UNIVERSITÀ DEGLI STUDI DI ROMA 'TOR VERGATA'

FACOLTÀ DI SCIENZE MATEMATICHE, FISICHE E NATURALI

Dipartimento di Fisica

Tesi di dottorato in Fisica

XXI Ciclo

a.a. 2008/2009

Neutron-based imaging applied to Cultural Heritage

Giulia Festa

Supervisors   *Prof. C. Andreani, Prof. M.P. De Pascale*

Coordinatore di dottorato   *Prof. P. Picozza*

Contents

Introduction

> 'Our cultural heritage is a legacy left to us by our forebears, which we in turn have a duty to pass on to our descendants.[...] We are at a turning-point. Science and technology present a host of exciting opportunities to the heritage sector. They must not be wasted.'

This statement, reported in the Science and Technology Ninth Report of the United Kingdom, was ordered by the House of Lords and printed the 19 October 2006 [1]. It is a notable example of the growing international interest demonstrated in science and technology applications devoted to the study of cultural heritage.

The discovery of an ancient artifact often raises a variety of questions such as the correct determination of its historical and cultural time-frame, the place and method of production, the choice of treatments and conditions for restoration and preservation.

In this field, new perspectives open up with the use of neutron-based techniques [2], [3].

The development of ad-hoc advanced neutron techniques such as imaging ones will provide essential tools to 'unveil secrets' in ancient objects and improve the knowledge about our past and about methods of heritage preservation for the future generations. Unlike other techniques, neutron based

analysis methods provide a unique opportunity to investigate whole objects without sectioning or damaging them. In fact neutrons penetrate through objects without substantial attenuation, a quality which makes them ideal for bulk, non-destructive testing.

The requirement to develop specific instrumentation and understand the real potentiality of neutron techniques applied to cultural heritage, springs from the contact between scientific or conservation institutions and museums. Of course, the potential and limits of these techniques are highly dependent on the intrinsic nature of the archaeological objects we want to study.

Neutron techniques can provide us precious structural information about the artifacts we want to study: composition, presence of alteration, crusts, inclusions, structure of the bulk, manufacturing techniques and presence of those elements which give us an overall fingerprint of the object's characteristics.

This thesis presents research results about the study of metal artifacts such Etruscan bronzes, ancient Roman coins or gilded bronzes, marbles and ceramics. All these objects posed crucial conservative, authentication or attribution questions.

In chapter 1 an overview of neutron production techniques and state of the art for 'standard' techniques is presented. It must be noted that such 'standard' techniques are actually quite recent in the field of archaeometry.

In chapter 2 a description of research and development about neutron instrumentation is provided: development of ancillary equipment for sample positioning is described and new prospectives for the Silicon-photomultiplier (SiPM) in the field of neutron applications are given.

In chapter 3 use of 'standard' neutron techniques in cultural heritage studies (in particular Neutron Diffraction) is assessed and validation and testing of their reliability in this field is reported: results derive from the

analysis of a large number of specifically constructed test samples.

In chapter 4 results from the use of 'standard' techniques on real and relevant archaeological objects are reported.

In chapter 5 preliminary results from newly developed techniques applied to notable archaeological samples are reported. The samples are parts of the well known *Porta del Paradiso* and North door by Lorenzo Ghiberti, from the *Battistero di San Giovanni* in Florence.

Finally conclusions and future perspectives related to the presented research are discussed.

Chapter 1

Neutron techniques for Cultural Heritage analysis

1.1 Properties of neutrons

A neutron is an electrically neutral subatomic particle whose physical properties listed in table 1.1. The weak decay of a free neutron is $n \rightarrow p + e + \bar{\nu}_e$ where p is the proton, e the electron and $\bar{\nu}_e$ the anti-neutrino, with a lifetime of about 15 minutes. Such lifetime is long enough to enable the use of a neutrons beam as a probe for materials investigation.

With the advent of nuclear reactors, thermal neutrons became an important probe for the recognition of structures and investigation of dynamics in condensed matter systems [4, 5].

Neutrons interact with atoms through nuclear forces or magnetic-dipole of unpaired electrons. Nuclear forces have a very short range, in the order of few fermi (10^{-12}m). As a consequence, neutrons can travel long distances through most materials without substantial attenuations. Moreover the elastic cross-section is not strongly dependent on the atomic number, unlike X-Rays and electrons where it is proportional to the atomic number (Z). A significant
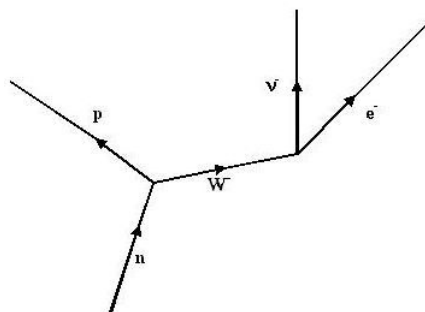
Figure 1.1: *Free neutron β-decay: $(n \rightarrow p + e^- + \bar{\nu}_e)$.*

PHYSICAL QUANTITY	VALUE
mass	1.675×10^{-27} Kg
charge	0
spin	1/2
magnetic dipole moment	$\mu_n = -1.913 \ \mu_N = 6.0311 \times 10^{-5}$ meV/Oersted

Table 1.1: *Neutron physical quantities ($\mu_n = $ nuclear magneton $= 5.051 \times 10^{-27}$ JT^{-1}).*

example is hydrogen which is transparent to X-Rays while it strongly scatters neutrons.

Neutrons additionally show three important advantages:

- It is easier to detect light atoms, such as hydrogen, in the presence of heavier ones

- Neighboring elements in the periodic table generally have different scattering cross-sections and thus can be distinguished

- Isotopes of the same element can be distinguished because have different cross sections for neutrons
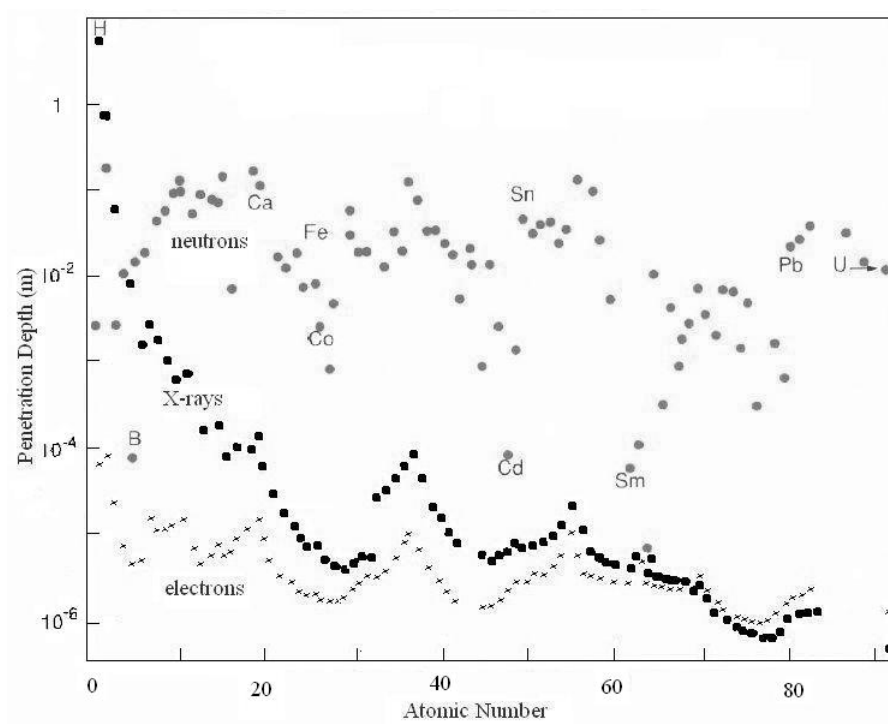
Figure 1.2: *Penetration depth for neutrons, X-rays and electrons.*

Because of their characteristics, neutrons can be considered as a non-destructive probe. This is a fundamental feature for the application of neutron techniques in Cultural Heritage.

The neutrons generally used in the study of condensed matter are in the thermal region (E$\sim$10 $-$ 100 meV) corresponding to a wavelength $\lambda \sim 3 - 1$ $\AA$ which is in the order of the inter-atomic distances.

From the De Broglie relation,

$$\lambda = \frac{h}{p} = \frac{h}{mv} \tag{1.1}$$

follows that:

$$E = k_b T = \frac{1}{2}mv^2 = \frac{h^2}{2m\lambda^2} = \frac{\hbar k^2}{2m} \qquad (1.2)$$

1.2   Neutron production at large scale facilities

Neutrons produced in large scale facilities are generated through different processes:

- Nuclear fission

- Photo-production

- Spallation

In the case of nuclear fission neutrons are produced in the core of reactors employing U^{235}. The process is based on the neutron capture by the fissile nucleus. The resulting deformation induces the nucleus to break up into two fragments. Some neutrons, $2-3$ neutrons for each fission, are released.
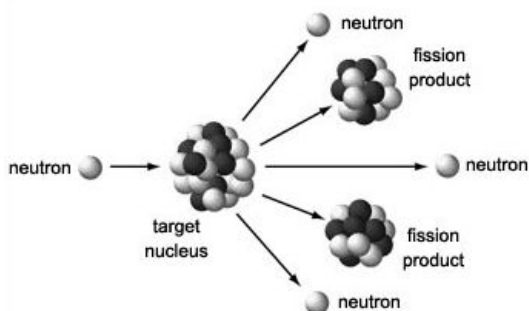

Figure 1.3: *Fission process.*

In photo-production, neutrons are produced when the energy of an incident photon is higher than the threshold energy of the (γ, n) reaction. This threshold depends on the atomic number of the target, ranging from 7-8 MeV for high Z materials (W, Pb, Fe) to 16-18 MeV for low Z elements (C, O). The photo-neutron energy spectrum is characterized by an evaporation peak in the low energy range and a relatively weak (10% of the integrated intensity) direct-reaction component in the several-MeV energy range with a resultant mean energy of (700 KeV - 1 MeV) [6].

In the spallation process high energy proton produced by accelerators, hit the nucleus of heavy atoms - such as lead (Pb) or tantalum (Ta) - with a pulse repetition rate triggering an intra-nuclear cascade and leaving the target nuclei in an exciting state (figure 1.4). As an example, a proton with energy E∼1GeV, hitting a tantalum target, will be produce on the average, 25 spallation neutrons.

Neutrons produced by these processes have energies that are in the range between a few to several hundreds of MeV. It is necessary to reduce the energy of incident neutrons before they can be used for scattering experiments. This is obtained through moderators: hydrogenated materials which make neutrons thermalize. Neutrons enter the moderator and, after a certain number of collisions, their energy will be equal to the energy of the moderator's nuclei. Hydrogenated materials are used because they have a large cross-section, thus maximising the neutron-moderator interaction [7]. Thermal neutrons are emitted at the moderator surface with an energy spectrum determined by the moderator temperature.

Neutrons are classified relatively to their energy as reported in table 1.2.

The spectra of moderated neutrons which eventually emerge into an experimental hall from a spallation source or a reactor are quite different. In fact the spallation beam has a greater percentage of high-energy neutrons
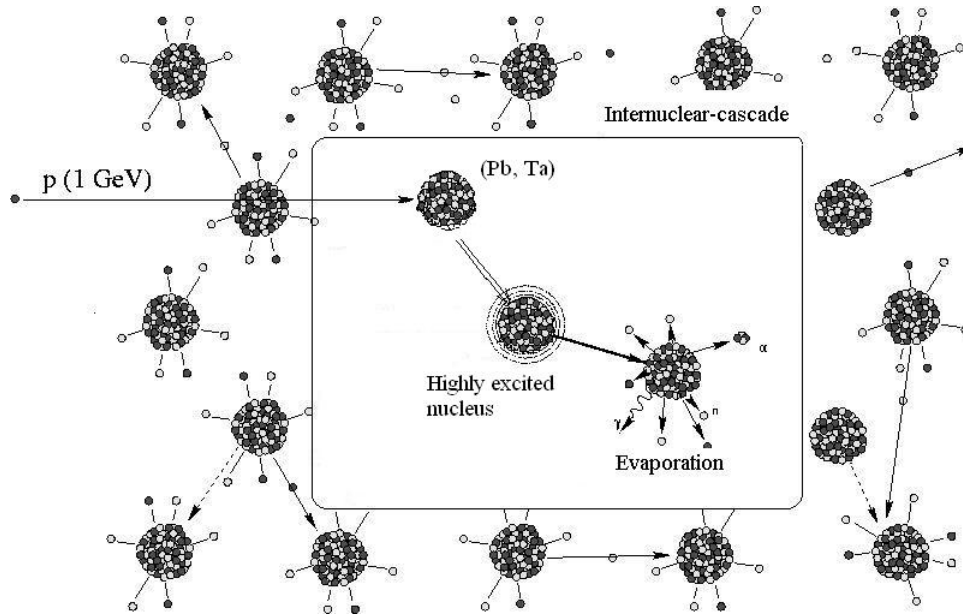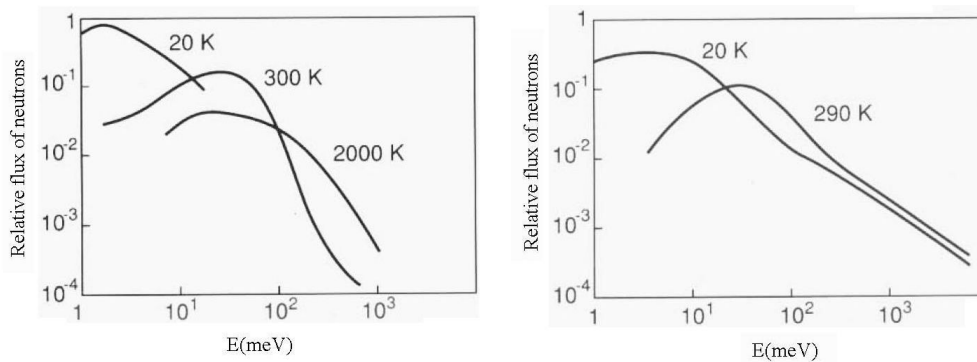
Figure 1.4: *Spallation process.*

Figure 1.5: *The relative flux of neutrons as a function of energy (a) for an high flux reactor (ILL), (b) for a spallation source (LANSCE).*

compared to the reactor one. There is another substantial difference: the neutron beam in a reactor is continuous while neutrons from a spallation

NAME	E (meV)	T (K)	λ (Å)
cold	0.1-10	1-200	30-3
thermal	10-100	120-1000	3-1
hot	100-500	1000-6000	1-0.4
epi-thermal	> 500	> 6000	> 0.4

Table 1.2: *Types of neutron beam - approximate values of range of energy, corresponding temperature and wavelength.*

source arrive in pulses. For a neutron source with neutron-flux time structure (as in the case of pulsed sources) what is measured is the time that each neutron takes to cover the distance between the moderator and the detector. Such time is defined as *Time Of Flight* (TOF). From the TOF, neutron velocity, therefore its wavelength, can be determined. As example with a flight distance of ~ 10 m it is obtained the neutron's TOF of ~ 5 ms. Because the neutron pulse is typically long a few tens of μs, its TOF can be determined with high precision.

During the PhD work three neutron sources have been used: two reactors (FRMII and BUDAPEST) and one spallation source (ISIS). In tables 1.3, 1.4 and 1.5, details for each source are reported.

The experiments performed by standard instrumentation and presented in this thesis, are based on scattering processes (in particular diffraction), absorption processes (as radiography/tomography) and radiative capture of neutrons in the case of Prompt Gamma Activation Analysis (PGAA).

Name	Value
ISIS Proton Synchrotron Energy	800 MeV
ISIS Pulsed frequency	50 Hz
ISIS average proton current on the target	175 μAh
Neutron yield	30 n/p
ISIS Fast neutron yield	4 $\times 10^{16}$ n/s

Table 1.3: *Parameters of ISIS Spallation Neutron Source, Chilton (Oxford), UK.*

Name	Value
Reactor type	Light-water cooled and moderated tank-type
Fuel	Uranium of 90% enrichment, UAl alloy
Nominal thermal power	10 MW
Mean power density in the core	61.2 KW/liter
Neutron flux density in the core	$2,5 * 10^{14}$ $ncm^{-2}s^{-1}$ (thermal), $1 * 10^{14}$ $ncm^{-2}s^{-1}$ (fast)

Table 1.4: *Parameters of Budapest Reactor, Hungary.*

Name	Value
Reactor type	Light-water cooled, heavy water moderated
Fuel	U_3Si_2
Nominal thermal power	20 MW
Neutron flux density in the core	8×10^{14} $ncm^{-2}s^{-1}$ (thermal)

Table 1.5: *Parameters of FRMII Reactor, Munich, Germany.*

1.3 Non-destructive probe to shed light on the past

1.3.1 Base theory of neutron scattering

The scattering of neutrons by nuclei is a quantum-mechanical process and can be described in terms of the wave function of the incident neutron and the nucleus. This wave function has the form of a sinusoid and the square of the amplitude at any point is related to the probability that the neutron will be found at that point [5]. The scattering of a neutron by a single nucleus can be described in terms of *cross section* (σ) that is equivalent to the effective area presented by the nucleus to the passing neutron. If the neutron hits this area it will be scattered with the same probability in all directions.

Considering the scattering of a neutron with a single nucleus at rest, the wavelength of thermal neutrons is in the order of 10^{-10} m while the nuclear forces that cause nuclear scattering have a range of $10^{-14} - 10^{-15}$ m. Therefore, the wavelength of the incident neutron beam is greater than the forces' range. As a consequence the scattered wave can be considered to have a spherical symmetry. If the origin is set in the position of the nucleus, and the z axis in the **k** incident wave-vector direction, the incident neutron beam can be described by:

$$\psi_{inc} = e^{ikz}$$

If the scattering has a spherical symmetry, the scattered wave has the form:

$$\psi_{scat} = -\frac{b}{r}e^{ikz}$$

where b is the *scattering length* and measures the strength of the interaction between the neutron and the scattering nucleus. In this particular case the energy of the incident beam is small enough not to change the internal energy

of the nucleus, so the *scattering* is *elastic* and the incident neutron's energy is conserved.

The intensity of the neutron beam, given by the square of the amplitude of the wave function, decreases as the inverse square of the distance from the source that in this case is the scattering nucleus.

The cross section in the case of single fixed nucleus scattering, $d\sigma/d\Omega$, is:

$$\frac{d\sigma}{d\Omega} = \int_0^\infty \left(\frac{d^2\sigma}{d\Omega dE}\right) dE$$

The flux of incident neutron beam is:

$$\Phi = v \left|\psi_{inc}\right|^2 = v$$

and from the definitions of *differential cross section*: $\frac{d\sigma}{d\Omega}$= (number of neutron scattered for second into $d\Omega$ in a determinated direction)$/\Phi d\Omega$

and *cross section*: σ_{tot}= total number of neutrons scattered for second$/\Phi$ follows that:

$$\frac{d\sigma}{d\Omega} = \frac{vb^2 d\Omega}{\Phi d\Omega} = b^2$$

and in the simple case of s-wave scattering:

$$\sigma_{tot} = 4\pi b^2$$

describes the relationship between scattering length (b) and the cross section (σ).

In the general case of neutrons scattering on matter both the momentum and the energy of the neutrons and the matter change. Hence the scattering is not necessarily elastic, atoms can recoil during collisions or absorbed energy. Applying 4-momentum conservation, the momentum transfer is given by:

$$\frac{h}{2\pi}\mathbf{Q} = \frac{h}{2\pi}(\mathbf{k} - \mathbf{k'}) \tag{1.3}$$

where $\mathbf{k}$ is the wave vector of the incident neutrons and $\mathbf{k}'$ is the wave vector of the scattered neutrons. $\mathbf{Q}$ is known as scattering vector. The angle between $\mathbf{k}$ and $\mathbf{k}'$ is known as scattering angle (2θ). Measuring the scattering per incident neutron, flux and the energy lost by the neutron, a one obtains the relative positions and the relative motions of atoms in matter.

Scattering effects are distinguished in two effects: the coherent and incoherent scattering.
In coherent scattering, the neutron wave interacts with the whole sample as a unit and the scattered waves from different nuclei interfere which each others. In this case the scattering depends on the distance between the point scatterers and thus gives information about the structure of the materials (as diffraction).

During incoherent scattering the neutron wave interacts independently with each nucleus in the sample so that the scattered waves from different nuclei don't interfere.

The techniques that will be described in the following subsections are:

- Time Of Flight neutron diffraction

- Prompt Gamma Activation Analysis

- Neutron Radiography and Tomography

They were used in the research work presented in this thesis.

1.3.2   Time Of Flight neutron diffraction technique

Neutron Diffraction (ND) is a powerful technique for investigating the crystal structure of samples. Diffractometers at a spallation sources are primarily based on the determination of neutrons' energy for a 'white beam', measuring their *Time Of Flight* (TOF). These energies are:

$$E = \frac{1}{2}m_n v^2 = \frac{1}{2}m_n \left(\frac{L}{TOF}\right)^2 \tag{1.4}$$

where m_n is the neutron's mass, v its velocity and L the flight length of the pulsed beam from the moderator to the sample. Using the De Broglie relation 1.4 becomes:

$$E = \frac{1}{2}m_n \left(\frac{h}{m_n\lambda}\right)^2 \tag{1.5}$$

where h is the Planck constant and λ the neutron's wavelength.

The diffraction process is described as the reflection of incident beam by crystal planes (hkl). The well known Bragg's law $n\lambda = 2d_{hkl}sin\theta$ in the case of TOF measurements, can be re-written as a relation between the TOF of neutrons scattered from a set of planes in the sample and the spacing between these planes, d_{hkl}:

$$(TOF)_{hkl} = \frac{2m_n}{h}Ld_{hkl}sin\theta_0 \tag{1.6}$$

where θ_0 is a fixed scattering angle. The resolution of a neutron diffractometer describes the instrumental contribution to the peak widths, and for a time-of-flight instrument is given by:

$$\frac{\Delta d}{d} = \left[\left(\frac{\Delta(TOF)_{hkl}}{(TOF)_{hkl}}\right)^2 + (cot\theta\Delta\theta)^2 + \left(\frac{\Delta L}{L}\right)^2\right]^{1/2} \tag{1.7}$$

The first term $(\Delta(TOF)_{hkl}/(TOF)_{hkl})$ is the moderator source broadening term and depends on the moderator characteristics. The second term

$(cot\theta\Delta\theta)$ is the angular dispersion and comes from the finite angular widths of the sample, the detector and the moderator. The term $(\Delta L/L)$ derives from the uncertainties in the flight path and is constant for a given measurement.

The diffraction patterns showing Bragg peaks, obtained from a measurement, used to identify phases, structures or to derive texture information. The peak positions are directly related to the crystal lattice dimensions. The peak intensities are determined by the atomic arrangement in the unit cell and are related to the structure factor by:

$$I_{hkl} \propto |F_{hkl}|^2 = \left|\sum_j b_j \cdot exp\{2\pi i(h \cdot x_j + k \cdot y_j + l \cdot z_j)\}\right|^2 \qquad (1.8)$$

where b is the neutron scattering length and depends on the kind of atoms in the sample, (h, k, l) are the Miller indexes and (x, y, z) define the atomic position in the unit cell.

The diffraction patterns are related to structural information at different scales:

- 'phase structure' describes compounds content

- 'crystal structure' is related to the atomic arrangement of each phase

- 'grain structure' represents size, shape and orientation of grains (texture)

- 'micro-structure' describes structural deviation from an ideal crystal within a grain

All of these levels are, of course, inter-dependent. A quantitative evaluation of structural properties requires analysis of data in terms of *peak position* related to changes in the lattice parameters, macro and micro strains;

peaks widths related to the particle size and micro-strain broadening; and *intensities* related to the atom arrangements and grain orientations [8].

For the diffraction measurements reported in the present work three diffractometers where used. The set-ups for each diffractometer are shown in figure 1.6.
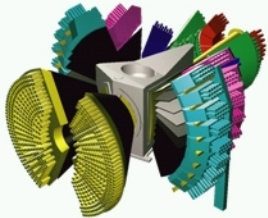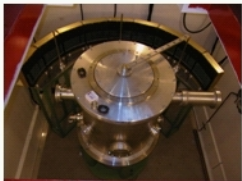

ROTAX

3 detector banks in horizontal plane

fast acquisition, medium resolution

Flight path 14.0 m

GEM

6 detector banks

fast acquisition, high resolution

Flight path 17.0 m

INES

9 detector banks in horizontal plane

slow acquisition, high resolution

Flight path 22.8 m

Figure 1.6: *Diffractometers at ISIS spallation source. ROTAX, GEM, INES diffractometers and their characteristics are presented.*

- **Quantitative multi-phase analysis and Rietveld method**

The quantitative phase analysis is mainly based on three principles: each phase exhibits a unique set of Bragg diffraction peaks; the intensity of each peak of a particular phase is proportional to the phase weight-fraction; the measured diffraction pattern is the simple sum of all single-phase patterns.

The first step in quantitative phase analysis is to identify the phases present in the sample. For such identification the Bragg peak positions of experimental diffraction patterns are compared with the peak-sets of known compounds, usually obtained through databases such as PDF [9], ICSD [10] and CRYSTMET [11]. The structure information (such as lattice parameters, space group, atom position) of identified phases obtained from these databases are generally stored in the CIF ('Crystallographic Information File') file format, the standard data exchange file format used in crystallography [12].

The second step is to fit the experimental diffraction patterns with those of known compounds obtaining quantitative multi-phase analysis through the Rietveld method. The core of the procedure is to make a least-square fitting of the calculated pattern and provides values of the phase composition and the adjustment of the structure parameters. Micro-structural characterization and preferred orientation parameters through refinement of peak broadening are also available. The calculated intensity profile is given by:

$$I_{ic} = I_{ib} + \sum_{\Phi=1}^{N_\Phi} S_\Phi \sum_{k=K_1}^{K} j_{\Phi k} L p_{\Phi k} P_{\Phi k} \left| F_{\Phi k} \right|^2 \Omega_{i\Phi k} \qquad (1.9)$$

where I_{ic} is the calculated intensity of the ith point,

I_{ib} is the background contribution,

S_Φ is a scale factor proportional to the volumic fraction of each refined phase,

$j_{\Phi k}$ is the multiplicity factor of the peak of the Φ phase,

$Lp_{\Phi k}$ is a factor related to the preferred orientations of the phase Φ,

$|F_{\Phi k}|$ is the structure factor of the particular phase Φ,

$\Omega_{i\Phi k}$ describes the profile function of the peaks of Φ phase and represents instrumental and potential sample broadenings. The first sum runs on all phases present in the sample, while the second on the reflections k which contribute to the ith measured point. A least-square fitting can be obtained by minimizing the function:

$$M = \sum_i w_i (I_i - I_{ic})^2 \tag{1.10}$$

where I_i is the observed intensity compared to the calculated intensity (I_{ic}) and w_i is the weighting factor at the ith measured point [8].

The multi-phase Rietveld refinement can be performed with software such as GSAS [13], MAUD [14] or FULLPROF [15]; the first two were used in the analysis described in the following chapters.

- **Texture analysis**

  Texture is the preferred orientation of crystallites and is an intrinsic characteristic of materials such as metals, ceramics, rocks. This characteristic influences physical properties of the samples and is related with geological phenomena in the rocks-formation or with the working-methods of metals and ceramics. Different mechanisms can produce or modify texture and many methods have been used to determine preferred orientation depending on the type of sample. Today diffraction techniques can be used to measure such property of materials. ND, in particular, offers some advantages compared to other techniques in the case of bulk samples namely the fact that there is no need to section the object under examination.

Firstly, in order to determine the orientation of a given lattice plane *hkl* of a single crystallite, the detector is set to the proper Bragg angle (2θ) of the diffraction peak of interest. Then the sample is rotated in a goniometer until the lattice plane *hkl* reaches the reflection condition. In a polycrystalline material, the intensity recorded at a certain sample orientation is proportional to the volume fraction of crystallites with their planes in the reflection geometry [16, 17]. In a pulsed neutron source detector panels are present and cover large angular areas thus recording simultaneously diffraction spectra from crystals in different orientations.

In the case of polycrystalline materials the orientations of crystallites are expressed in terms of probability distribution and described by the *orientation distribution function* (ODF) $f(g)$ defined as:

$$dV/V = f(g)dg \tag{1.11}$$

where dV is the volume of grains with orientation g, dg is the element of orientation space and V is the volume from which data is collected.

In the diffraction pattern, the presence of texture is expressed in systematic intensity variations of Bragg peaks. Consequently, the intensities are linked to the crystal structure by means of the structure factor but they are also linked to the texture through the ODF. Texture analysis is generally presented trough 'pole figures' in which a specified crystallographic axis (or *pole*) from each of a representative number of crystallites is plotted in a stereographic projection, along with directions relevant to the material's processing history (such as the rolling direction and transverse direction or the fiber axis). Therefore, a pole figure is a two-dimensional projection of the ODF which

is a 3-dimensional function representing the continuous density distribution of orientations. Such pole figure represents the probability of finding a pole to a lattice plane (hkl) in a certain sample direction. Pole figures are normalized to express this probability in multiples of a *random distribution* (m.d.r.).

In order to specify a crystallite orientation, it is necessary to set up two coordinate systems: one relating to the whole specimen and the other relating to the crystal. Both systems are Cartesian and generally right-handed. The axes of the first coordinate system, the sample coordinates, are chosen according to particular directions associated with the external shape of the specimen. In the case of rolled products, for example, rolling direction (RD), direction normal to the rolling plane (ND) and transverse direction (TD) are chosen.

The second coordinate system, the crystal coordinates, is specified by the directions in the crystal: the choice of directions is arbitrary but it is convenient to adapt it to the crystal symmetry.

To derive the pole figure a reference sphere (with radius 1 and the crystal in center) is considered. The direction of any three-dimensional vector in the crystal (for example a crystallographic direction or the normal to a crystal plane) can be described as a point (the *pole*) on the unit reference sphere. To represent the three-dimensional orientation information on the unit sphere in a two-dimensional plane, it is necessary to project the sphere onto this latter plane. In crystallography and metallurgy, stereographic projection is used.

The position of a given pole on the sphere is commonly characterized by two angles: α describing the azimuth of the pole with $\alpha = 0^0$ corresponding to the north pole of the unit sphere; β describing the rotation of the pole around the polar axes [18].
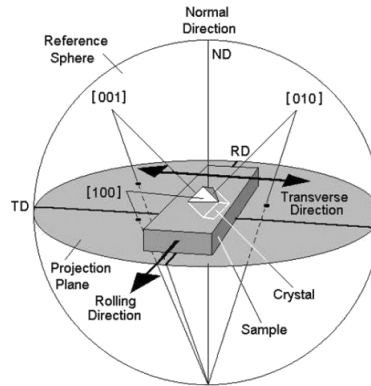
Figure 1.7: *Pole figure construction. Stereographic projections of [001], [010], [100] poles on the equatorial planes.*
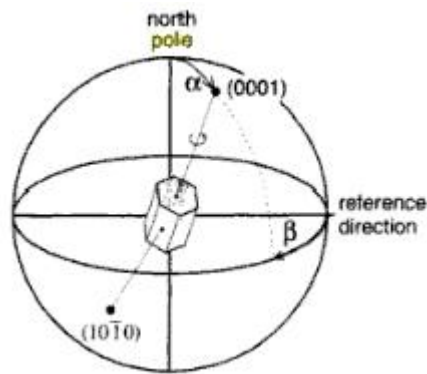

Figure 1.8: *Orientation of the basal plane in the hexagonal crystal. The position of the pole is defined by the α and β angles.*

1.3.3   Radiative capture of neutrons and PGAA

Prompt Gamma Activation Analysis (PGAA) is a neutron technique based on the radiative capture of neutrons, a nuclear reaction that takes place for each isotope of every element (exept ^4He). The so-called (n, γ)-reaction takes place when a nucleus absorbs a neutron and a compound nucleus is formed. The exciting energy is equal to the sum of the binding energy and the kinetic energy of the absorbed neutron. The decay of the compound nucleus takes place in about 10^{-16} s while the nucleus reaches its ground-state in $10^{-9} - 10^{-12}$ s emitting 2-4 gamma rays, called *prompt gammas*, in a cascade. Prompt gamma energy is characteristics of the emitting nuclide. Their intensities, moreover, are proportional to the number of atoms of a given nuclide present in the irradiated area. Generally, a nuclide emits a large number (several hundreds) of different energies prompt gamma rays, and the spectrum is usually complicated.

The energy of the emitted prompt gamma ray (E_γ) is given by the difference between the energy of the transition (E_T) and the recoil-energy of the nucleus (E_R):

$$E_\gamma = E_T - E_R, \quad E_R = \frac{E_\gamma^2}{2m_A c^2} \tag{1.12}$$

where m_A is the mass of the radiation atom and A is its atomic number. An important characteristic of the radiative capture of neutrons, is that both captured and emitted particles have a high penetration power. The neutron beam generally illuminates the bulk samples and the results of measurements are given by an average composition of the illuminated area. The obtained analytical result is the identification of the nuclide independent from the chemical state of the sample. In PGAA systems excitation and detection happen in the same time: the sample is illuminated from the neutron beam while gamma radiation is detected perpendicularly to the neu-

tron beam direction, generally through a Germanium detector. The beam direction and the viewing solid angle of the detector define the active volume where the gamma rays come from. PGAA can be defined non-destructive: in fact no sample preparation is required and the irradiation doesn't change the elemental composition of the irradiated sample.

The complexity of prompt gamma spectra depends on the nuclear levels structure of the irradiated sample, in particular the number of levels between the capture state and the ground state. For this reason, the lightest nuclides lack a level below their capture states and thus only one prompt gamma peak is present in the spectrum corresponding to the transition from the capture state to the ground state. Although in principle any element could be identified by PGAA, in reality detection limits exist. Such limits depend on the spectral background produced by: room-background, which is always present, and beam-background which is present when the beam is on. At low energies the spectral background is enhanced by photo-electrons bremsstrahlung, Compton-electrons and β particles emitted by radioactive nuclides. In the completely background-free region (at the upper end of the spectrum) there are only 2-4 counts which are enough to identify a peak, while on the high background baseline several hundred of counts are necessary to distinguish the peak from the background [19].
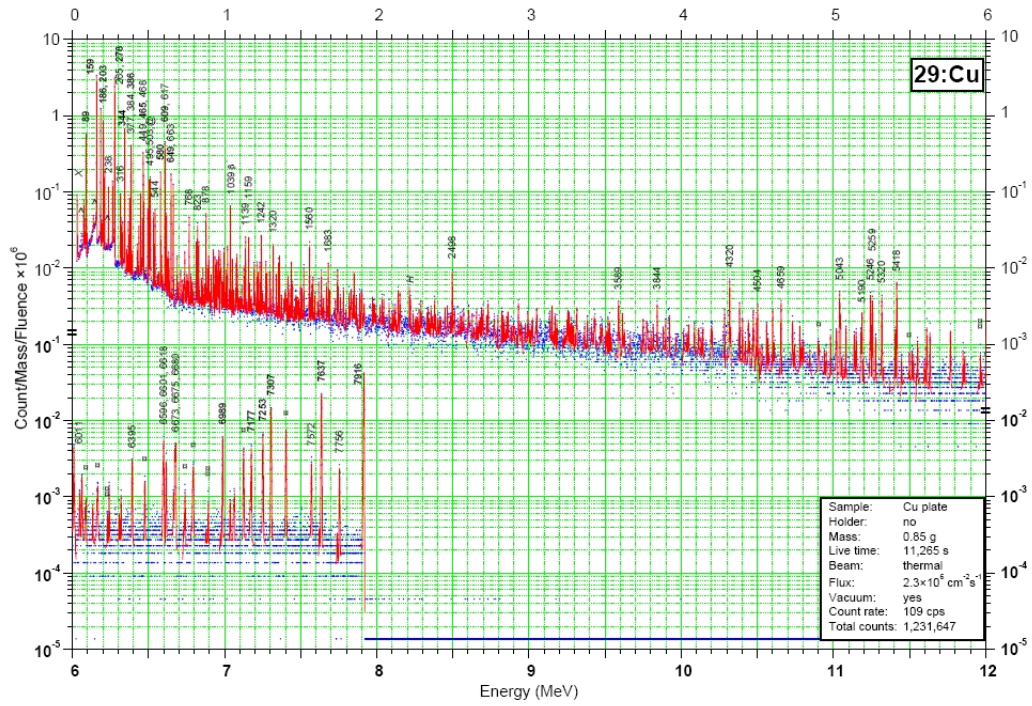
Figure 1.9: *Gamma spectrum of* ^{29}Cu.

1.3.4 Neutron Radiography and Tomography techniques

Radiography is a method of non-destructive testing. Internal examination of an object is carried out by exposing it to a beam of X-Ray or neutrons. Internal feature can be seen on a screen or recorded on film. The technique of neutron radiography is known since more than 50 years, related to the availability of suitable neutron sources as research reactors or spallation neutron sources. Tomography is an extension of radiography. In general, it is a non-destructive technique to investigate the inner structure of an object in three-dimension. The 3D structure is reconstructed based on a set of 2D projections, that are the radiographies, taken from different angles by rotating the sample around a defined axis.

When the neutron or X-ray beam pass trough a sample, part of the radiation is attenuated by the sample-material. The change in beam intensity is related to the material absorption for the particular probe. Absorption and scattering processes are the interactions that contribute to beam attenuation. In conventional radiography the attenuation on incident beam by the sample can be described by an exponential function:

$$I(x,y) = I_0(x,y)e^{-\int_{path} \mu(x,y,z)dz} \tag{1.13}$$

where $I(x,y)$ and $I_0(x,y)$ are the intensity of transmitted and incident beam in a plane (x,y) transversal to the propagation direction z.

The *linear attenuation coefficient* (μ) depends on the physical process from which the particle is absorbed by the material and describes the fraction of a beam that is absorbed or scattered per unit thickness of the absorber. The charge-free neutrons interact with the core of the atoms, while in contrast, X-rays interact with the charge distribution of the electronic shell. Therefore the X-ray absorption coefficient depends on atomic number. In the case of neutrons, in fact, the probability that a neutron interact with the atomic core depends on the coherent scattering length. The latter is inde-
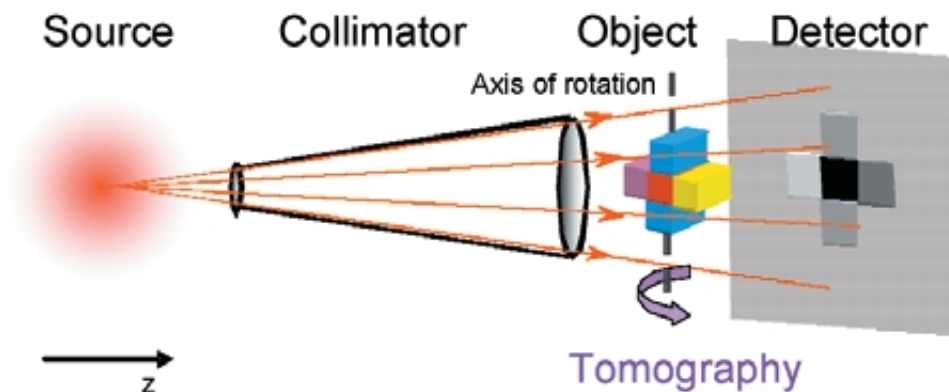
Figure 1.10: *Diagram of a standard tomography set-up [20].*

pendent from the atomic number but change from one isotope to another. The attenuation properties are, also, related with the energy of the incident radiation.

The coefficient for neutrons and X-rays are shown in figures 1.11 and 1.12.

The degree of attenuation is represented, on the detection system as CCD cameras or films, with different gray degrees.

To pass from the group of projections to the 3D reconstruction it is necessary to use reconstruction algorithms. Figure 1.14 shows the simplest geometry of parallel configuration.

In this case projection of an object at a given angle θ is made up of a set of line integrals. The line integral represents the total attenuation of the beam as it travels in a straight line through the object. The resulting image is a 2D model of the attenuation coefficient. The data are considered to be collected as a series of parallel rays, at position r, across a projection at angle θ, repeating the measure for a set of angles. Using equation 1.13, the total attenuation P of a ray at position r, on the projection at angle θ is given by the line integral:

H 0.02																	He 0.02
Li 0.06	Be 0.22											B 0.28	C 0.27	N 0.11	O 0.16	F 0.14	Ne 0.17
Na 0.13	Mg 0.24											Al 0.38	Si 0.33	P 0.25	S 0.30	Cl 0.23	Ar 0.20
K 0.14	Ca 0.26	Sc 0.48	Ti 0.73	V 1.04	Cr 1.29	Mn 1.32	Fe 1.57	Co 1.78	Ni 1.96	Cu 1.97	Zn 1.64	Ga 1.42	Ge 1.33	As 1.50	Se 1.23	Br 0.90	Kr 0.73
Rb 0.47	Sr 0.86	Y 1.61	Zr 2.47	Nb 3.43	Mo 4.29	Tc 5.06	Ru 5.71	Rh 6.08	Pd 6.13	Ag 5.67	Cd 4.84	In 4.31	Sn 3.98	Sb 4.28	Te 4.06	I 3.45	Xe 2.53
Cs 1.42	Ba 2.73	La 5.04	Hf 19.70	Ta 25.47	W 30.49	Re 34.47	Os 37.92	Ir 39.01	Pt 38.61	Au 35.94	Hg 25.88	Tl 23.23	Pb 22.81	Bi 20.28	Po 20.22	At	Rn 9.77
Fr	Ra 11.80	Ac 24.47	Rf	Ha													

	Ce	Pr	Nd	Pm	Sm	Eu	Gd	Tb	Dy	Ho	Er	Tm	Yb	Lu
*Lanthanides	5.79	6.23	6.46	7.33	7.68	5.66	8.69	9.46	10.17	10.91	11.70	12.49	9.32	14.07
	Th	Pa	U	Np	Pu	Am	Cm	Bk	Vf	Es	Fm	Md	No	Lr
**Actinides	28.95	39.65	49.08											**x-ray**

Figure 1.11: 150 *KeV X-ray linear attenuation coefficient scales* $[cm^{-1}]$ *with atomic number Z.*

$$P(r,\theta) = \ln(I/I_0) = -\int \mu(x,y)\, ds \tag{1.14}$$

Using the coordinate system described in Figure 1.14, the value of r onto which the point (x,y) will be projected at angle θ is given by:

$$x\cos\theta + y\sin\theta = r \tag{1.15}$$

and the equation 1.14 can be written as:

$$P(r,\theta) = \int_{-\infty}^{\infty}\int_{-\infty}^{\infty} f(x,y)\delta(x\cos\theta + y\sin\theta - r)\, dx\, dy \tag{1.16}$$

where $f(x,y)$ represents $\mu(x,y)$. This function is known as the Radon transform or sinogram of the 2D object. The *projection-slice theorem* say that from an infinite number of one-dimensional projections of an object taken at an infinite number of angles, it is possible to totally reconstruct the original object, $f(x,y)$. So to get $f(x,y)$ back, from the above equation means finding the inverse Radon transform. It is possible to find an explicit

H 3.44																	He 0.02
Li 3.30	Be 0.79											B 101.60	C 0.56	N 0.43	O 0.17	F 0.20	Ne 0.10
Na 0.09	Mg 0.15											Al 0.10	Si 0.11	P 0.12	S 0.06	Cl 1.33	Ar 0.03
K 0.06	Ca 0.08	Sc 2.00	Ti 0.60	V 0.72	Cr 0.54	Mn 1.21	Fe 1.19	Co 3.92	Ni 2.05	Cu 1.07	Zn 0.35	Ga 0.49	Ge 0.47	As 0.67	Se 0.73	Br 0.24	Kr 0.61
Rb 0.08	Sr 0.14	Y 0.27	Zr 0.29	Nb 0.40	Mo 0.52	Tc 1.76	Ru 0.58	Rh 10.88	Pd 0.78	Ag 4.04	Cd 115.11	In 7.58	Sn 0.21	Sb 0.30	Te 0.25	I 0.23	Xe 0.43
Cs 0.29	Ba 0.07	La 0.52	Hf 4.99	Ta 1.49	W 1.47	Re 6.85	Os 2.24	Ir 30.46	Pt 1.46	Au 6.23	Hg 16.21	Tl 0.47	Pb 0.38	Bi 0.27	Po	At	Rn
Fr	Ra 0.34	Ac	Rf	Ha													

*Lanthanides	Ce 0.14	Pr 0.41	Nd 1.87	Pm 5.72	Sm 171.47	Eu 94.58	Gd 1479.04	Tb 0.93	Dy 32.42	Ho 2.25	Er 5.48	Tm 3.53	Yb 1.40	Lu 2.75
**Actinides	Th 0.59	Pa 8.46	U 0.82	Np 9.80	Pu 50.20	Am 2.86	Cm	Bk	Cf	Es	Fm	Md	No	Lr neut.

Figure 1.12: *Linear thermal (0.025 eV) neutron attenuation coefficient* $[cm^{-1}]$.

formula for the inverse Radon transform. However, the inverse Radon transform proves to be extremely unstable with respect to noisy data. In practice, a stabilized and discretized version of the inverse Radon transform is used, known as the filtered back projection algorithm [21].

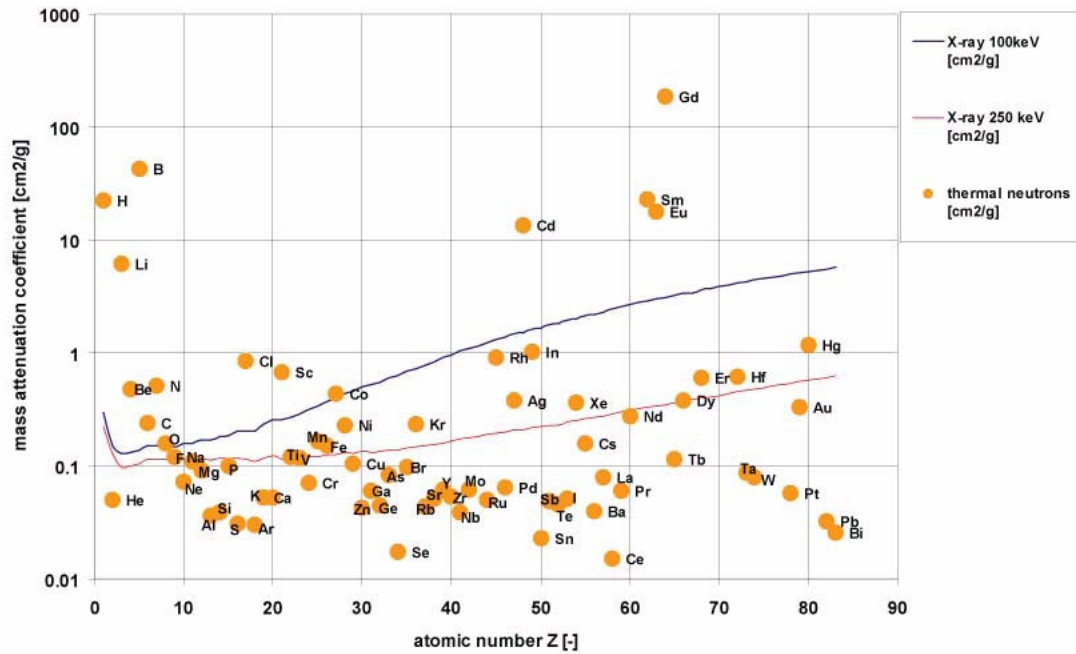The parallel beam geometry is typically used for the neutron tomography.

Figure 1.13: *Diagram of X-ray and neutron attenuation coefficient for all elements. X-ray's of 100 or 250 KeV penetrate low Z materials easily, whereas high Z materials induce high radiation attenuation. Thermal neutrons (bullets) are weakly attenuated by silicon or calcium, showing strong attenuation for hydrogen. Heavy elements are easily transmitted by neutrons. There is no systematic dependence of neutron attenuation with atomic number Z.*
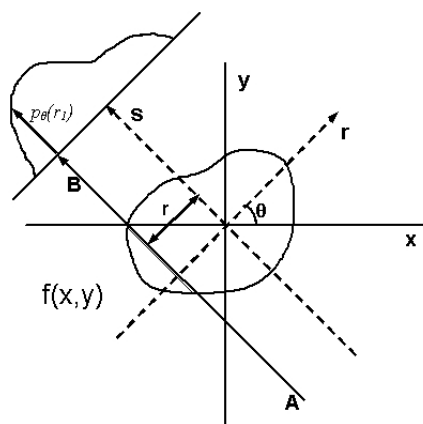
Figure 1.14: *Scheme of parallel beam geometry.*

Chapter 2

Innovative neutron instrumentation

This chapter presents the research and development activities on neutron instrumentation such as sample positioning system for Prompt Gamma Activation Imaging/Neutron Tomography (PGAI/NT) instrument and the use of silicon-photomultiplier (SiPM) as neutrons and gammas detector coupled by YAP crystal to obtain small and compact, low cost, portable detector system.

A large variety of chemical, physical and micro-structural techniques are employed to characterize objects of archaeological significance. The potential of neutron-based techniques for archaeometry is large while their development is recent in most cases. Especially, no attempt has been made to use the unique resonance absorption properties of epithermal neutrons for quantitative 3D imaging. Many elements have neutron absorption resonances in the epithermal energy range. Neutron absorption is followed by the prompt emission of a gamma-ray cascade, and both the gamma emission and the neutron transmission can be measured. Spatially resolved information can, in principle, be obtained by a combination of tight neutron beam collima-

tion, multiple positioning of the sample, and simultaneous measurement of neutron resonances with different strengths and therefore able to effectively probe depth. Developing the 'Neutron Resonant Capture Imaging' combined with 'Neutron Resonance Transmission' (NRCI/NRT) as a non-invasive technique for 3D tomographic imaging and its use in cultural heritage research is the ultimate aim of the ANCIENT CHARM European project. The idea of developing an imaging technique based on epithermal neutron absorption is totally new and presents a number of scientific and technical challenges which are best addressed by the joint development of two related 3D imaging methods: Prompt Gamma Activation Imaging combined with cold Neutron Tomography (PGAI/NT) and Neutron Diffraction Tomography (NDT). The three new imaging methods will provide a new, comprehensive neutron-based imaging approach, which will be applied for the 3D imaging of elemental and phase composition of objects selected as a result of a broad scope archaeological research.

2.1 Sample positioning of Cultural Heritage objects

The developed sample positioning system is integrated in the new imaging technique, named PGAI/NT, produced by the combination of the Prompt Gamma Activation Analysis (PGAA) and Neutron Tomography (NT), two standard techniques, described in chapter 1 that are combined together in an innovative procedure of measurement.

Trough PGAI measurements the objects are scanned by determining the compositions of small volumes within the sample. This little volume investigated, named iso-volume, is determined by the intersection of the high collimated neutron beam (2 mm × 2 mm) with the line of sight defined by the collimator of the Germanium detector. A complete 3D scan of the object by PGAI would take a lot of time, nevertheless by using the 3D NT image of the object it is possible to decide pre-emptively the zone of interest and to be able to determine compositions exactly in that regions. This combination of the NT with PGAI speeds up the investigation of the object considerably. The assembly operations, testing and preliminary measurements were performed at the neutron source on the Budapest Neutron Center, a 10 MW Research Reactor. Here, the neutrons are cooled by a moderator and guided to the experimental area by means of a super-mirror guide. The NIPS experimental station can accommodate various measurement configurations such as gamma-gamma coincidence or a new type of setup. The incident neutron beam spot is 20 mm by 20 mm, when used for neutron tomography. For PGAI, an adjustable neutron collimator was fabricated from ^6Li-enriched polymer, which can provide a 2 mm wide pencil beam with height of 2 to 20 mm. The sample is located at the center of a 20 cm × 20 cm × 20 cm sample chamber made of ^6Li-enriched polymer with no bottom wall. The Tomography set up is placed in transmission mode while the PGAI set-up is

mounted at 90 degree to the beam, close to the lead collimator that has a minimum size of 2 mm $\times$ 2 mm. The $xyz - \omega$ moving table is placed under the sample chamber and move the object respect to the beam, allowing a scanning of the sample.

The schematic drawing and pictures of the PGAI-NT setup are shown in figures 2.1 and 2.2.
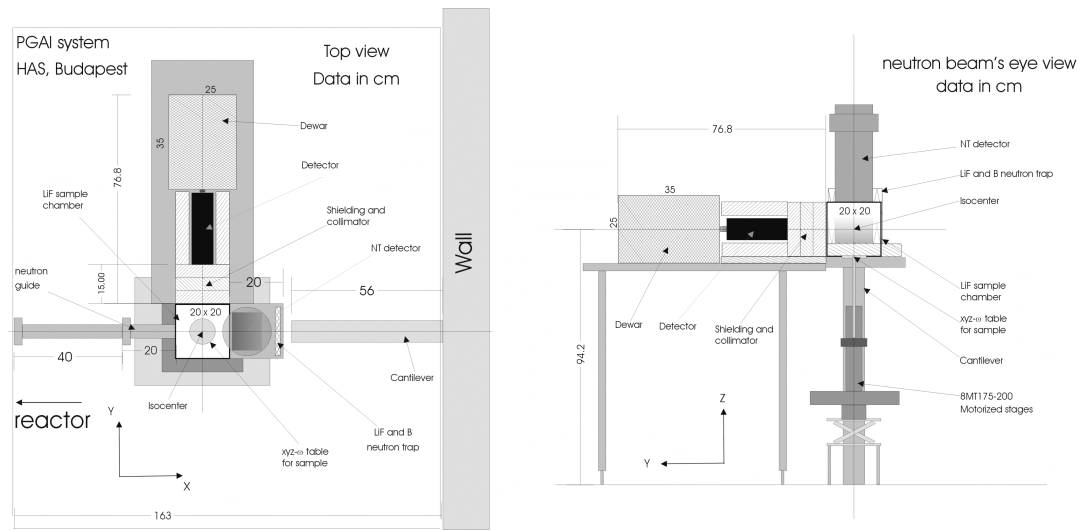

Figure 2.1: *Scheme of the Budapest PGAI setup.*

An integrated data acquisition system has been developed in Igor Pro by the Institute of Isotopes at Budapest Neutron Center (BNC). It can control all systems involved in the measurements.

In this context, the $xyz - \omega$ moving system has been specifically assembled for Prompt Gamma Activation Imaging (PGAI) measurements. This device allows for correct positioning and automated movement (three translations and one rotation) of samples with respect to the neutron beam for scanning purposes. Main characteristics of the device are listed in Table 2.1.

The device consists of three linear slits connected to linear motors $8MT175-$
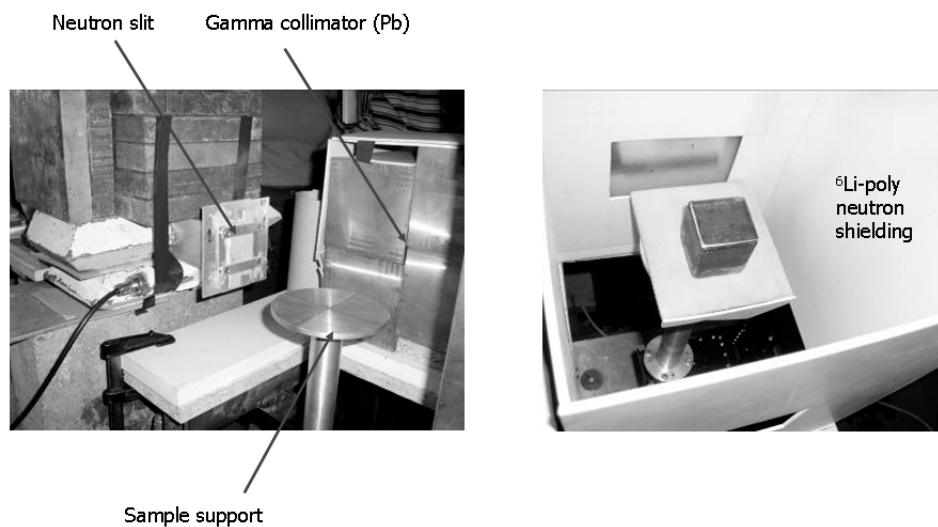
Figure 2.2: *Photograph of Budapest PGAI/NT setup.*

200 of Standa.srl to perform the xyz movements plus one rotation axis (ω) connected to the rotation motor $8MR150$ of the same supplier. All slits are made in pure Aluminum and their movements along the slits are automatically provided by an external motors controller.

In order to optimize the acquisition time, it was possible to restrict the sample-scanning using the movement system with an input file that contains the coordinates of the surface of the sample. A preliminary laser-scan produce, as output, a file which contains reference point. The laser scanner that makes this operation is Scanny 3D system.

The effectiveness of this system to reconstruct the object surface is shown in figure 2.4.

A software tool has been developed in order to read the output file of the scanner driving motors of the 3D position. This software is a package of functions that can be included as a library in the master data acquisition

$8MT175-200$ (Motorized Linear stages)	
Lead screw pitch	0.5 mm
Max speed	4 mm/s
Min speed	0.5 mm/s
Position resolution at Min speed	2.5 μm
Position resolution at Max speed	20 μm
Horizontal Load capacity	8 Kg
Vertical Load capacity	3 Kg
$8MR150$ (Motorized rotation stage)	
Rotation range	360^0
Resolution	$0.6 arcmin$
Rotation speed	12^0/s
Horizontal load capacity	6 Kg
Radial	1.7 Kg
Torque	0.5 N/m
Motor cable integrated	2 meters long

Table 2.1: *Main mechanical characteristics of the two different mechanical motorized stages of the $xyz - \omega$ table.*

programs. A set of command lines allows the user to initialize and control the movements:

- **Auto System**
  Utility = Read input file and start single motor's movement
  Command line variables = An input .txt file that contains:
  - First line = Device Number (program connect the specified device: motors 1, 2, 3, 4),
  - Second line = Destination position (in μ-steps),
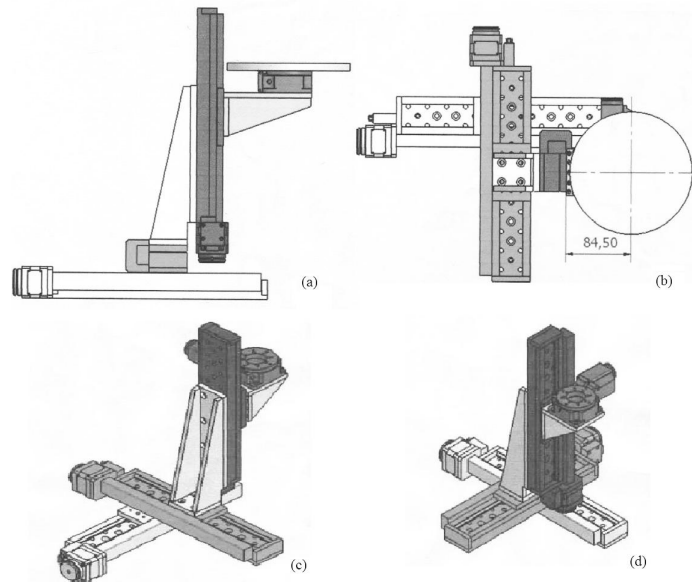
Figure 2.3: *Schematic drawings of the $xyz - \omega$ table: (a) lateral view (b) upper-view, (c) and (d) 3D view of the $xyz - \omega$ table where the translation and rotation stages are clearly visible. The dashed arrows indicate the direction of the neutron beam.*

- Third line = Speed (Speed of rotation in the units of real world)-speed advise max 200 1/s,
- Fourth line = Step-Divider (step is devided by this factor: 1, 2, 4, 8).

- **Reset Motors**
  Utility = Overrides current position value of controller,
  Note = Can be use to reset to zero or a given value,
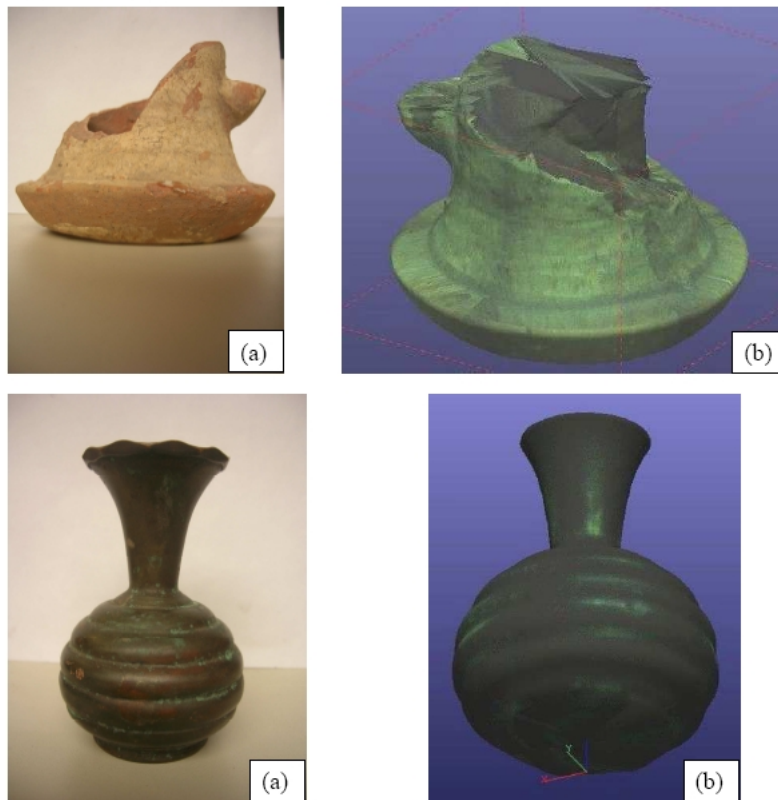 *Command line variables* = Device Number, Position (if it's not specified are set to zero).

Figure 2.4: *Digital acquisition of cultural heritage objects. (a) photograph of the object (b) colour acquisition mapping.*

- **Step Motors output**
  Utility = Read current position from the controller and put into an output file,
  Note = Can be use to observe if the motor is in destination position,
  Command line variables = Device, output file-name,

- **Stop Motors**

Utility = Stop immediately motor movement,
Note = Can be use integrated with an emergency stop system,
Command line variables = Device Number.

Figure 2.5: *Scheme of automatic and control system for table movements.*

2.2   Neutron and gamma detectors

2.2.1   The Silicon-photomultiplier for neutrons application

The development of a suitable instrumentation, i.e. components and detectors, plays a key role importance in the exploitation of the great capabilities offered by neutrons. The research activity on neutron detectors is strategic for the development of reliable application of the neutron techniques. Efficiency, spatial and time resolutions are the features for good detectors, and despite the physical properties of this particle restrict the field of the neutron detection reactions, the new technologies in radiation sensors as well as electronics may contribute greatly in enhancing the present performances, thus providing a step forward, towards a highly performing neutron instrumentation. The Silicon Photomultipliers (SiPM) [22], [23] offer a unique opportunity, due to their low cost, robustness and radiation hardness. These photomultipliers operate at low voltages (in the range 30-70 V) and have reduced volumes as compared to the standard neutron detection devices. The small volume allows a great flexibility in detector development with good efficiency.

The aim of the present study is to compare the SiPM (silicon photomultiplier) and standard PMT (standard photomultiplier) performances for gammas and neutron detection at spallation neutron source.

2.2.2 Set-up description

The new gamma/neutron detector pilot system is based on four components:

- A crystal (6 mm × 6 mm × 25 mm) scintillator (YAP)

- A Cadmium foil converter (for neutron detection)

- 1 mm^2 Hamamatsu silicon photomultiplier (SiPM)

- A Standard Hamamatsu Photomultiplier (PMT)

The same set-up is used in two configurations: without cadmium foil as gammas detector, with cadmium foil converter as neutron detector (figure 2.6). In the first case, the gammas emitted by the sample go through the YAP crystal where they release most of their energy, thus inducing the generation of scintillation photons. These are then multiplied by the PMT and SiPM and the voltage signal provides the counting event for the data acquisition electronics. In the second case, the detection mechanism is performed by neutron absorption, with a certain probability, onto the cadmium foil and, consequently, gammas emission; they reach the scintillator and perform the same effect as in the first case. The Time Of Flight of these induced gammas could be thought as instantaneous respect to the neutrons diffraction Time-Of-Flights considered and the signal from the SiPM and PMT will reflect the diffracted neutrons Time-Of-Flight structure.

The assembled detector is shown in figure 2.7.

The electronics is composed by one integrated low-power supply developed and assembled at UNITOV (E. Reali), with only one 5 volts as input and the needed voltages as output ($\pm 6V$ for the SiPM pre-amplifier, 71 V for the SiPM itself and $+12V$ for the PMT), the SiPM polarization circuit, the external SiPM preamplifier [24] and the integrated PMT pre-amplifier as illustrated in figure 2.8.
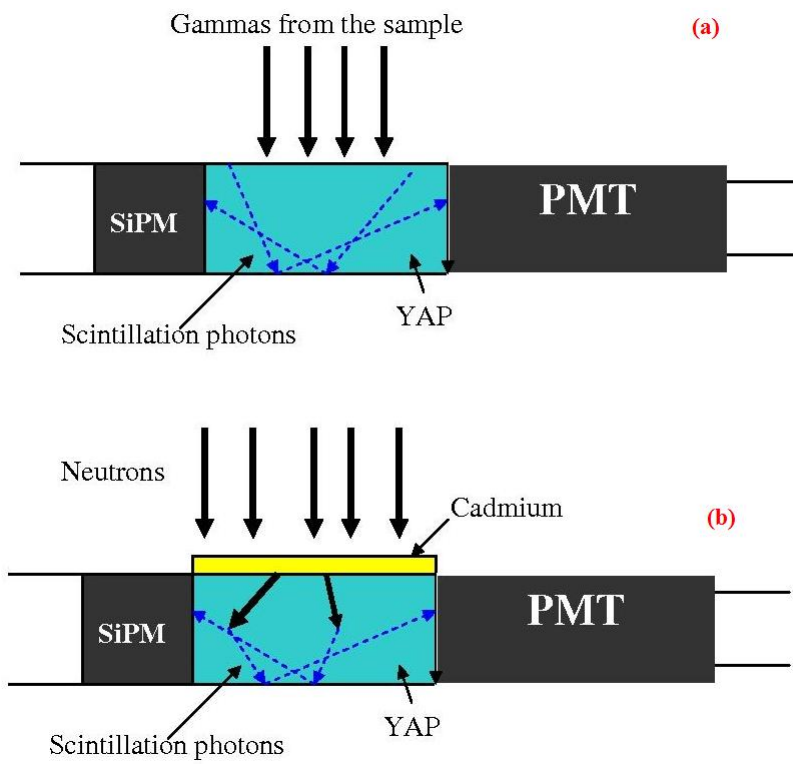
Figure 2.6: *Schematics of detection system in two configurations: (a) gammas configuration (b) neutrons configuration.*
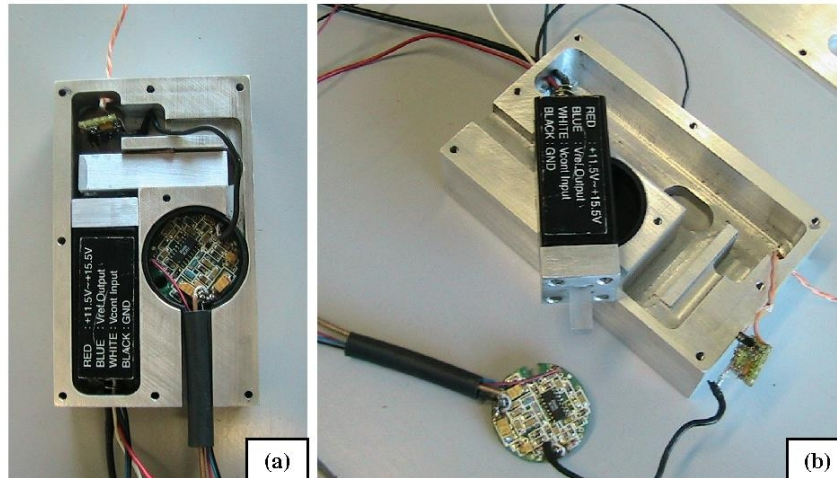
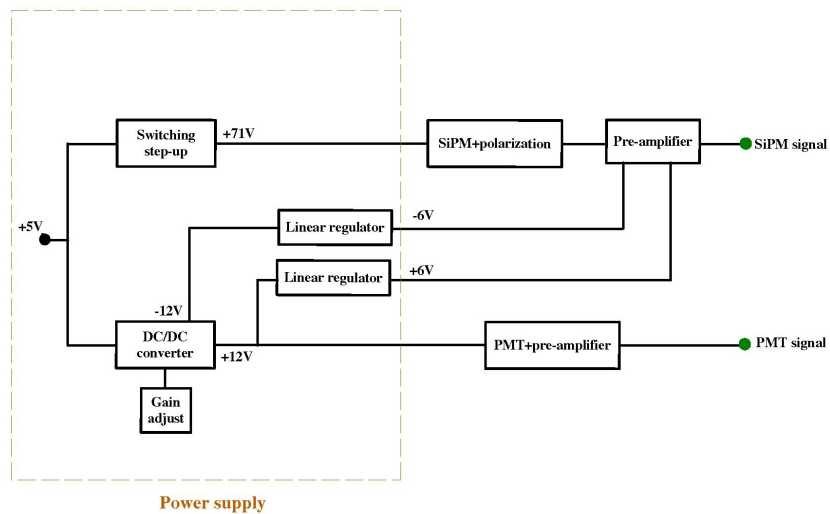**Figure 2.7:** *Pictures of the experimental set-up.*

Figure 2.8: *Scheme of the electronics for the PMT-YAP-SiPM system.*

- **YAP characteristics**

  Yttrium-Aluminum-Perovskite (**YAP:Ce**) is a fast, mechanically and chemically resistant scintillator material. This inorganic scintillator is non hygroscopic, glass-like, with a high density (5.55 g/cm^3) and an effective atomic number of $Z = 36$. Main characteristics of this scintillation material are a good light yield (about 18000 photons/MeV) and a short decay time $\tau = 27$ ns for $\lambda = 350$ nm (wavelength of maximum emission). YAP scintillators are normally employed for photon spectroscopy in different fields including Mossbauer spectroscopy, X-ray imaging and medical applications.

  In table 2.2 the main physical and scintillation properties of the Yttrium-Aluminum-Perovskite (Ce doped) scintillator are presented, while in table 2.3 a comparison of the main characteristics of YAP, Sodium Iodide (NaI(Tl)) and Bismuth Germanate (BGO) are presented.

photons/MeV @300K	~ 18000	cleavage plane	*none*
effective Z	31.4	**density**	5.37 g/cm^3
melting point	$1,875\ ^0C$	**hardness [Moh]**	8.6
hygroscopic	$1,875\ ^0C$	**hardness [Moh]**	8.6
decay constant	27 ns	**refractive index [@ 370 nm]**	1.95
afterglow @ 6ms	$< 0.005\%$	**Light output [NaI(Tl)=100%]**	$\sim 40\%$
crystal structure	Rhombic	**chemical formula**	$YAlO_3 : Ce^+$

Table 2.2: *List of the main physical and scintillation properties of the Yttrium-Aluminum-Perovskite (Ce doped) scintillator.*

Property	YAP:Ce	NaI(Tl)	BGO
Density (g/cm^3)	5.55	3.67	7.13
Effective Atomic Number	36	50	83
Hardness (Mho)	8.5	2	5
Hygroscopic	No	Very	No
Wavelength of Emission Maximum (nm)	350	415	480
Refractive Index at Emission Maximum	1.94	1.85	2.15
Decay Time (ns)	27	230	300/60
Relative Light Output	40	100	20
Light Output, Photons per MeV	18000	38000	8500

Table 2.3: *Comparison of three different scintillator materials, namely YAP, NaI and BGO.*

• **PMT characteristics**

The H6780 is a commercial photo-sensor module housing a metal package PMT and high-voltage power supply circuit produced by Hamamatsu. The characteristics of this PMT are high gain, wide dynamic range and fast response while maintaining small dimensions. The internal high-voltage power supply circuit is also compact, making the module easy to use.
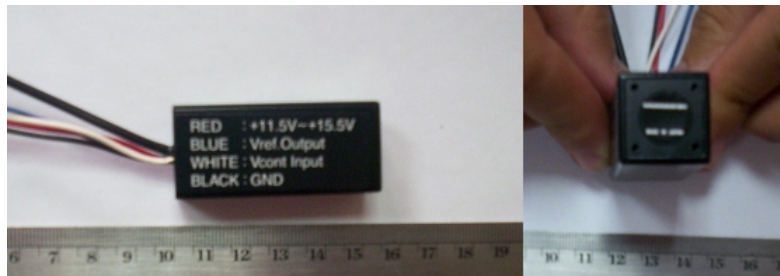

Figure 2.9: *Lateral (left side) and top (right side) views of the H6780 PMT.*

- **SiPM characteristics**

The Silicon Photomultiplier (**SiPM**) is a photon counting device consisting of multiple avalanche photo-diodes (APD) pixels. The APDs are high-speed, high-sensitivity photo-diodes that internally amplify photo-current when a reverse bias is applied. Its structure allows a high fill to ensure high photon detection efficiency. This device is essentially an opto-semiconductor device with excellent photon counting capability combined to the low voltage operation, the insensitivity to magnetic fields, high peak photon detection efficiency (more than 50%) and a good response [25],[26]. The independently operating pixels are connected together in a simple output signal. In the present application the SiPM device is used as a proportional counter. The SiPM topology is shown in figure 2.10.
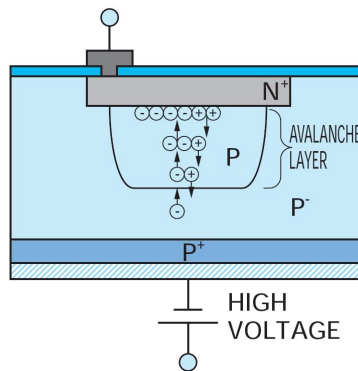

Figure 2.10: *Topology of SiPM.*

The SiPM device were developed and used for particle physics such as, for example, readout of detectors for Cherenkov photons [27], minimum ionizing particles [28] and dark matter searches[29]. It was used also in medical physics applications such as PET (Positron Emission

Parameters	Value
Chip size	$1.5 \times 1.5 \ mm^2$
Active area	$1 \times 1 \ mm^2$
Pixel size	$25 \times 25 \ \mu m^2$
Spectral response range	$270 - 900$ nm
Peak sensitivity wavelength (λ_p)	400 nm
Quantum efficiency (λ_p)	70 min %
Time resolution	250 ps %

Table 2.4: *SiPM Specifications.*

Tomography) [30], [31], [32].

2.2.3 PMT and SiPM for gamma detection

The measurements of gammas produced by neutron irradiation of a Copper-Antimony (Cu-Sb) alloy were performed with the detector system described in section 2.2.2. Both Cu and Sb have several resonances in the radiative neutron capture cross sections in the eV region. Gamma's measurements were performed by both SiPM and the standard PMT in order to assess the performances of the silicon-photomultiplier with respect to the well known standard photomultiplier in the field of gamma induced by neutrons. The sample were a copper-antimony alloy ($Cu_{92}Sb_8$) standard of cultural heritage interest. The detector system was positioned at a distance $L_1 \approx 1m$ from the sample at $\alpha \approx 90^0$ with respect to the incident neutron beam direction. Both detectors measured the emitted prompt-gammas from the sample during irradiation.

The spectra acquired by SiPM and PMT are shown in figure 2.11. It could be observed that the two signals have a similar shape.

Peaks resonance gammas are clearly visible from the spectra. The intensity ratio of the two spectra is about 3, which is mostly due to the reduced geometrical coupling between YAP and SiPM compared to the PMT. Since the prompt-gammas are emitted by the nucleus in 10^{-9} - 10^{-12} s after capture of a neutron $[(n,\gamma)$-reaction], the Time-Of-Flight of the neutrons has been calculated considering instantaneous the prompt-gamma emission respect to the time-window detected (time order of milliseconds). The acquisition start of the data is triggered by the ISIS clock (50 Hz) and the stop pulse of the Time Of Flight is determined by the detection of the prompt gammas from the sample. Using the energy resonance from the radiative capture cross section spectrum, the TOF of neutrons that produce resonances is given by the relation:
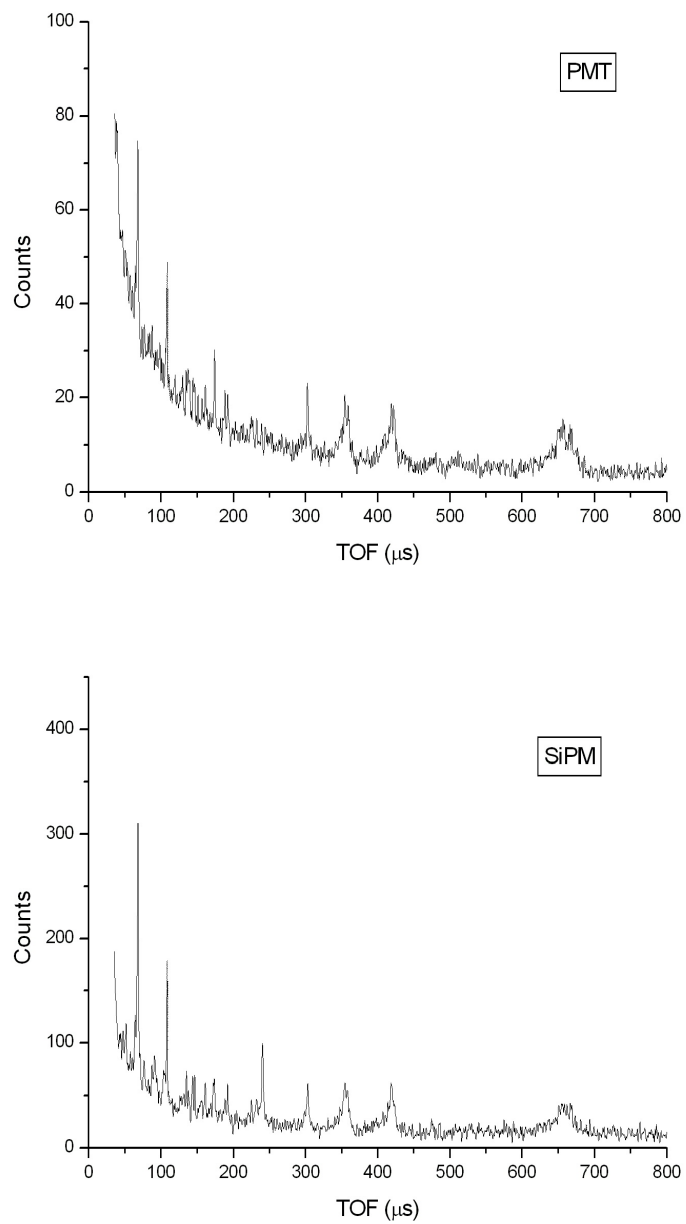
Figure 2.11: *Flight spectra recorded by PMT and SiPM.*

$(TOF)_{res}$ **PMT** (μs) ± 0.26	$(TOF)_{res}$ **SiPM** (μs)± 0.26
662.02	662.53
420.67	419.67
354.36	355.04
302.67	303.19
231.27	231.09
225.49	225.32
203.27	204.65
182.43	182.25
161.07	160.89
119.21	119.37
108.36	108.35
68.39	68.39
64.43	64.26
57.53	58.23
52.33	51.85
44.45	44.96

Table 2.5: *Gamma peaks Time-Of-Flight from the standard photomultiplier (PMT) and the silicon photomultiplier (SiPM).*

$$(TOF)_{res} = \frac{L_0}{\sqrt{2E_r/m_n}} \tag{2.1}$$

where $(TOF)_{res}$ is the Time Of Flight of the resonances, L_0 is the INES flight length, E_r and m_n the resonance energy and the mass of the neutron.

In this way, the experimental gamma peaks in the PMT and SiPM Time Of Flight spectra have been identified and associated to the isotopes present in the sample. To obtain the isotopic abundances of the object it was per-

formed the comparison with the most abundant isotopes of Sb and Cu elements:

$^{121}Sb = 57.25\%$ $^{123}Sb = 42.75\%$

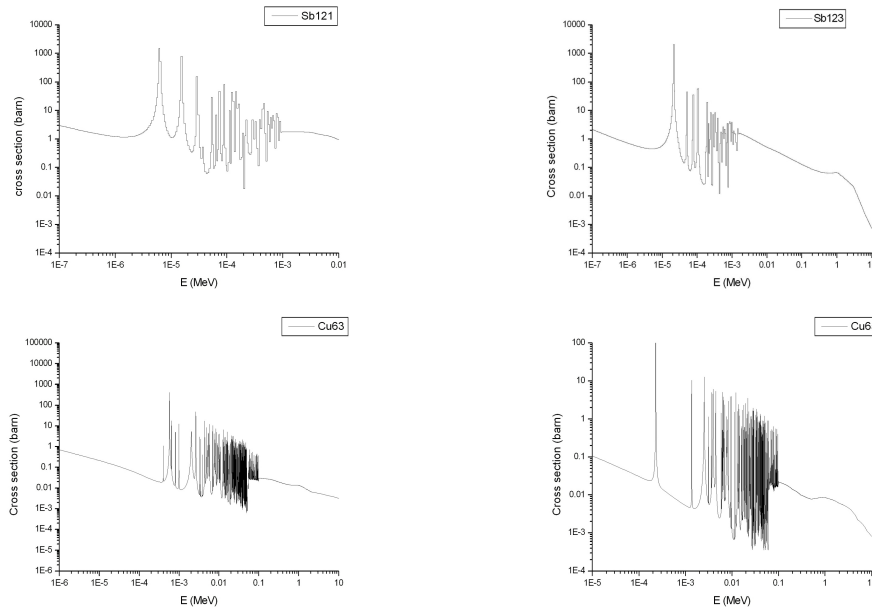$^{63}Cu = 69.17\%$ $^{65}Cu = 30.83\%$

Figure 2.12: *Radiative Capture Cross section of ^{63}Cu, ^{65}Cu, ^{121}Sb, ^{123}Sb.*

As it is shown in figure 2.13 and table 2.6, the SiPM signal gives a good performance in that application.

The energy resolution of the PMT and SiPM has been calculated using a Voight fit. The FWHM of the most important peaks are shown in table 2.7.

(a) ^{121}Sb

$E(eV)$	$t(\mu s)$
6.16	663.9
15.37	420.1
28.85	306.6
53.09	226.2
64.26	205.3

(b) ^{123}Sb

$E(eV)$	$t(\mu s)$
21.59	354.8
50.65	231.5
77.73	183.2
105.50	160.3
193.62	118.4

(c) ^{63}Cu

$E(eV)$	$t(\mu s)$
583.30	68.2
640.66	65.1
811.20	58.0
981.82	52.6

(d) ^{65}Cu

$E(eV)$	$t(\mu s)$
228.65	108.9
1371.00	44.5

Table 2.6: *List of gamma's Time-Of-Flight of principal components of the sample (^{121}Sb, ^{123}Sb, ^{63}Cu, ^{65}Cu) for the INES instrument (flight path=22.804 m).*

t_{res} (μs)	**FWHM SiPM (μs)$\pm$0.26**	**FWHM PMT (μs)$\pm$0.26**
663.9	25.40	26.02
420.1	9.65	9.64
354.8	9.65	8.62
306.6	2.62	2.01
108.9	1.37	1.36
68.2	3.11	2.59

Table 2.7: *FWHM of main peaks in the TOF spectra recorded by PMT and SiPM.*
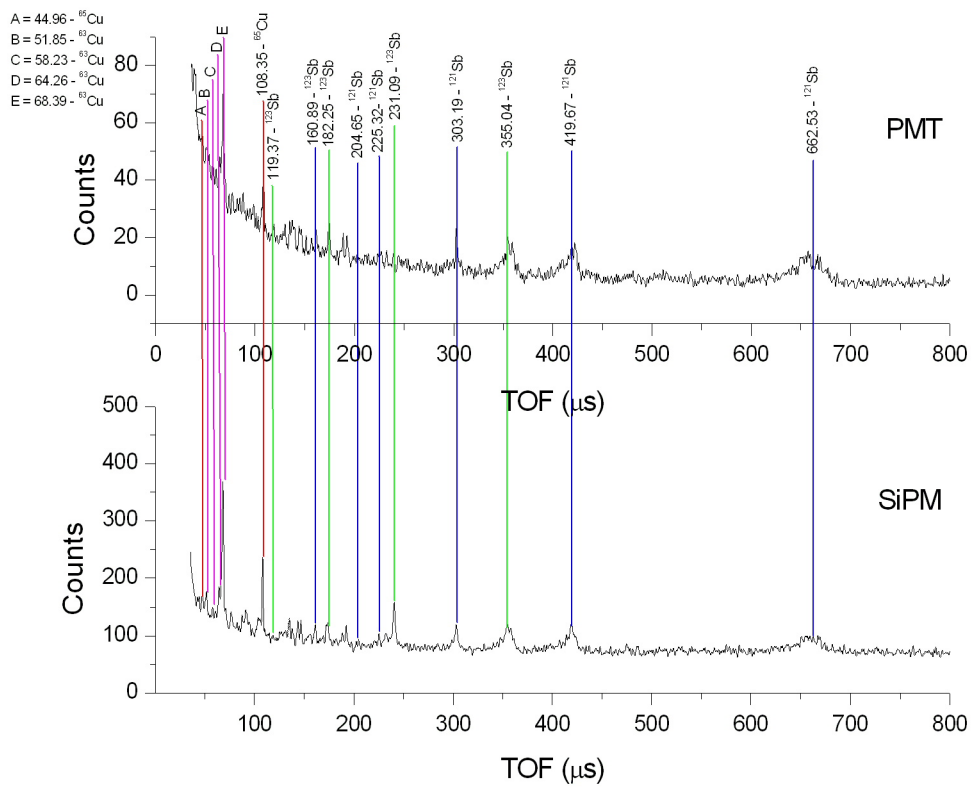
Figure 2.13: *Peaks identification in the PMT and SiPM spectra.*

2.2.4 PMT and SiPM for neutron detection

Diffracted neutron measurements were performed on an iron (Fe) sample. The detector system was positioned in the same place of the previous gammas measurements, at one meter from the centre of instrument. Neutrons are scattered from the sample and hit the cadmium-foil-converter in front of the YAP crystal, emitting gamma rays. The cadmium-foil have the role of converter: in thermal neutrons range (beam energy of the order of meV) the radiative cross section has a plane zone without resonances and a cut-off in the range of epi-thermal neutrons: it act as a filter (see figure 2.14).
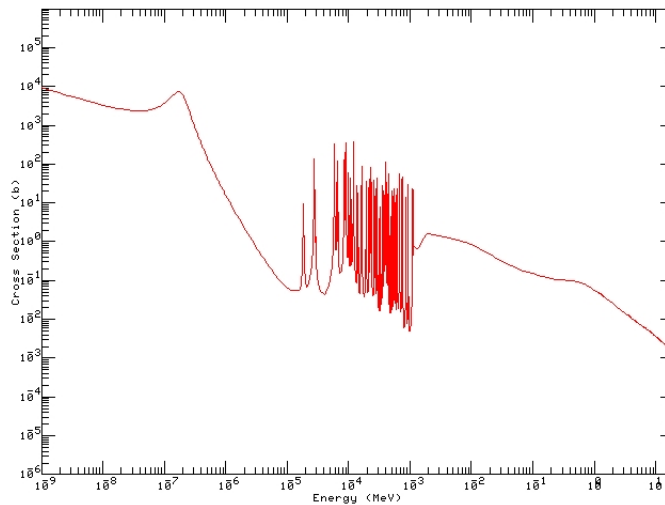
Figure 2.14: *Radiative Capture cross-section of Cadmium.*

The raw spectra acquired by SiPM and PMT, in diffraction condition, are shown in figure 2.15. It could be observed that the two signals are very similar.

The peak positions of SiPM and PMT spectra are additionally compared with the corresponding ^3He detector spectrum at the same angle $\alpha \approx 90^0$ with respect to the incident neutron beam direction. As it is shown in figure
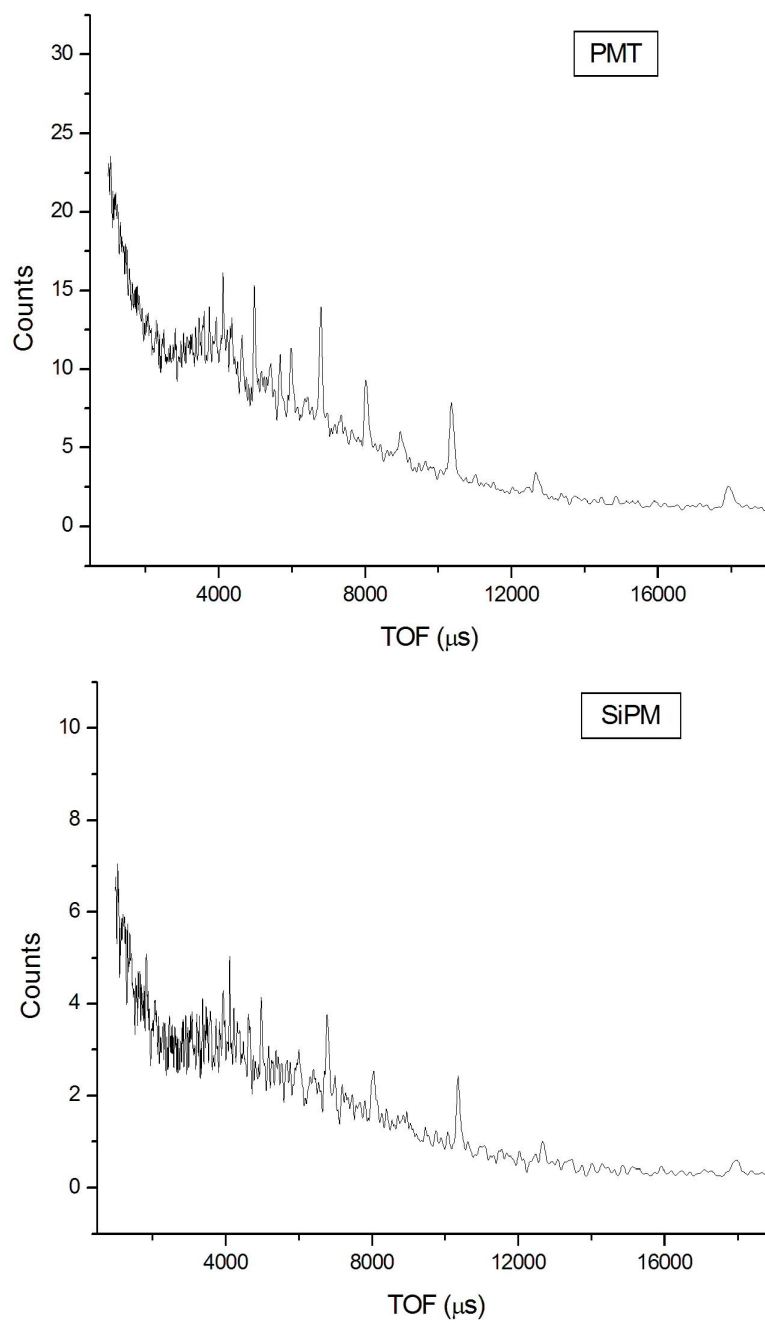
Figure 2.15: *Time Of Flight diffraction patterns recorded by PMT and SiPM.*

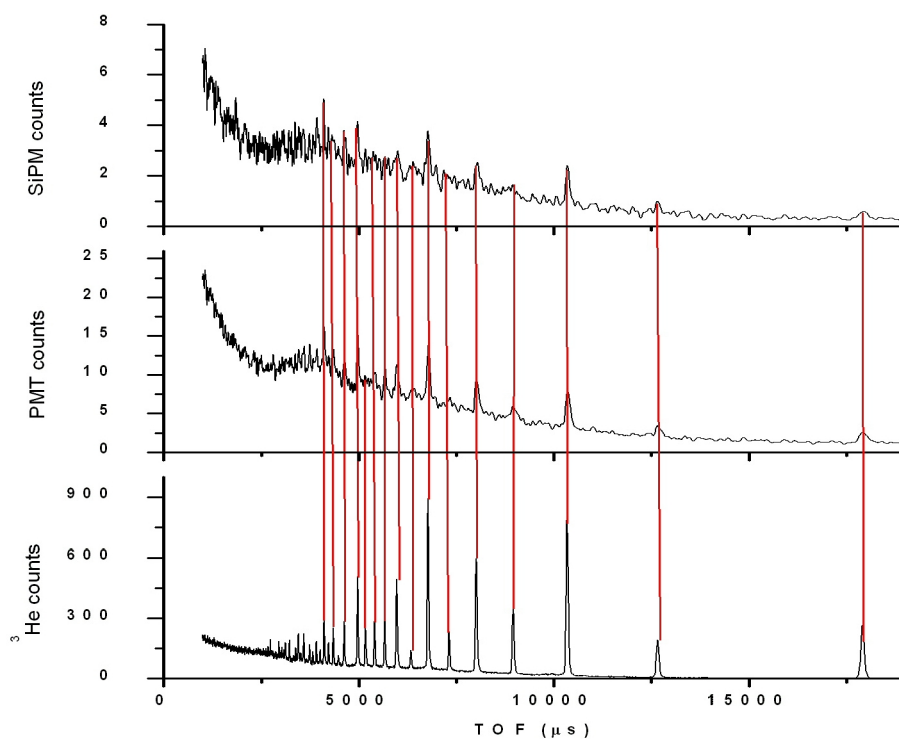2.16 the peak position, in Time Of Flight, is the same in all three cases.

Figure 2.16: *Peaks position comparison between PMT, SiPM and standard ^3He detector mounted on INES spectrometer.*

A detailed list of neutron peaks Time-Of-Flight from the standard photomultiplier (PMT), the silicon photomultiplier (SiPM) and the ^3He gas detector are reported in table 2.8.

TOF ^3He (μs)$\pm$0.26	TOF PMT (μs)$\pm$0.26	TOF SiPM (μs)$\pm$0.26
17926	17937	17948
12680	12691	12680
10355	10366	10360
8966	8966	8960
8017	8023	8040
7314	7257	7189
6783	6783	6777
6331	6383	6400
5966	5977	6500
5669	5669	5664
5406	5383	5371
5177	5171	5164
4998	4994	4966
4623	4629	4617
4355	4326	4320
4103	4103	4103

Table 2.8: *Neutron peaks Time-Of-Flight from the standard photomultiplier (PMT), the silicon photomultiplier (SiPM) and the ^3He gas detector.*

2.2.5 Conclusions

The results obtained by the SiPM-YAP-PMT pilot system for neutron or gamma detection show the effectiveness, the practicality and the high potential of the SiPM technology for neutron spectroscopy at spallation neutron sources. The observation and identification of gamma peaks produced by resonant isotopes, present in the sample, has been performed. Moreover the applications to neutron diffraction with novel detection concept (the SiPM) has been achieved.

The pilot experiment described, provided useful information for subsequent design of a high-efficiency and good resolution SiPM-detectors array in the context of neutronics.

Chapter 3

Assessment of standard neutron techniques in cultural heritage

The aim of this study, performed as ANCIENT CHARM European project activity, was to identify strengths and weaknesses of neutron diffraction application to the study of archaeological objects and to develop a best practice for a combined use of neutron analysis methods (such us PGAA, TOF-ND, NT) for different combinations of materials.

For this purpose, 17 samples were used , known as *black boxes*, consisting in closed cubes containing geometrical arrangements of materials such as metals, minerals, ceramics, and organic matter.

The Time Of Flight Neutron Diffraction (TOF-ND) measurements, presented here, were carried out at the pulse neutron source ISIS at the Rutherford Appleton Laboratory in the United Kingdom.

3.1 Why *black boxes*: description of the samples

The contents of the 17 boxes were proposed by the archaeologists and conservators of the Hungarian National Museum, using typical materials often found in an archaeological context. Two sets of sealed *black boxes* were manufactured by the Hungarian National Museum and by the University of Bonn, respectively.
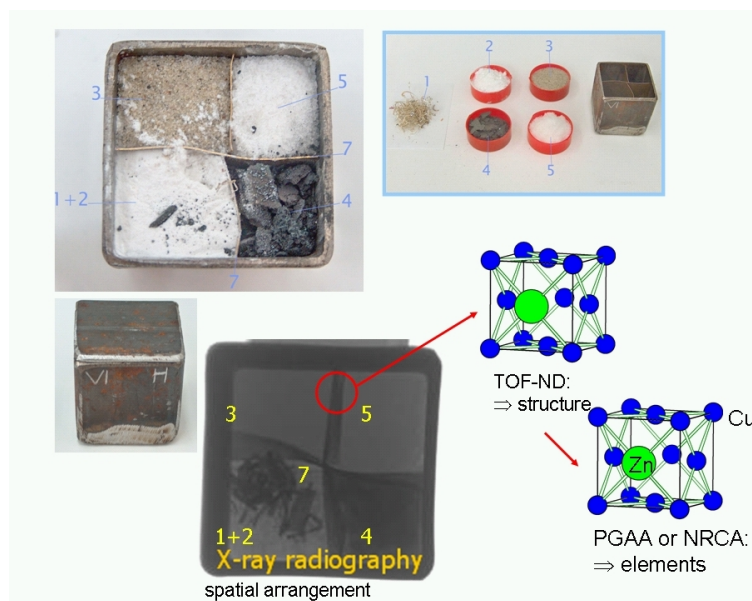

Figure 3.1: *Example of black box construction (H-VI) and X-ray radiograph. In this case neutron diffraction identifies a copper alloy fcc phase as the material of a dividing wall, whilst PGAA is necessary to detect the presence of zinc as alloying element.*

The first set consists of ten iron cubes of 40 mm edge length and labelled as H-I through H-X with the wall thickness of 1 mm [33], [34]. The second set is labelled as D-I through D-XI comprises eleven aluminum boxes with

wall thicknesses of 1 mm and dimensions edge length of 50 mm [35]. The compositions of the internal parts as well as the individual layouts were unknown to the scientists. The boxes present increasing levels of complexity, with geometrical 2D or 3D arrangements of different materials. The combination of different materials in a particular box was not always following realistic compositions in an archaeological context, but rather chosen to test the capabilities and limitations of the utilized neutron methods, by realizing varying degrees of complexity. In this sense, the *black boxes* served as samples for testing the different neutron methods and examining the degree to which the results from the different methods can be combined and made consistent.

Box	Instrument	Complementary methods
$D-II(Al)$	ROTAX	XR, NR
$D-IV(Al)$	ROTAX	PGAA,XR
$D-V(Al)$	ROTAX	PGAA, XR, NR
$D-VI(Al)$	ROTAX	PGAA
$D-VII(Al)$	ROTAX	PGAA, XR, NR
$D-VIII(Al)$	ROTAX	XR, NR
$D-IX(Al)$	ROTAX	XR, NR, NRCA
$D-X(Al)$	ROTAX	XR, NR
$D-XI(Al)$	ROTAX	-
$H-I(Fe)$	GEM,INES	PGAA, XR, NR
$H-II(Fe)$	GEM, INES	XR, NR
$H-III(Fe)$	GEM, INES	PGAA, XR, NR
$H-V(Fe)$	GEM	XR, NR
$H-VI(Fe)$	GEM, INES	PGAA
$H-VIII(Fe)$	GEM	PGAA, XR, NR
$H-IX(Fe)$	GEM, INES	XR, NR

Table 3.1: *Analysed black boxes at ISIS. Techniques used: Time-Of-Flight neutron diffraction (TOF-ND), Prompt Gamma Activation Analysis (PGAA), X-ray Radiography (XR), Neutron Radiography (NR).*

3.2 Neutron Diffraction study of *black boxes*

The TOF-ND measurements were carried out on the diffractometers ROTAX, GEM, and INES at the ISIS Facility, at the Rutherford Appleton Laboratory (Chilton, Oxfordshire, UK).

Although these instruments use the same type of technique they have different characteristics, performances and set-ups. There are, however, some common characteristics for all the measurements: the boxes were mounted on a platform or on a moving table inside a sample chamber to change the zone illuminated by the neutron beam and its direction relative to the samples own coordinate system. The data were collected at standard room temperature conditions and generally performed in air because, in this case, the air scattering turned out to be irrelevant. Neutron and X-ray radiographies were used as guides to select the most interesting points for TOF-ND analysis. The beam size was typically $10 \times 10 \ mm^2$ except for INES where a beam of $40 \times 40 \ mm^2$ was used. Alignments were by eye, data collection times lasted between minutes and two hours at most, and data were collected with all available detectors of the instruments. Correspondingly, in the analysis, all data were taken into account. There are well established procedures in crystallography, indeed, to study single-phase samples (powders or single crystals) and multi-phase samples in case of well defined diffraction geometry. In comparison, the analysis of the *black boxes* data presents a much higher degree of complexity due to:

- interference of different materials, crystalline and amorphous, inside a box; powders, single crystals, textured materials, compounds of high and low symmetries,

- scattering contributions from sample parts off-set from the instrument centre i.e. the neutron data depend on which material is in front or in the rear of the box,

- materials with different absorption properties.

In this application, the *back-scattering* pattern has a special relevance because neutrons are scattered back into the detector and provide information even if the box contains highly absorbing material. For the forward-scattering banks the primary neutron beam, as well as the scattered neutrons, have to cross the full length of the sample so that forward scattering data are much more prone to absorption effects.
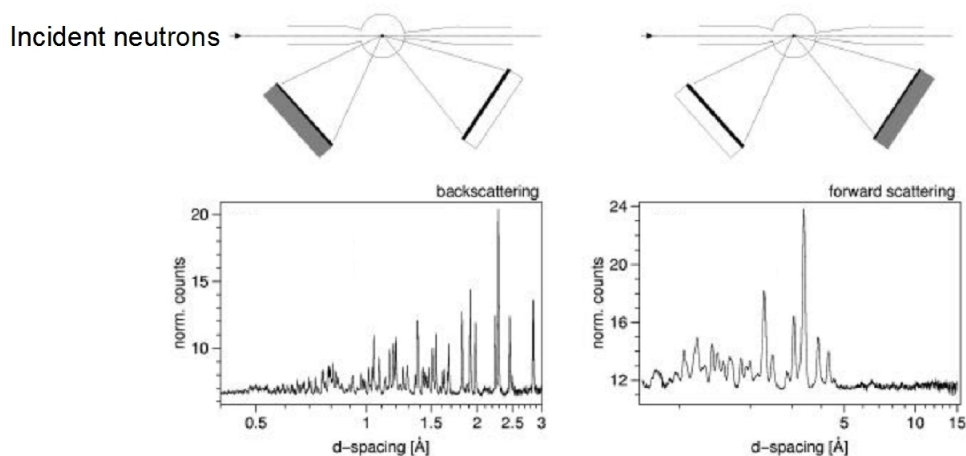

Figure 3.2: *Patterns collected with detectors at distinct angles provide different d-spacing ranges with diverse d-resolutions back-scattering and forward-scattering patterns.*

During the analysis some spectra presented a systematic peak-shift from the nominal center of the Bragg peak positions due to the sample-material displacement from the center of the geometry. Hence, the Bragg peaks from the walls of the cubes are shifted with respect to the nominal Al or Fe positions from databases. Then, in the case of a weak neutron-absorbing material inside the box, a double pattern at *back-scattering* and *forward-scattering* angles shows up.

Instead when the material is a strong neutron absorber, only single Al or Fe Bragg peaks are observed at backscattering angles. Hence the d-spacing shifts permit the identification of a phase and moreover these shifts can also be used to reconstruct the spatial distribution of the material in an extended object with the relation:

$$\frac{\Delta d}{d} = \frac{x cos\theta}{L_2} \tag{3.1}$$

where Δd is the distance between the observed and the nominal peak position, d is the d-spacing (measured in Å), L_2 is the distance between sample position and detector, and θ is the half of scattering angle.
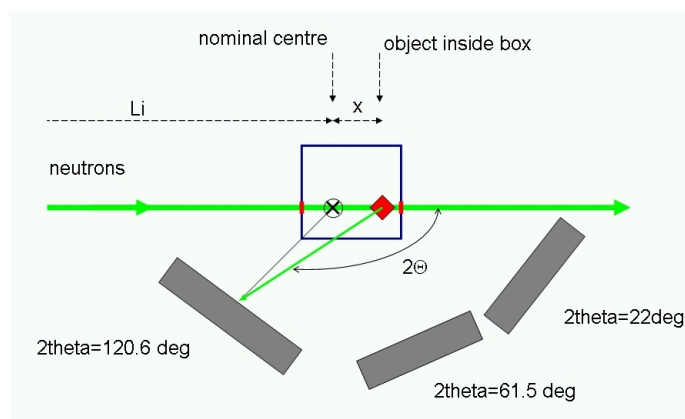
Figure 3.3: *Schematic experimental set-up and effect of the sample displaced (case of large samples) from the nominal center of the diffractometer.*

In the case of the *black boxes* analysis, the crystalline phases were identified by pattern comparison with a database of mineral and metal phases. The GSAS analysis suite is used to check the measured neutron patterns against theoretical single phase database patterns, and thus to confirm or reject the presence of an assumed phase. A full quantitative analysis is difficult and actually impractical due to the above described peak shifts caused by

off-focus scattering; in fact Rietveld programs cannot account for different off-centre displacements of different phases in the same data set.

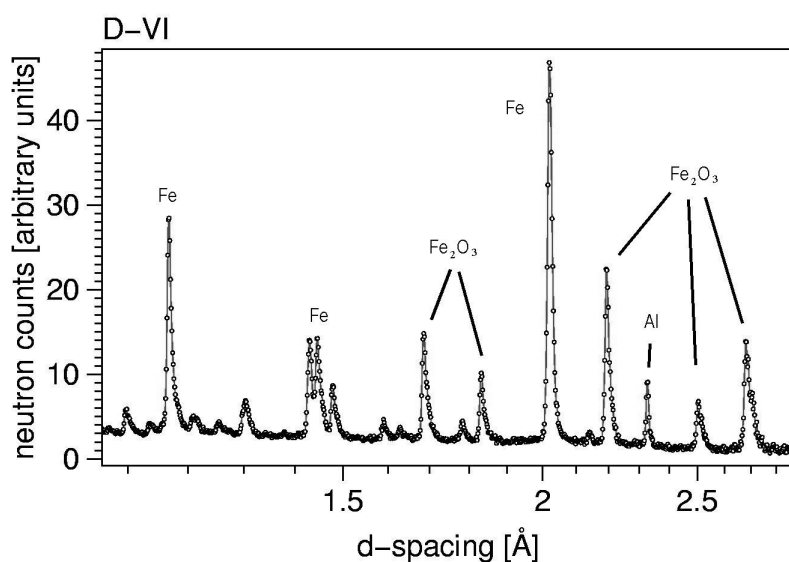Figure 3.4 shows a typical neutron diffraction pattern, here of box D-VI, which contains iron and hematite (Fe_2O_3).

Figure 3.4: *A TOF-ND pattern of black box D-VI.*

The neutron diffractogramm is characterized by Bragg peaks which are quantitatively analysed in terms of peak-intensities, peak-positions and pick-widths. The data contain information on the crystal structures and magnetic structures (hematite is magnetic at room temperatures) as well as on the texture (the orientation distribution of the crystallites in the material). Non-crystalline components or amorphous materials, typically organic materials, do not give rise to Bragg peaks but produce a noticeable high background in the diffraction data originating from the incoherent scattering of hydrogen atoms.

Neutron diffraction is sensitive to modifications of a compound, as well as its corrosion products or structural differentiation. For instance, the face centered cubic (fcc) structure of alpha-brass and the body centered cubic (bcc) structure of the beta-brass phase are noticeable.

For many metal structures, which crystallize in the fcc-lattice, instead, the diffraction patterns appear very similar and a high resolution instrument is needed to distinguish one of each other. Then, the differences between diffraction patterns are only recognizable from slightly different peak positions due to different lattice parameters. Usually, with an optimized geometry, the unit cell parameters of compounds can be determined by TOF-ND with high accuracy.

Because of the peak shifts, the measurements of lattice parameters is less accurate, and differentiation between some fcc structures becomes difficult. In this case, for example, the structures of copper (Cu, $a = 3.6145$ Å) and steel ($a = 3.608$ Å), or to aluminum (Al, $a = 4.048$ Å), silver (Ag, $a = 4.086$ Å) and gold (Au, $a = 4.078$ Å) are indistinguishable. In such situations, it is crucial to have results from some other techniques, such as PGAA, in order to determine the correct metal phase. The lattice parameter of the fcc cell determined with GSAS from the *black boxes* data gives a first indication of the composition of the lattice. Incorporation of an element, such as tin or zinc, into the copper lattice expands the unit cell according to the size of the guest atoms (Sn is larger than Zn).

3.3   Results and conclusions

All results of ND are presented in tables contained in the appendix of this chapter. For most of them, radiographies were available at the time of the ROTAX and GEM experiments, and they were used to guide the ND measurements. Also, PGAA results were available during ND analysis, and they helped to identify some of the components inside the boxes. The layouts and the material compositions of the boxes disclosed after the analysis could be compared to the diffraction analysis results. The first part of the table (a) in the appendix, presents the results of the neutron diffraction analysis; the second part (b) compares the results from ND and PGAA [36] with the actual compositions of the boxes (reality check).

In a lot of cases, ND measurements have added complementary information to radiographies and PGAA data. For box D-II, for example, TOF-ND discovered a beta-brass alloy inside one of the copper alloy spirals. This result could only be achieved by neutrons which penetrate into the core of the wire. X-ray diffraction detected the beta-phase in the wire interior only after grinding a piece of wire. Still, the neutron diffraction cannot tell if the beta-brass phase is in the core or in the surface of the wire due to the insufficient spatial resolution. Cementite (Fe_3C) peaks were identified in the iron rods of box $D-IV$. Different iron modifications (ferrite, steel) and iron oxides (FeO, Fe_2O_3, Fe_3O_4) are differentiated, as demonstrated for $D-VI$ and $H-VI$. ND, in combination with PGAA, distinguishes between copper alloys and copper phases.

All these examples demonstrate the neutron diffraction potential for the characterization of archaeological objects. A good practice can be obtained only combining the element analysis methods (PGAA) and the phase analysis method (TOF-ND). In many cases, the diffraction analysis was hindered by the complexity of the diffraction data, originating from the superposition of patterns from different parts of a box, when the neutron beam had been cross-

ing several components. This shows that the beam size and the contributing irradiated volume need to be smaller.

The *black boxes* results highlight some aspects for analysis of archaeological objects with neutrons. Neutron analysis are non-destructive and provide information from the interior of the boxes with a low spatial resolution (typically 0.1 mm), compared with other methods. The *black boxes* analysis suggest a best procedure for non-destructive analysis of objects:

1. A conventional surface analysis technique such as walls in the case of the boxes, is necessary to characterize the outside of the objects, in order to distinguish the surface from the bulk components.

2. X-ray radiography or neutron tomography produce high-resolution 2D/3D images that show the internal geometrical structure and attenuation features in quantitative terms. Radiographic data prior to the diffraction experiments are essential to guide the ND structure analysis. In many cases, X-ray radiographies will be sufficient. In-situ neutron radiography to guide the experiments would be useful.

3. The analysis have to be performed using a unique object coordinate system, ensuring reproducible orientation.

4. The collection of elemental data by PGAA and/or NRCA is essential for a proper identification of materials.

3.4   Appendix

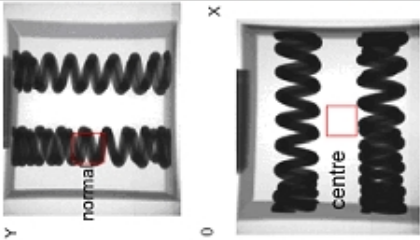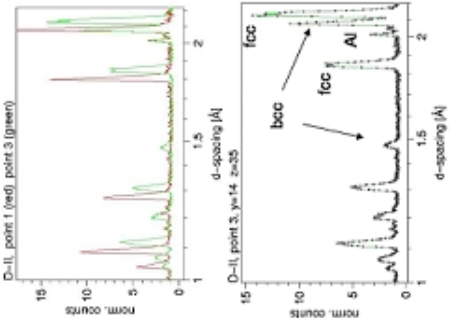*Table 1 (a). TOF Neutron Diffraction results on D-II*

Box no.	X-ray radiograph	Set-Up	Diffraction patterns	ND results
D-II		**Instrument: ROTAX** beam size 10x10 mm; beam along y Central box alignment: no offset; P1-P4: aligned with incident beam. "normal": incident beam normal to the spiral. Beam traverses two spirals P3-P4. no offset "centre": incident neutron beam aimed at box centre to determine filling. no offset		**Point 1:** fcc a $=3.60$ Å (Cu-type); **Point 2:** fcc a $=3.601$ Å (Cu-type) **Point 3:** fcc a $=3.69$ Å (Cu-type) (80wt%); bcc-phase (20wt%), a $=2.94$ Å **Point 4:** fcc a $=3.686$ Å (Cu-type) (85wt%), bcc-phase (15wt%), a $=2.95$ Å **Centre:** beam along z, empty (only Al peaks) **Normal** to the spiral, beam along z: fcc a $=3.690$ Å (Cu-type) (85wt%), bcc-phase (15wt%) a $=2.94$Å

Table 1 (b). Comments on TOF-ND results on D-II

Box no.	Box content from TOF-ND	Complementary info	Reality Check
D-II	- Springs made of different materials but combination of two phases (fcc+bcc) - The lattice parameter indicates a **copper alloy** (bronze/brass) for the fcc metal, and beta-brass for the bcc-phase. The peak shift of the copper alloy (fcc phase) compared to 1+2 is clearly visible in the diffraction patterns. The 'normal shot' went through 3+4, and confirms results on point P3+P4 Lattice parameter of bronze/brass: a $=3.686$ Å. This value can be interpreted as $Cu_{0.7}Zn_{0.3}$ brass ($=40$wt% Zn) or a bronze $Cu_{0.93}Sn_{0.07}$ ($=12$wt% Sn). These cases are indistinguishable. - no filling materials	none	- The springs are made of Cu and brass. The brass consists of $Cu_{64}Zn_{36}$, with alpha-brass on the surface and beta-brass in there wire core. TOF-ND identifies the different phases of the two types of springs: two Cu-type phases with different lattice parameters. - TOF-ND also **identifies** the beta-brass component (bcc-phase) which is consistent with the Cu-Zn phase diagram for a $Cu_{60}Zn_{40}$ brass.

Table 2 (a). TOF Neutron Diffraction results on D-IV

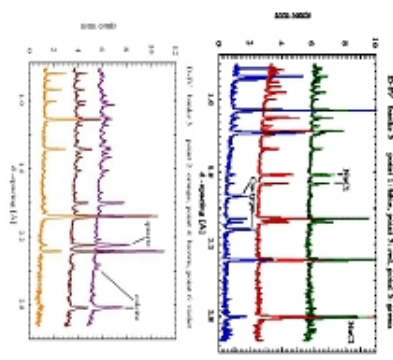| Box no.	X-ray radiograph	Set-Up	Diffraction patterns	ND results
D-IV		**Instrument: ROTAX** beam size 10x10 mm; beam along z box alignment: P1-P6 aligned with incident beam; no offset		Point 1: NaCl, Cu-type (fcc) a=3.592 Å, steel (Fe) or copper (Cu) Point 2: bcc a=2.845 Å, ferrite (Fe) +cementite (Fe_3C), in clay=calcite+quartz Point 3: NaCl, small fcc peaks a=3.6 Å, steel (Fe) or copper (Cu) Point 4: calcite, quartz, bcc a=2.845 Å, ferrite (Fe) Point 5: NaCl Point 6: calcite (75wt%), quartz (25 wt%)

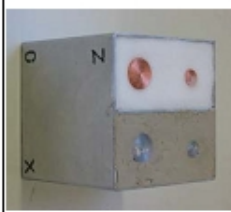*Table 2 (b). Comments on TOF-ND results on D-IV*

Box no.	Box content from TOF-ND	Complementary info	Reality Check
D-IV	- Two compartments with different filling materials: salt (NaCl) and clay consisting of quartz (25 wt% SiO_2) and calcite (75wt% $CaCO_3$). - **The objects** in the two chambers are made of different materials: 1: fcc-structure, Cu-type (fcc structure); lattice parameter (a=3.592 Å) is closer to steel (3.594 Å) than to copper (3.615 Å) 2: Bcc lattice, ferrite (Fe); extra cementite (Fe_3C) peaks; clay peaks are small compared to the Fe peaks; 3: fcc-structure, Cu-type (fcc structure); lattice parameter (a=3.592 Å) indicates steel 4: The rod material is bcc-Fe (ferrite)	- **PGAA** identifies fcc-metal as **Cu** for points (1) and (3) - **PGAA** identifies Al as separator material.	Cu and Iron rods, embedded in halite (NaCl) and clay (51% calcite, 20% quartz, 12% muscovite, 17% kaolinite) - The main components are identified by TOF-ND. - PGAA is required to decide on the fcc-material: copper. - For the clay the two main components were identified with approximately the correct proportions. - After disclosure of the content, kaolinite is identified in the pattern. - Muscovite was not detected by TOF-ND. - The lattice parameters of Cu and Fe are systematically shifted towards lower values. This is probably due to absorption (i.e. apparent shift of the material towards the neutron source.) - **Extra phase**: Cementite is observed in the ferrite. - The second wall of the box is not visible for both filling materials. The Cu rod in position 3 was almost missed by the neutron beam due to misalignment of the box on the instrument.

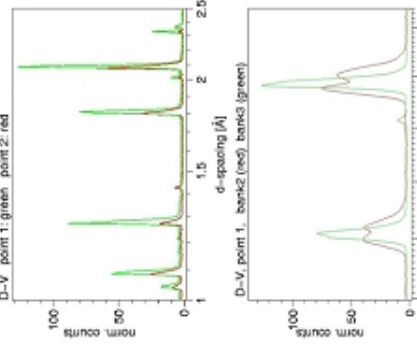*Table 3 (a). TOF Neutron Diffraction results on D-V*

Box no.	X-ray radiograph	Set-Up	Diffraction patterns	ND results
D-V		**Instrument: ROTAX** Point 1: beam size 10x10 mm; beam along y Point 2: beam size 10x10 mm; beam along z box alignment: P1-2 aligned with incident beam; no offset		**Point 1:** Cu-type (*fcc*), a=3.608 Å **Point 2:** Cu-type (*fcc*), a=3.598 Å

Table 3 (b). Comments on TOF-ND results on D-V

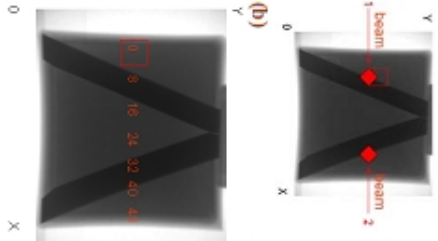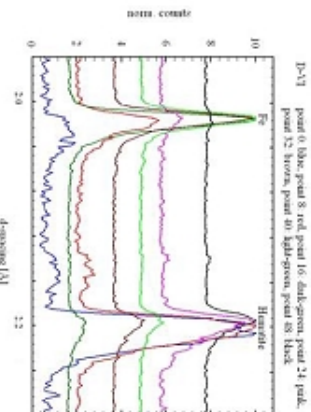| Box no.	Box content from TOF-ND	Complementary info	Reality Check
D-V	- The two analysis points show the same set of peaks, i.e. all the parts of the internal object are made of the same material; - The object is made of an fcc material with Cu type structure; the lattice parameters point to steel rather than copper but peaks can be shifted due to displacement of the object inside the box. - The rest of the box is **empty**. - Inspection of the diffraction patterns shows the following features: **1.** Fcc Cu-type material is textured (preferred orientation of grains) **2.** The aluminium peak intensities are different for point 1 and point 2 due to absorption of neutrons in the copper **3.** Splitting of peaks in bank-2 (double pattern) indicates transition of beam through two walls.	- **PGAA** identifies fcc-metal as **Cu**.	 - The **objects** consist of **pure copper**. - The main phase is identified by TOF-ND. PGAA differentiates between steel and Cu.

Table 4 (a). TOF Neutron Diffraction results on D-VI

Box no.	X-ray radiograph	Set-Up	Diffraction patterns	ND results
D-VI	(a) (b)	**Instrument: ROTAX** (a) Point 1: beam size 10x10 mm; beam along x Point 2: beam size 10x10 mm; beam along minus x (b) Scan along x [mm]; beam size 10x10 mm; beam along z box alignment: no offset		(a) **Point 1**: Hematite (Fe$_2$O$_3$), bcc type structure, a=2.86 Å, ferrite (Fe) **Point 2**: Hematie (Fe$_2$O$_3$) , bcc type structure, a=2.85 Å, ferrite (Fe) (b) **Point 0**: Fe$_2$O$_3$ (Hematite), wall **Point 8**: Fe$_2$O$_3$ (17wt%), ferrite (83wt%) **Point 16**: Fe$_2$O$_3$ (86 wt%), ferrite (14 wt%) **Point 24**: Fe$_2$O$_3$ (94 wt%), ferrite (6 wt%) **Point 32**: Fe$_2$O$_3$ (38wt%), ferrite (62wt%) **Point 40**: Fe$_2$O$_3$ (37wt%), ferrite (63wt%) **Point 48**: Fe$_2$O$_3$ (100wt%) ferrite (0 wt%)

Table 4 (b). Comments on TOF-ND results on D-VI

Box no.	Box content from TOF-ND	Complementary info	Reality Check
D-VI	- The two inclined 'plates' are of the same **material**: ferrite (bcc-Fe); - The x-scan shows that the V-shape object is **ferrite** and that the box is **filled with hematite** (not the other way round).	- **PGAA** confirms presence of Fe and absence of other elements; 	- The main components (ferrite and hematite) are identified. - This box highlights the **advantage of TOF-ND** compared to element-sensitive methods: oxides, corrosion phases, secondary alteration phases can be distinguished from alloys.

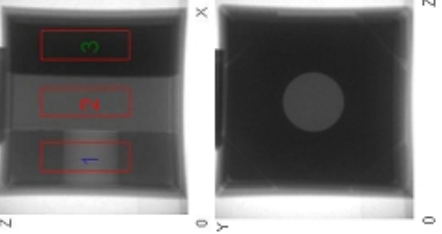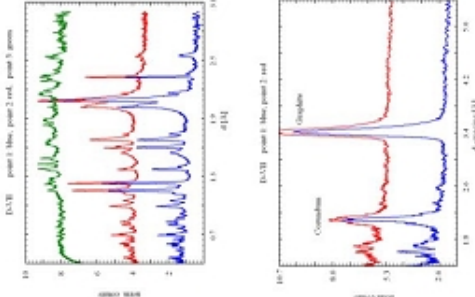*Table 5 (a). TOF Neutron Diffraction results on D-VII*

Box no.	X-ray radiograph	Set-Up	Diffraction patterns	ND results
D-VII		**Instrument: ROTAX** beam size 10x30 mm; beam along y box alignment: no offset		**Point 1**: graphite (C) + corundum (Al_2O_3) in equal parts **Point 2**: graphite (C) + corundum (Al_2O_3) in almost equal parts **Point 3**: phase not identified

Table 5 (b). Comments on TOF-ND results on D-VII

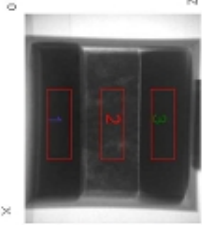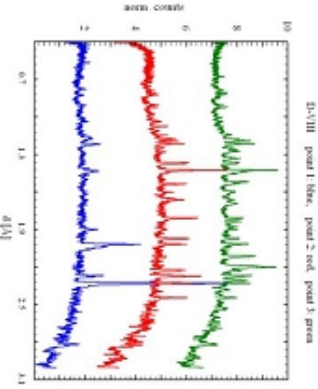| Box no.	Box content from TOF-ND	Complementary info	Reality Check
D-VII	- Analysis **points 1 and 2** are made of the **same material**: graphite and corundum. - Analysis **point 3** shows a rich spectrum of diffraction peaks. The pattern could not be unravelled, or assigned to a single phase.	- **PGAA** identifies **Na** which may come from diaoyudaoite ($Al_{10.33}$ $Mg_{0.65}O_{16}(Na_{1.65}O)$ - **PGAA** identifies **Si** and **H** which comes from pyrophyllite	 - **Graphite and corundum were identified.** - The peaks of diaoyudaoite ($Al_{10.33}$ $Mg_{0.65}O_{16}(Na_{1.65}O)$ at 11.2 and 5.7 Å were observed but the compounds was not identified. - The peak-rich pattern of pyrophyllite was recognised, but the mineral was not identified. - The simultaneous observation of graphite and corundum in equal amounts for point 1 and point 2 indicates a substantial **misalignment** of the box on the diffractometer, or wrong axes description on the radiographies.

Table 6 (a). TOF-Neutron Diffraction results on D-VIII

Box no.	X-ray radiograph	Set-Up	Diffraction patterns	ND results
D-VIII		**Instrument: ROTAX** beam size 30x10 mm; beam along y box alignment: no offset		**Point 1:** calcite ($CaCO_3$), high background **Point 2:** quartz (SiO_2), on high amorphous background **Point 3:** quartz (SiO_2)(25wt%), mullite $3Al_2O_3\,2SiO_2$ (55wt%), cordierite $Mg_2Al_4Si_5O_{18}$ (10wt%), cristobalite (SiO_2) (5wt%), identified in the data after box content is revealed; other un-indexed peaks on high background level

Table 6 (b). Comments on TOF-ND results on D-VIII

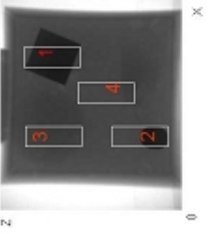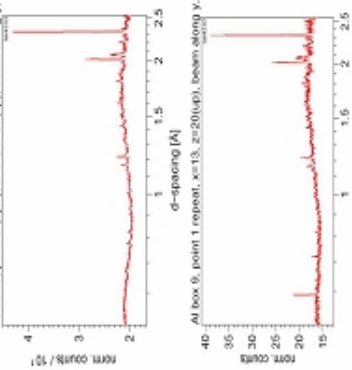| Box no.	Box content from TOF-ND	Complementary info	Reality Check
D-VIII	- **Point 1** shows a very high hydrogen background indicating mineral with H-content; the beam is stopped in the box, there are no Al-peaks from the back aluminium wall of the box; there are practically no peaks in forward scattering. The main component is calcite. - In **Point 2** quartz is identified. - **Point 3** has a large amorphous background, most likely due to H-containing substance/mineral, or glassy component. The patterns contain Bragg peaks from quartz, mullite, cordierite and cristobalite. A large peak at 2.84 Å is unidentified.	- **PGAA** identifies hydrogen on all points, in agreement with the neutron background, in contrast to x-ray analysis.	- **P1** is on a slab of clay. TOF-ND sees the main component, calcite. The clay seems to be more hydrogenous than in D-IV. - **P2** is on a slab of brick stone (quartz, albite, muscovite, hematite). TOF-ND sees only main component, quartz. - **P3** is on a slab of fire brick (schamotte) (mullite, quartz, cordierite). The phases mullite, cordierite were not identified from the observed peak-rich spectrum because the peaks were only from backscattering. (Mineral phases are best identified in forward scattering). Once the box content was revealed, the phase fractions from TOF-ND are in the right order of magnitude.

Table 7 (a). TOF Neutron Diffraction results on D-IX

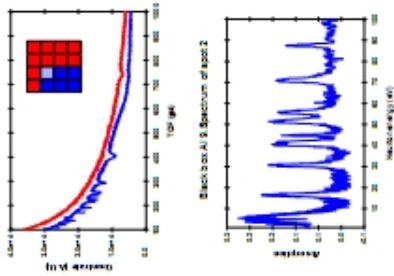| Box no.	X-ray radiograph	Set-Up	Diffraction patterns	ND results
D-IX		**Instrument: ROTAX** beam size 10x30 mm; beam along y box alignment: P1-P4 aligned with incident beam; offset on diffractometer according to radiography		**Point 1-4:** gypsum, high amorphous background

Table 7 (b). Comments on TOF-ND results on D-IX

Box no.	Box content from TOF-ND	Complementary info	Reality Check
D-IX	- All patterns exhibit a very high (hydrogen) **background**, i.e. indicate compounds with hydrogen. - The patterns only show the front wall of the Al-cube, i.e. the beam is stopped within the box. - There are **weak peaks** in the patterns from the filling material (they are in all patterns). The filling material is not identified. - **P1** has extra single crystal peaks in backscattering at low d-spacing; not possible to index with low d-value lines;	- **NRCA** analysis on INES identifies the Ag rod on point 2. 	- Box is filled with gypsum (CaSO$_4$ (H$_2$O)$_2$). - Embedded are: 1. pyrite single crystal (FeS2) in point 1 2. Silver rod in point 2 3. Glass sphere in point 3 4. Quartz crystal in point 4 - The extra peaks of the filling material are only identified after disclosure of the box fillings. - The single crystal peaks of FeS$_2$ are visible in the data but were not identified. - no identifiable signals from the other objects in the box. The glassy signal from the glass object is covered by the gypsum scattering. Ag-peaks in TOF-ND data are hidden under the Al peaks.

Table 8 (a). TOF Neutron Diffraction results on D-X
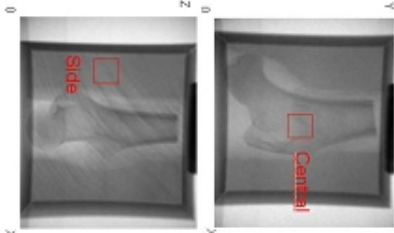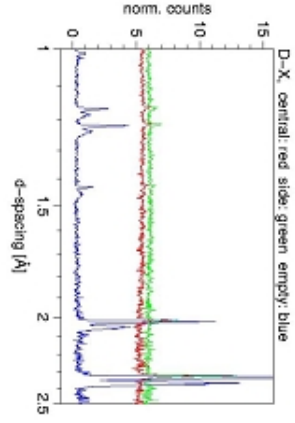
Box no.	X-ray radiograph	Set-Up	Diffraction patterns	ND results
D-X		**Instrument: ROTAX** beam size 10x10 mm; box alignment no offset	D-X, central: red side: green empty: blue	**Central:** beam along z; high background scattering **Side:** beam along y; high background scattering

Table 8 (b). Comments on TOF-ND results on D-X

Box no.	Box content from TOF-ND	Complementary info	Reality Check
D-X	- The diffraction patterns do show Al peaks from the box wall, but only from one wall. - The aluminium peaks are only in backscattering; - Therefore the box cannot be empty. There are no peaks of bone material. - The high neutron background indicates scattering by hydrogen; the hydrogen can be in the bone (visible in x-ray radiography) but there may also be filling material around the bone;	none	- Badger bone, inside beech wood, lower part of bone wrapped in leather; - TOF-ND cannot provide information due to missing crystallinity of the material.

Table 9 (a). TOF Neutron Diffraction results on D-XI

Box no.	X-ray radiograph	Set-Up	Diffraction patterns	ND results
D-XI		**Instrument: ROTAX** beam size 10x30 mm; box alignment: no offset		Doublets of Al peaks from front and back-wall scattering

Table 9 (b). Comments on TOF-ND results on D-XI

Box no.	Box content from **TOF-ND**	Complementary info	Reality Check
D-XI	- We observe diffraction patterns from the **front wall** and from the **back wall**. The patterns show the fcc structure of aluminium. Moreover, the patterns show a drastic texture (preferred grain orientation of the Al grains). - The **distance** between the **double peaks** is related to the distance between front and back wall of the box (x): $\Delta d/d = x \ast \cos(\theta) / L_2$ where Δd is the distance between two peaks in Å, L_2 the distance between sample position and detector, and where θ is ½ the detector angle. - The **intensities** of the **peaks** from the back wall are much reduced compared to the peak intensities from the front wall due to absorption.	none	- **Empty box**, made of aluminium. The front and back walls are x=50 mm apart. Wall thickness 1 mm.

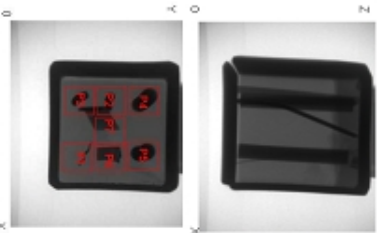*Table 10 (a). TOF Neutron Diffraction results on H-1*

Box no.	X-ray radiograph	Set-Up	Diffraction patterns
H-1		**Instrument: GEM**; beam size10x10 mm; beam along z (top side towards beam, side with number "1" facing down) box alignment: no offset	**P1**: copper or steel (small peaks) **P2**: copper a=3.62 Å, small copper alloy component a=3.7 Å, Al/Ag **P3**: copper alloy a=3.69 Å **P4**: fcc-phase a=3.7 Å: bronze or brass; Al/Ag **P5**: copper alloy, a=3.62 Å, Al/Ag, maybe Zn **P6**: fcc a=3.60 Å (copper or steel!), Al/Ag **P7**: fcc a=3.60 Å (small peaks) All diffraction patterns contains gypsum (CaSO$_4$(H$_2$O)$_2$) peaks.

Table 10 (b). Comments on TOF- ND results on H-1

Box no.	Box content from TOF-ND	Complementary info	Reality Check
H-1	The analysis points P1-7 reveal the following main materials (in addition to gypsum): **P1**: copper (Cu) or steel (Fe) **P2**: copper **P3**: brass or bronze **P4**: brass or brass **P5**: copper, indications of Zn; **P6**: copper or steel; strong Al/Ag peaks **P7**: indications of copper/steel peaks - All patterns show Al/Ag peaks, apart from P1, P6	- **PGAA** observed **Cu, Zn** and **Fe**; i.e. no Sn. This means, the copper alloy is most likely brass (Cu-Zn). - **PGAA** does not find Al or Ag.	1 - copper wire 2 - brass wire 3 - copper wire 4 - brass rod 5 - copper rod 6 - zinc plate 7 - iron plate on gypsum plate - Copper on **P1** was first overlooked, but peaks are present in data. **P1, P4, P5** were assigned correctly. - **P2, P3** analyses are wrong. **P2** was analysed as copper; small brass component is correct. **P3** was analysed as brass, but it is copper. Since copper and brass are easy to distinguish there seems to be an alignment error. Zinc on **P6** is not identified (Zn: peaks at 2.09, 2.31, 2.47 Å). There are small Zn peaks in **P2**. - **P7** shows fcc-phase, in agreement with steel. Pb peaks, identified in the first analysis, are from gypsum. - Ag/Al was identified but is not present.

Table 11 (a). TOF Neutron Diffraction results on H-11

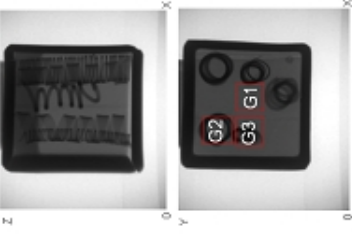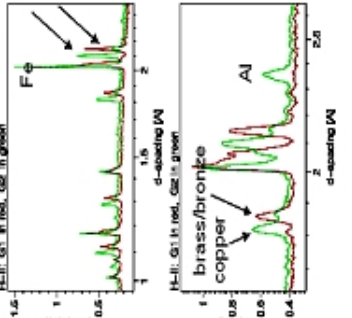| Box no.	X-ray radiograph	Set-Up	Diffraction patterns	ND results
H-11		**Instrument: GEM** beam size 10x10 mm; beam along z box alignment: no offset	 copper brass/bronze	"Filling" peaks gypsum: $CaSO_4(H_2O)_2$ **G1**: gypsum, strong copper alloy peaks (a=3.70 Å) **G2**: gypsum, strong copper/steel (a=3.62 Å), + weak copper alloy (a=3.70 Å) peaks; **G3**: gypsum, Al, copper alloy/steel phase (a=3.59 Å), strong Al/Ag

Table 11 (b). Comments on ND results (Black Box H-11)

Box no.	Box content from **TOF-ND**	Complementary info	**Reality Check**
H-11	- The **filling material** is gypsum. The box contains metallic springs, made of different materials: copper/steel and bronze/brass. - **G1** in the centre shows strong copper alloy peaks (bronze or brass), presumably from one of the springs. - **G2** shows a copper/steel fcc-phase, next to a much weaker bronze/brass phase. Extra strong peaks indicate Al/Ag. - **G3** shows a weak copper/steel phase. Extra strong peaks indicate Al/Ag. - The Cu/Al phases are not present in the forward scattering banks.	none	 **1** - brass spring **2** - brass spring **3** - copper spring **4** - brass spring **5** - copper spring - The springs were correctly identified as metal (bronze or brass) springs. - The points G1 was intended as a shot in the centre to determine the filling material. The presence of copper in the data indicates a "failed shot". - G2 (brass) is wrongly assigned as copper. G3 (Cu) is correct. - Beta brass components are not detected. - Gypsum was not identified as a plate, but as a powder filling. This could have been detected by comparing the patterns to the ones of other gypsum-filled boxes. There could be a mis-orientation of the box on the instrument.

Table 12 (a). TOF Neutron Diffraction results on H-III

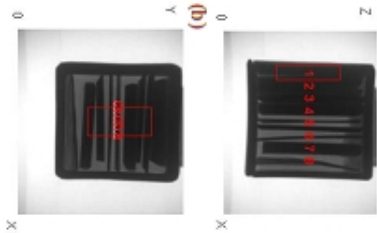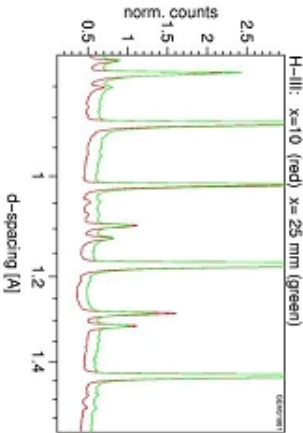| Box no.	X-ray radiograph	Set-Up	Diffraction patterns	ND results
H-III	**(a)** **(b)**	**Instrument: GEM** **(a)** beam size 5x20 mm; beam along y (side with number H-III facing incoming beam) **(b)** Beam size 10x20 mm; beam along z box alignment: no offset	 H–III: x=10 (red) x= 25 mm (green)	**(a)** Point 1: x=5, copper alloy 1 (a=3.618 Å), Point 2: x=10, copper alloy 1 (a=3.614 Å), Point 3: x=15, copper alloy 1 (a=3.613 Å), copper alloy 2 (a=3.70 Å) Point 4: x=20, copper alloy 1 (a=3.613 Å), copper alloy 2 (a=3.70 Å) Point 5: x=22.5, copper alloy 1 (a=3.613 Å), copper alloy 2 (a=3.70 Å) Point 6: x=25, copper alloy 1 (a=3.613 Å), copper alloy 2 (a=3.70 Å) Point 7: x=30, copper alloy 1 (a=3.613 Å), copper alloy 2 (a=3.70 Å), Point 8: x=32.5, copper alloy 1 (a=3.613 Å), copper alloy 2 (a=3.70 Å) **(b)** Point Centre: copper alloy 1 (a=3.615 Å), copper alloy 2 (a=3.70 Å)

Table 12 (b). Comments on TOF-ND results on H-III

Box no.	Box content from TOF-ND	Complementary info	Reality Check
H-III	- The data show the same phases (copper-type phase, copper alloy phase) for all points, in similar phase ratios. - The copper-type phase (a=3.613 Å) can be steel or copper. - The copper alloy (a=3.7 Å) can be bronze or brass. - There is **no filling material identified**.	- **PGAA** data show copper and iron as elements. The PGAA scan identifies the copper-type phase as copper. No filling material is detected. - **PGAA** identifies the copper alloy with the larger lattice parameter as brass.	 1 - copper sheet 2 - iron sheet 3 - brass sheet 4 - copper sheet 5 - iron sheet 6 - brass sheet 7 - iron sheet 8 - brass sheet 9 - steel sheet - All TOF-data show the same pattern. It has to be assumed that the scan was not, as planned, across the different plates. Maybe the incoming beam was impinging on the flat side of the sheets. - TOF-ND does not (easily) recognise an iron object in an iron box, although it is principally possible to separate the inside-objects via peak shift analysis. - TOF-ND failed to identify the steel sheet (9.

Table 13 (a). TOF Neutron Diffraction results on H-IV

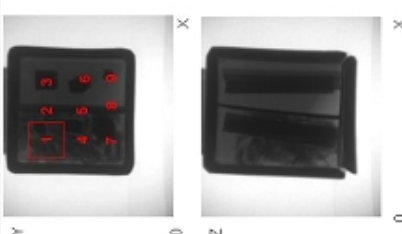| Box no.	X-ray radiograph	Set-Up	Diffraction patterns
H-IV		**Instrument: GEM** beam size 10x10 mm; beam along z (top side facing incoming beam, side with numbers down) box alignment: no offset	All patterns exhibit: quartz (SiO_2), gypsum $CaSO_4(H_2O)$, copper alloy ($a=3.654$ Å), **Point 1:** Quartz (12%), gypsum (7%), copper alloy (3%), Al/Ag (1%), FeO (3%), Fe_3O_4 **Point 4:** Quartz (17%), gypsum (5%), copper alloy (2%), FeO (2%), Fe_3O_4 **Point 7:** Quartz (11%), gypsum (6%), copper alloy (2%), FeO (2%) **Point 2:** Quartz (26%), gypsum (7%), copper alloy (3%), Al/Ag (5%), FeO (1%) **Point 5:** Quartz (27%), gypsum (7%), copper alloy (3%), Al/Ag (2%) **Point 8:** Quartz (17%), gypsum (7%), copper alloy (3%) **Point 3:** Quartz (31%), gypsum (6%), copper alloy (3%), Al/Ag (13%) **Point 6:** Quartz (27%), gypsum (6%), copper alloy (2%), Al/Ag (12%) **Point 9:** Quartz (20%), gypsum (5%), copper alloy (3%))

Table 13 (b). Comments on TOF-ND results on H-IV

Box no.	Box content from TOF-ND	Complementary info	Reality Check
H-IV	- The box is divided into **two parts**. All data show quartz and gypsum. However, P3, P6, P9 contains much more quartz. - The **copper alloy** can be brass (17wt% Zn) or bronze (5 wt% Sn). This component is high for P2,5,8, and low otherwise, indication that the separating sheet is made out of copper alloy. - **Copper alloy** contents are small.	- PGAA idenfies Fe and Mn, with the latter probably in the ferrite. - PGAA identifies Al, rather than Ag. - One filling material contains Si and B (?) as main component (SiO_2). The other filling material contains Fe as main component. - PGAA identifies Cu, in agreement with the TOF-data.	 **1, 2, 3** - iron **4** - thin steel plate **5** - fill grit **6** - fill sand - TOF-ND does not easily recognise a ferrite object in a box made of ferritic iron, although it is principally possible to separate the inside-objects via peak shift analysis from the wall material. - The gypsum was not identified as a plate, but as a powder filling. Has quartz spilled into left side of the box? Where is Al and Cu in the box? The nominal elemental composition is: Fe, Mn, C, B, Al, Si, K, Ti

Table 14 (a). TOF Neutron Diffraction results on H-V

Box no.	X-ray radiograph	Set-Up	Diffraction patterns	Box no.
H-V	(a) (b)	**Instrument: GEM** (a) beam size 10x20 mm; beam along y (b) beam size 10x10mm; beam along z box alignment: no offset	*(diffraction plot: H-V point 1 (red) point 2 green; labels Cu/Zn, Cu/Sn, Fe, Pb, Sn, Cu; norm. counts vs d-spacing [Å])*	(a) **P1+2**: gypsum CaSO$_4$ (H$_2$O)$_2$ (small peaks), Pb, Sn, copper alloy (a=3.7 Å) (b) **P3**: gypsum CaSO4 (H2O)2 (strong peaks), Pb, Sn, copper alloy (a=3.63 Å), Al/Ag (small)

Table 14 (b). Comments on TOF-ND results on H-V
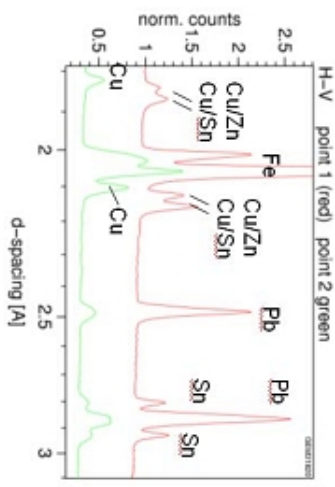
Box no.	Box content from TOF-ND	Complementary info	Reality Check
H-V	- The box contains gypsum (filling). - There is a combination of metals: Pb, Sn, copper alloy, Al/Ag. - **P1** shows split bronze/brass peaks, but **P3** not. Therefore the bronze/brass might be the outermost ring; the copper alloy peaks are different for P1 and P3. - The Pb peaks are split in P2. Therefore Pb could be the second-outermost metal in the box. The Sn could be part of a Pb/Sn solder. - There is a **peak at 2.34 Å** in P3 which indicates a fcc metal such as Al or Ag/Au. Pb and Sn are present in the center as well. - **P3** shows the 2.34 Å peak while it is hardly visible in P1. Therefore is can be assumed that Al/Ag/Au is the innermost metal in the box.	none	- The outer ring was correctly identified as copper alloy. Cu/Sn and Cu/Zn cannot be distinguished by TOF-ND. - The Pb ring was correctly identified. - The different copper alloy for P3 corresponds to the (short) copper ring which is out of sight in P1. The Cu lattice constant from TOF-ND is too large. - The inner metal is Pb/Sn eutectic which gives separate Pb and Sn peaks. Pb/Sn inside a Pb-sheet is difficult to see. - Al/Ag was wrongly identified as the centre object. Is there a top Al plate? - The gypsum peaks are smaller in P1-2 compared to P3 because there is just the bottom gypsum plate. Gypsum peaks in P3 remain unexplained 1 - brass plate 2 - lead plate 3 - copper tube 4 - thin lead solider Mounted on a gypsum plate

Table 15 (a). TOF Neutron Diffraction results on H-V1
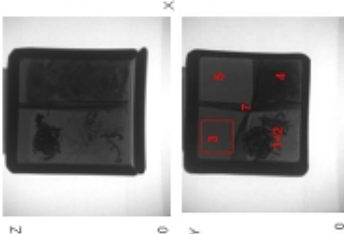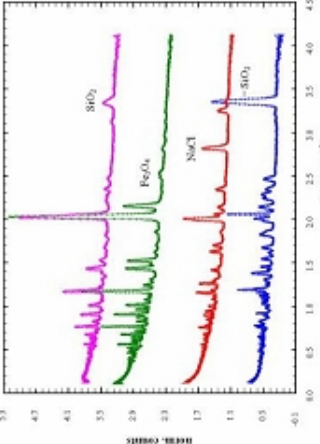
Box no.	X-ray radiograph	Set-Up	Diffraction patterns	Box no.
H-V1		**Instrument: GEM** beam size 10x10 mm; beam along z box alignment: no offset	From bottom to top: P3, P5, P4, P1+2	**P1+2:** quartz (SiO_2), gypsum ($CaSO_4(H_2O)_2$), talc ($Mg_3(OH)_2$ (Si_4O_{10}), Al or Ag **P3:** quartz, gypsum, talc, Al/Ag, fcc-Cu-type (a=3.7 Å) **P4:** gypsum, talc, fcc-Cu-type (a=3.7 Å), Magnetite (FeO_4), maybe FeO; **P5:** quartz, gypsum, halite (NaCl), gypsum, talc, fcc Cu-type (a=3.7 Å) **P7:** gypsum, halite, talc, fcc Cu-type (a=3.7 Å), Al/Ag, FeO

Table 15 (b). Comments on TOF-ND results on H-V1

Box no.	Box content from TOF-ND	Complementary info	Reality Check
H-V1	- The radiography shows that the box is divided into 4 sectors. - There are a number of peaks that are common to **all sectors**, either because it is a filling material or a wall material: gypsum, Al, talc (peaks at 9.6, 4.56 3.13 Å). - There is the following additional material in the *4 chambers:* • Main phase in **P1+2:** Al/Ag • Main phase in **P3:** quartz • Main phase in **P5:** halite (NaCl) • Main phases in **P4:** iron oxides (FeO, Fe_3O_4)	- PGAA identifies Ag rather than Al. - PGAA confirms the presence of a copper alloy as the fcc-phase. - The presence of Zn indicates brass rather than bronze.	1 - silver wire 2 - fill talcum 3 - fill sand 4 - fill grit iron **5** - fill salt (NaCl) **6** – copper sheets **7** –aluminium sheet - The main components in the compartments were identified. - The fcc-copper phase has a lattice parameter that rather indicates brass than pure copper, confirmed by PGAA. - The brass sheets are visible in all data except for point 1+2 (larger sector) which indicates a slight problem with the alignment of the box. - TOF-ND shows talc in all sectors. This result may indicate a misalignment or it may indicate that talc powder leaked from 1+2 into other compartments

Table 16 (a). TOF Neutron Diffraction results on H-VIII
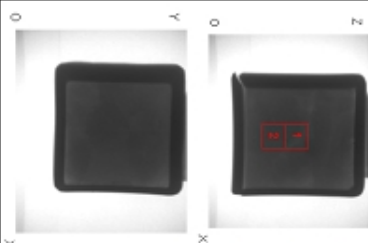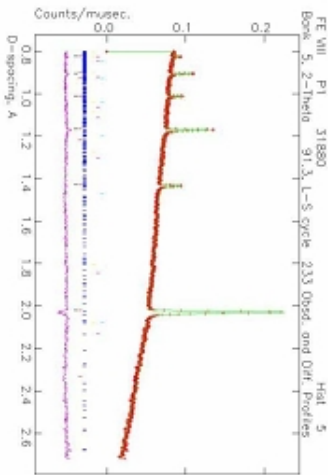
Box no.	X-ray radiograph	Set-Up	Diffraction patterns	Box no.
H-VIII		**Instrument: GEM** Beam along y; side with number "VIII" facing incoming beam box alignment: no offset		All diffraction patterns show single Fe peaks from the box walls. **Point 1:** moderate background **Point 2:** moderate background

Table 16 (b). Comments on TOF-ND results on H-VIII

Box no.	Box content from TOF-ND	Complementary info	Reality Check
H-VIII	- Only Bragg peaks of ferrite (front wall) are observed. - The beam does not pass through the box. - The box is filled with a neutron-stopping material. - TOF-ND "sees" no crystalline material. - The backgrounds in the neutron diffraction patterns are decreasing with increasing d-spacing (i.e. with increasing wavelengths). This is typical for absorbing or self-absorbing material (e.g. hydrogen-containing compounds).	- **PGAA** data suggest gypsum as main material (Ca, S, H). - Other elements from **PGAA** are Al, Si, K, Ti.	- Neolitic chaff tempered pottery; filling material is gypsum - The material inside the box is not identified. There are slight hints of gypsum peaks in the TOF-ND data. - The gypsum filler is impenetrable for the thermal neutron beam.

Table 17 (a). TOF Neutron Diffraction results on H-IX
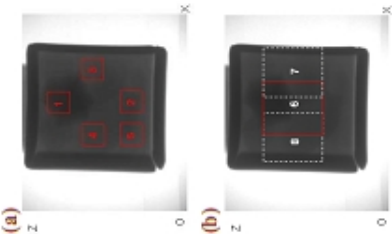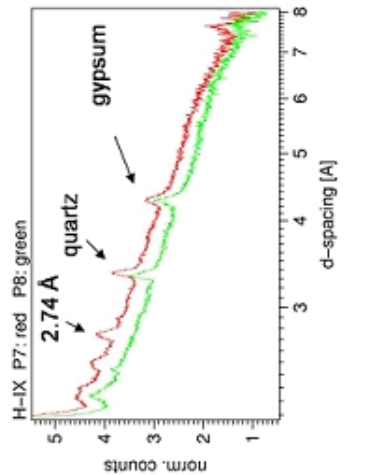
Box no.	X-ray radiograph	Set-Up	Diffraction patterns	Box no.
H-IX		**Instrument: GEM** Beam along y (side with number "IX" facing incoming beam) (a) Beam size: 10x10 mm (b) Beam size: 20x40 mm box alignment: no offset		Diffraction patterns show strong Fe peaks from front wall and weak peaks from back wall of the box. All points P1-P8 show gypsum $CaSO_4(H_2O)_2$ and quartz (SiO_2). **(a)** P1: extra characteristic peaks at 2.33, 3.31 Å P2: extra characteristic peaks at 2.50, 2.73 Å P3: extra characteristic peaks at 2.33, 2.73 Å P4: extra characteristic peak at 2.33 Å **(b)** P6: extra characteristic peaks at 2.44, 2.73, 3.31 Å P7: extra characteristic peak at 2.73 Å

Table 17 (b). Comments on TOF-ND results on H-IX

Box no.	Box content from TOF-ND	Complementary info	Reality Check
H-IX	- Apart from Fe peaks, there is a confusing pattern of Bragg peaks. All points show quartz and gypsum peaks (mixture of the two as filler). - **Gypsum** peaks are observed in forward scattering. This means that the neutrons are able to penetrate the box, in contrast to H-VIII. - The background in the neutron diffraction patterns is decreasing with increasing d-spacing (i.e. with increasing wavelengths). This is typical for a hydrogen-containing material, such as the gypsum filler). - 2.33 Å peaks in P1,3,4 indicate presence of Al/Ag.	none	 *1, 2 – achat 3 – amethyst 4, 6 – cornean 5 – blue glass 7-achat globular bead 8–turquoise 9 -pyrite* **Filler material: gypsum** - **Gypsum and quartz** are identified. Gypsum is the filling material, quartz is present in form of several localized objects rather than a filler. A finer scan would have revealed this. - **Achat and amethyst** are different varieties of quartz (SiO_2). - What's cornean? - The glass bead was not detected. - P2,3,6,7 show pyrite (2.74 Å peak). This does not agree with the cube-feature in the radiography. (orientation problem?) - Al/Ag is not present. The peaks at 2.33, 2.44, 3.31 Å are unexplained. - Quartz in P5 is polycrystalline, while quartz in P1 is a single crystal. - It is surprising that this box is more transparent than H-VIII.

Chapter 4

Neutrons and the study of archaeological objects

The discovery of ancient artifacts and artwork usually raises a variety of questions such as the correct determination of their historical and cultural time-frame, the place and method of production, the choice of treatments and conditions for restoration and preservation. In the field of archaeometry, new perspectives are opened up by the use of neutron techniques. Neutron is a very suitable means for the collection of information from the bulk of large cultural heritage objects. In fact neutrons penetrate through objects without substantial attenuation, a property that makes them ideal for non-destructive testing. Information on the artifacts is relative to their composition, the presence of alteration, crusts, inclusions, the structure of the bulk, the typology of the location of materials extraction, the manufacturing techniques, refractoriness, the porosity, the firing temperature. The provenance and the state of conservation of ancient objects are of key importance to address matters of attribution and restoration of archaeological objects.

In this chapter results from the use of 'standard' techniques on real ar-

chaeological objects are reported. The samples come from important archaeological sites or museums such as *Museo Nazionale Etrusco di Villa Giulia* (Rome) or the *Parco archeologico di Villa Adriana* (*Tivoli*, Rome).

4.1   Metals

4.1.1   Etruscan bronzes

Neutron Diffraction (ND) study of laminated ancient bronze vases was performed. The bronze vases, preserved at the *Museo Nazionale Etrusco di Villa Giulia* (Rome, Italy), are part of an Etruscan collection discovered in the necropolises of *Osteria-Poggio Mengarelli* and *Cavalupo* in the outskirts of *Vulci* (*Viterbo*, Italy). The study allowed to derive information related to the main composition of the objects, possible presence of alterations and their nature and state of conservation. Moreover, the data analysis of corrosion products provides information about the past environments and the physical/chemical events that transformed the objects into a partially corroded matrix.

During the first millennium BC the large area of *Vulci* was site of an Etruscan community. The town development took place during the two centuries characterizing the *Villanoviano* period ($9^{th} - 8^{th}$ BC): the ancient villages slowly began to merge into rich and fortified towns. This was a time of large transformations and *Vulci* workshops had a fundamental role in the metallurgic activity of Southern *Etruria*. Vases were used to hold, pour or drink liquids; they were placed in the tombs to evoke the convivial ceremony held by the dominant elites. The samples, 14 fragments, were analyzed with regard to chemical-phase compositions and corrosion products. Bronze is composed of copper, tin ($Cu \equiv 85 - 95\%$, $Sn \equiv 5 - 15\%$) and small

quantities of other metals. The determination of the exact copper/tin/lead relative composition provides important information on the working process and technologies adopted. The presence of other components, like corrosion products, is linked to the past environment and to the physical and chemical events that transformed the object into a partially corroded matrix. Some bronzes also contain lead added to the mixture of copper and tin in order to lower the melting temperature during casting. The atoms arrangement in the bronze alloy can be seen as the incorporation of tin into the copper crystalline structure. This doesn't change the crystal structure but it expands the unit cell since tin atoms are bigger than copper ones. Evaluation of unit cell expansion provides indirectly information on the tin content and, therefore, the type of bronze. In low-tin bronzes (content of tin less than 17% by weight), typically used for casting, the lead concentrates in small globules throughout the metallic structure. These globules (typically $30 - 200$ μm in diameter) are randomly distributed. Neutron diffraction measurements were performed on INES powder diffractometer at ISIS Spallation Source (Rutherford Appleton Laboratory, UK). Each sample was placed in a vanadium pocket positioned inside an evacuated sample-chamber. The object was studied with a single sampling by using a beam size of (4×4) cm^2; in most cases the beam area covered the whole fragment being examined, thus allowing a reliable determination of the average composition. The spectra cover a slightly different d-spacing range with a diverse resolution: the first bank (at highest resolution) is in back-scattering and detects the pattern in the region between 0.1 Åand 1.6 Å. Indeed, this is the area with the highest density of peaks. The last bank, in forward scattering, covers the high-d region; here only few peaks are present but these are the most important for the identification of the phases. The data have been normalized to the number of counts (through the incident monitor) and have been divided by a vanadium rod spectrum in order to account for the detectors' efficiency.
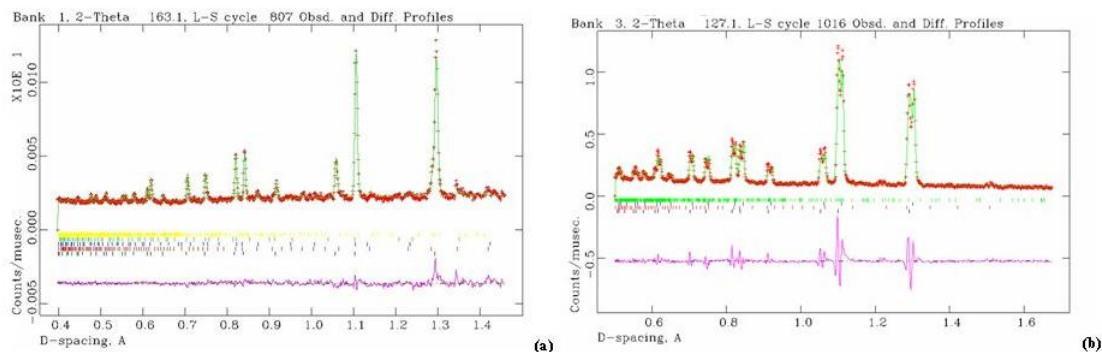
Figure 4.1: *Typical spectra are reported as normalized number of counts as a function of d-spacing. Best fit of data are also shown, with the peak position of the different components, and residue is reported in violet. (a) sample n.6, detector bank n.1 at $2\theta = 163$. Components: yellow=bronze (Cu/Sn), green=cuprite (Cu_2O), blue= lead, black=tenorite (CuO), red=nantokite (CuCl); (b) sample n.8, detector bank n.1 at $2\theta = 127.1$. Components: black = bronze1 (Cu/Sn), blue = bronze2 (Cu/Sn), red = cuprite (Cu_2O), green = covellite (CuS). It presents double bronze peaks, corresponding to different percentages of tin in the alloy: this sample is composed of two distinct parts, not coming from the same casting.*

Data for each sample have been fitted with the commercial GSAS software. The results of analysis are shown and compared in figure 4.2.

The results for the investigated samples show that 60% to 95% by weight is un-corroded alloy that presents a composition ($Cu = 90 \pm 4\%$) which is typical of low tin ancient bronzes. Recent studies [3], [37] have shown that the width of the peaks derived from Gaussian fits of the ND data, are related to thermal-mechanical treatments. The conclusions drawn in these papers, based on experiments performed on standard samples, relate the relative peak width $\Delta d/d$ trend and the different working treatments such as hammering, raw casting, annealing, different cooling dynamics. This

N	Bronze [wt%]	Lattice parameters [Å]	Cu; Sn [wt%] in bronze	Pb [wt%]	Cuprite [wt%]	Tenorite [wt%]	Azurite [wt%]	Covellite [wt%]	Botallackite [wt%]	Nantokite [wt%]
1	84.3	a=b=c=3.681	88.5; 11.5	3.7	12.0	-	-	-	-	-
2	75.6	a=b=c=3.676	89.4; 10.6	2.1	22.3	-	-	-	-	-
3	34.7	a=b=c=3.658	92.3; 7.7	-	60.0	-	5.3	-	-	-
4	80.1	a=b=c=3.678	89.1; 10.9	2.9	17.0	-	-	-	-	-
5	76.3	a=b=c=3.676	89.3; 10.7	0.8	8.1	-	-	14.8	-	-
6	75.2	a=b=c=3.666	91.0; 9.0	1.4	20.0	1.8	-	-	-	1.6
7	77.5	a=b=c=3.674	89.7; 10.3	1.9	18.8	1.8	-	-	-	-
8	70.0	a=b=c=3.657	92.6; 7.4	-	1.4	-	-	6.5	-	-
	22.1	a=b=c=3.689	87.2; 12.8							
9	-			8.9	91.1	-	-	-	-	-
10	-			5.9	49.0	8.9	-	31.4	4.8	-
11	60.9	a=b=c=3.673	89.8; 10.2	1.7	33.7	2.2	-	-	-	1.5
12	89.4	a=b=c=3.684	88.0; 12.0	0.3	10.3	-	-	-	-	-
13	74.5	a=b=c=3.663	91.6; 8.4	1.5	21.6	-	-	-	-	2.4
14	88.8	a=b=c=3.694	86.3; 13.7	1.1	10.1	-	-	-	-	-

Figure 4.2: *Results from ND analysis: weight percentage of present compounds.*

information, compared to the above mentioned diffraction results, was used to deduce the type of undergone treatment for the examined Etruscan samples.

In figure 4.3 the relative peak width $\Delta d/d$ has been reported as a function of d-spacing for all the samples. It seems that the working methods for the Etruscan bronzes were very similar between each other: annealing and two different types of cooling dynamics (fast and slow) are present while hammering could also be present.

Generally speaking, the atmospheric corrosion is an important degradation process which causes damage to equipment and structures. It has become evident that acid deposition through rain, snow, fog, or dew has resulted in a substantial deterioration of artistic and historical objects, including ancient buildings and structures of historic value, statues, monuments and other cultural heritage objects. The atmospheric corrosion of metals is an electrochemical process in which a metal reacts with its environment to form an oxide or other compounds. Metals exposed in the environment will absorb water forming a thin water layer on their surface. Several gases like
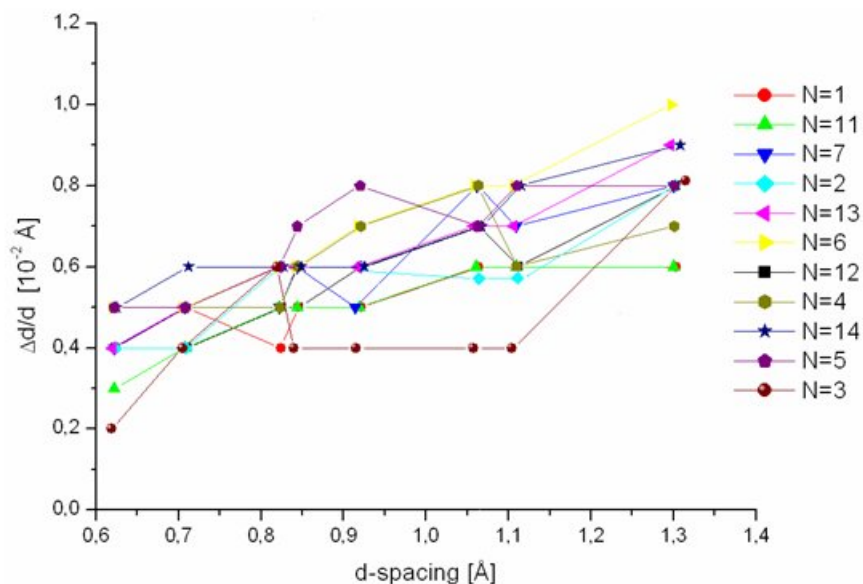
Figure 4.3: *Relative variation of the bronze-Bragg peak width for the different samples.*

oxygen (O_2) and pollutants - like sulphur dioxide (SO_2) and carbon dioxide (CO_2) - which are present in larger amounts in urban and industrial environments, accelerate the corrosion processes. CO_2 is a colourless gas with a sharp, irritating odour. SO_2 is an acidic gas and it is a major component of acid rain; because it mixes and oxidizes with the water vapor in the atmosphere to produce sulphuric acid (H_2SO_4), SO_2 influences strongly the local pH on the surface. This causes oxide dissolution and increases the corrosion rate. Additionally CO_2, mainly formed by the combustion of organic matter, has an important role in atmospheric corrosion due to the formation of secondary products, especially on non-ferrous metals. Normally, the concentration of CO_2 in the atmosphere is about 350 ppm. When dissolved in water CO_2 forms carbonic acid (H_2CO_3), a weak acid which can produce bicarbonates and carbonates, mostly insoluble. CO_2 concentration is one of

the most important parameters in determining corrosion processes in oil/gas production environments [38]. The recent Fourier Transform Infrared Spectroscopy (FTIR) studies on the effect of CO_2, SO_2 and $NaCl$ concentration on atmospheric corrosion of metals may help in understanding crevice corrosion, pitting corrosion and corrosion beneath organic coating. The mechanism by which CO_2 controls the corrosion of copper is well understood. It has been reported [39] that CO_2 has a strong effect on the $NaCl$ induced atmospheric corrosion of metals; the corrosion is considerably lower at low CO_2 concentrations ($[CO_2] < 1$ ppm) than at environment concentration ($[CO_2] \approx 350$ ppm). At $[CO_2] < 1$ ppm the $NaCl$ induced corrosion leads to the formation of corrosion products containing cuprite (Cu_2O), tenorite (CuO), botallackite ($Cu_2(OH)_3Cl$), copper(II) hydroxide ($Cu(OH)_2$), and carbonate $(CO3)^{2-}$. Another factor, which influences the corrosion process, is the effect of CO_2 and pH combined. At higher pH values ($[CO_2] < 1$ ppm) the formation of tenorite and cuprite is favoured. The presence of tenorite increases the corrosion resistance of the oxide layer and ultimately decreases the corrosion rate. In the same condition it is possible to have the formation of insoluble nantockite ($CuCl$), whereby more soluble chlorides have the tendency to trigger localized corrosion and to accelerate the initial atmospheric corrosion of copper. At $[CO_2]$ close to 350 ppm, the corrosion products after exposure include cuprite, malachite ($Cu_2(OH)_2CO_3$), carbonate but not tenorite. In these conditions CO_2 will increase the corrosion rate of samples exposed. It has been shown [39] that the oxidation of SO_2 in presence of humidity, leads to formation of sulphate $(SO_4)^{2-}$ and dithionate $(S_2O_6)^{2-}$ ions. A copper catalysed reaction for the sulphite oxidation was suggested; it includes the formation of a Cu(II)-sulfito complex as an important step. The corrosion products finally formed are nantockite, botallackite, sulphate, sulphides and small amounts of dithionate and carbonate.

However, the mechanism by which SO_2 accelerates the corrosion of cop-
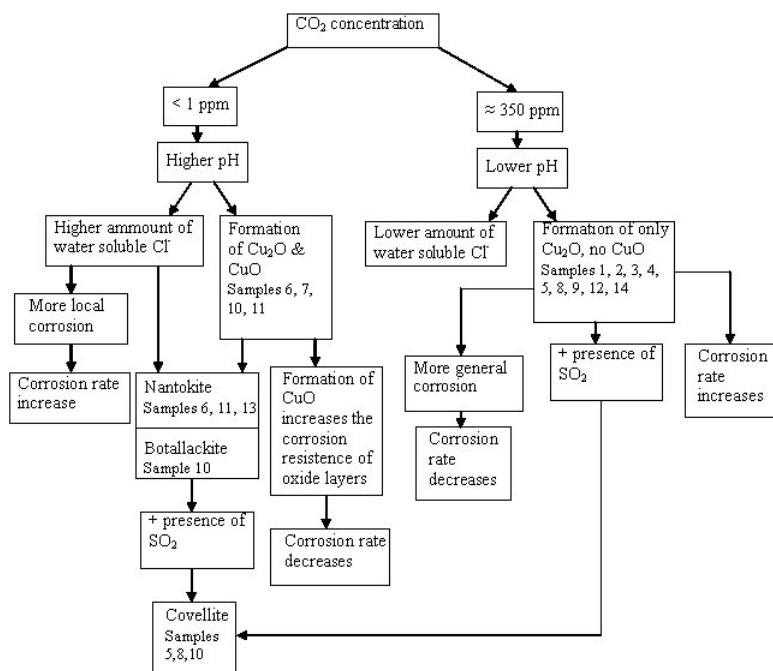
Figure 4.4: *Schematic draft of chemical phenomena on bronze surface.*

per is still not fully understood. In samples $1, 2, 3, 4, 5, 8, 9, 12$ and 14 the presence of cuprite may be justified at high level of $[CO_2]$. For example at $[CO_2] = 350$ ppm the main corrosion product after exposure in low pH conditions, is cuprite which will increase corrosion rate. Absence of chloride compounds is indicative of an essentially dry environment. In samples 5 and 8 the presence of SO_2, besides the formation of a Cu(II)-sulfito complex, promotes the formation of copper sulphides. A different situation is shown in samples $6, 7, 10$ and 11 where presence of tenorite implies $[CO_2] < 1$ ppm for the conservation environment. At such concentration the high pH value on the surface promoted the formation of both tenorite and cuprite. The resulting layer acted as a passive surface and contributed to a lower corrosion rate. The presence of nantokite in samples $6, 11$ and 13 as well as of botallackite

in sample 10 could be due to a higher amount of water soluble chlorides in the environment. The low quantity of chloride in comparison to other copper compounds shows that the corrosion rate decreases at low $[CO_2]$ ($<$ 1 ppm). Finally, in samples $5, 8$ and 10 the combination of SO_2 and CO_2 promotes the formation of sulphate, sulphite and sulphides (CuS in sample 10) and small amounts of dithionate and carbonate. The formation of covellite (CuS) may be due to combination of botallackite with SO_2, through presence of intermediate states (Cu-sulphates). The presence of covellite may be indicative of contact with salted water, as it has been proven [38],[39] that copper sulphide is a common corrosion product on objects buried in seawater sediments removed from oxygenated conditions. Covellite presence also suggests for burial conditions where reduction of sulphate by bacteria is possible. Sulphide ions are produced essentially by the reaction $2SO_4^{2-} \leftrightarrow S^0 + S^{2-} + 4O_2$. The bacteria utilize oxygen for oxidative enzymatic activity, and one of the end products in seawater or sediments is hydrogen sulphide ($2H^+ + S^{2-} \leftrightarrow H_2S$) which can form insoluble complexes with trace elements in oxygen-deficient sediments. Formation of hydrogen sulphide accelerates the corrosion of copper alloys by formation of covellite.

4.1.2 Montesarchio's bronze Spearhead

A Bronze Age Spear-head preserved from *Museo Archeologico Nazionale del Sannio Caudino - Montesarchio* (*Benevento*, Italy) and dated 8th century BC was investigated via neutron and X-ray radiographies. The aim of the study was to check the state of conservation of the object with the final intent to supply information useful to select the best preservation and restoration method and the exposition conditions of all metal objects in Montersarchio's Museum. The surface, indeed, of the sample appears, by eye, pitted by green areas, possibly CuO corrosion and covered by a darker patina.

The object is part of the furniture of a burial grave dating to the half of

Figure 4.5: *Photograph of the Montesarchio's spearhead - length = 30.5 cm handle's diameter = 3.0 cm.*

the 8th century BC. This grave has great significance in the Montesarchio's necropolis: it is, indeed, one of the two tombs belonging to the early iron age in a contest of about 3000 excavated.

Iron and bronze weapons are generally produced locally. However, the *Caudium* peculiar topographic position, to connect Tyrrhenian coast with the inner Campanian areas, helped along trade contacts between the city and the coastal South Italian and Etrurian centers until 4th century BC. The object was polished and consolidated by a protective transparent-paint layer. The radiographic measurements were performed at the ANTARES facility at the FRM-II reactor from the Technical University Munich, Garching, Germany. This facility is situated at beam line $SR4b$, facing the cold source with neutron fluxes of $1 \cdot 10^8$ $n/cm^2 s$ and $2.6 \cdot 10^7$ $n/cm^2 s$. The typical energy of cold neutrons is 3 meV. The standard detection system is a 2048×2048 pixel cooled CCD camera. It is used in combination with a mirror, a neutron or a X-ray scintillation screen, (figure 4.7) and a sample movement system, to perform neutron radiography or neutron computed tomography.

The setup of the ANTARES facility is shown in Figure 4.6.

A 320 KeV X-ray tube can be shifted into the beam path when the neutron shutter is closed. The tube is mounted at the beginning of the flight tube and produces exactly the same beam geometry as the neutron collimator. Images recorded with the X-ray tube and scintillator can be immediately overlaid to neutron images without further adjustment.
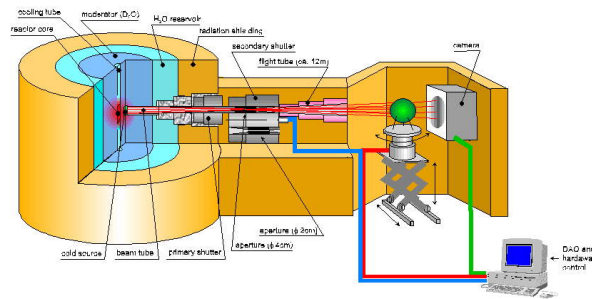
Figure 4.6: *ANTARES set-up, FRMII reactor neutron source, Garching, Germany.*
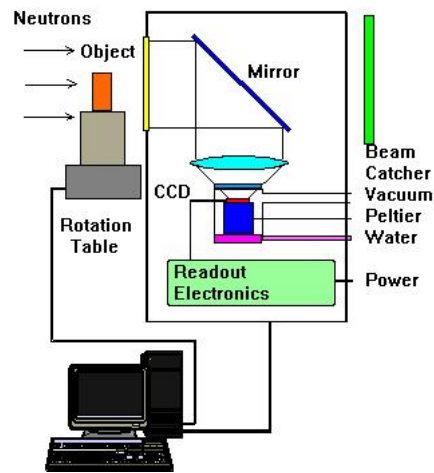
Figure 4.7: *ANTARES detector system set-up.*

In order to obtain an estimate for the irradiation time of the object, it was performed a short 30 seconds irradiation on the ANTARES beam line. The object it was initially irradiated with the full open beam configuration and the gammas-spectrum, after 1 day from the exposure, was measured in order to define the elements inside and make a prediction about the decay-time, after longer irradiation, of the sample. The beam flux was 108 n/scm^2.

The gamma spectrum allows the presence of copper and tin as majority
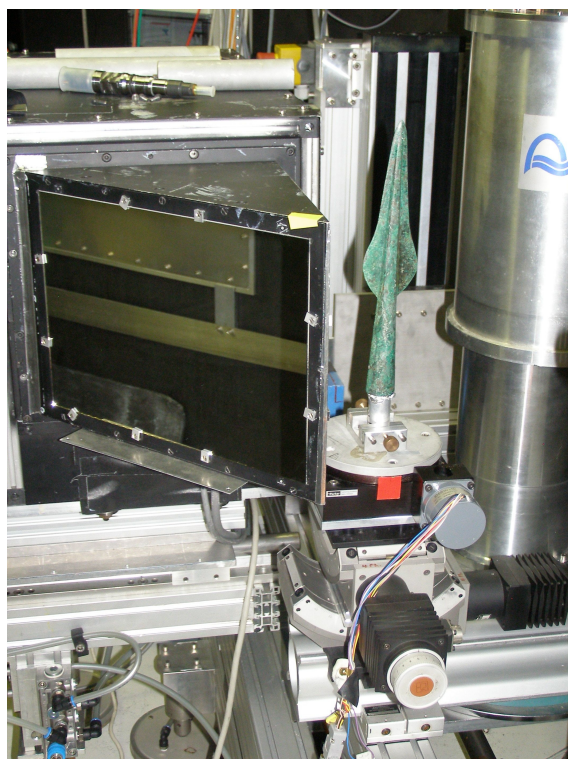
Figure 4.8: *Photograph of the Montesarchio's spearhead setup on ANTARES instrument (FRMII)- length $= 30.5$ cm handle's diameter $= 3.0$ cm.*

elements and elements like arsenic (^{76}As) and antimony (^{122}Sb) as minority elements. With these informations it was possible to define the irradiation limit of the object, in relation with the sample-permission of stay at the reactor (5 days). It was 20 minutes. Radiographies were performed rotating the sample with respect to the incoming beam at 0^0, 30^0, 60^0 and 85^0.
In all positions different filter types were applied: no filter, a poly-crystalline Bismuth filter to remove gamma radiation, a polycrystalline Beryllium filter to remove the thermal neutrons or a sapphire filter to remove the fast neutrons from the spectrum. Finally X-rays radiographies by 320 KeV X-ray

tube were performed. Results are shown in figures from 4.9 to 4.12.
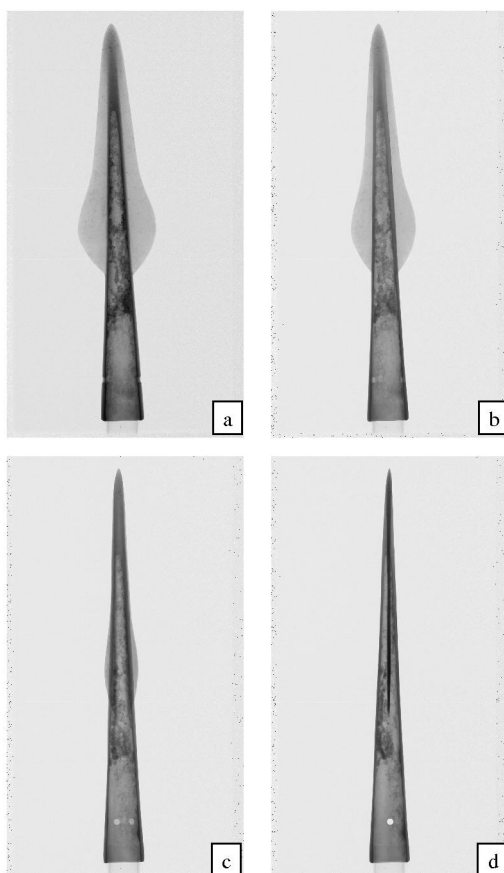
Figure 4.9: *Open beam neutron radiographs at 0^0, 30^0, 60^0 and 85^0 of rotation toward the incoming beam - length = 30.5 cm handle's diameter = 3.0 cm.*

The neutron images give more detailed information about the copper object. The neutron and the X-rays radiographies show that the metal of the spread-head is mostly intact. Density changes as shown in the false colour radiographies and indicate thickness variation that could be given by the presence of non-homogeneous copper compounds on the surface.
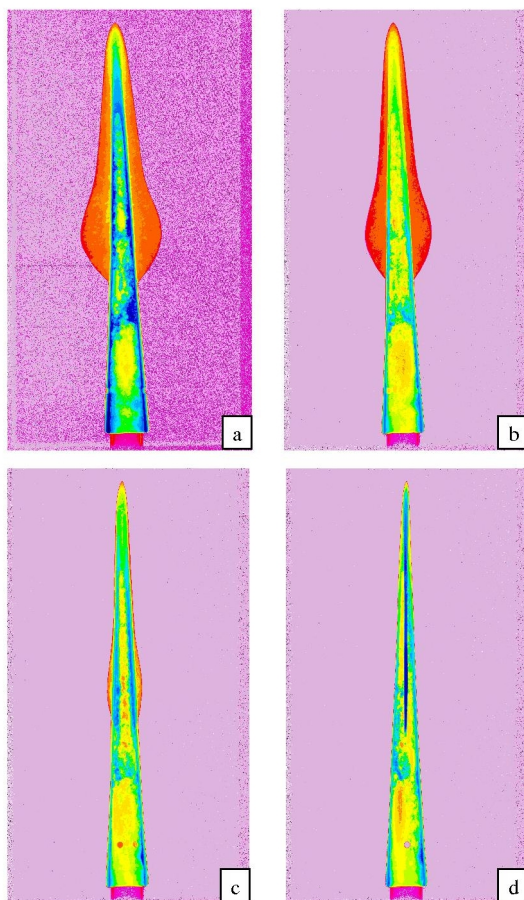
Figure 4.10: *Open beam false color neutron radiographs at 0^0, 30^0, 60^0 and 85^0 of rotation toward the incoming beam - length $= 30.5$ cm handle's diameter $= 3.0$ cm.*

Finally, the object is in a good state of conservation.
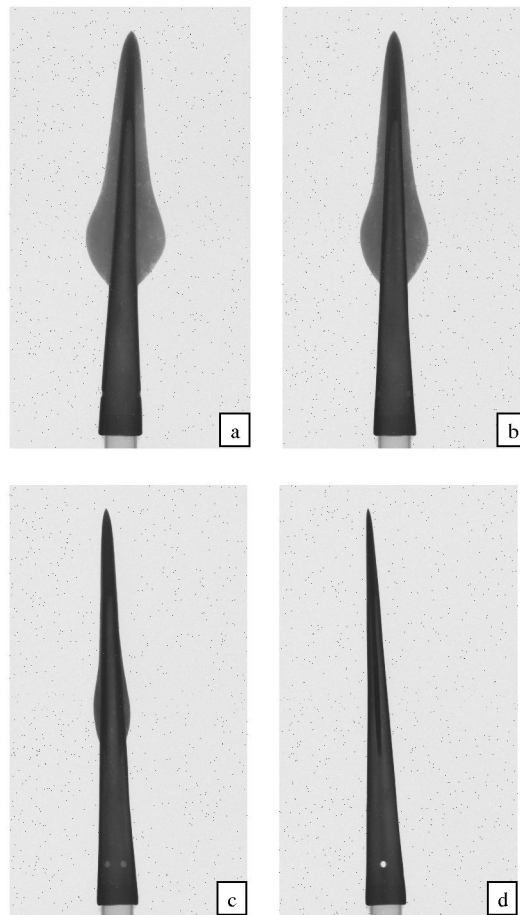
Figure 4.11: *Open beam X-ray radiographs at 0^0, 30^0, 60^0 and 85^0 of rotation toward the incoming X-ray beam - length = 30.5 cm handle's diameter = 3.0 cm.*
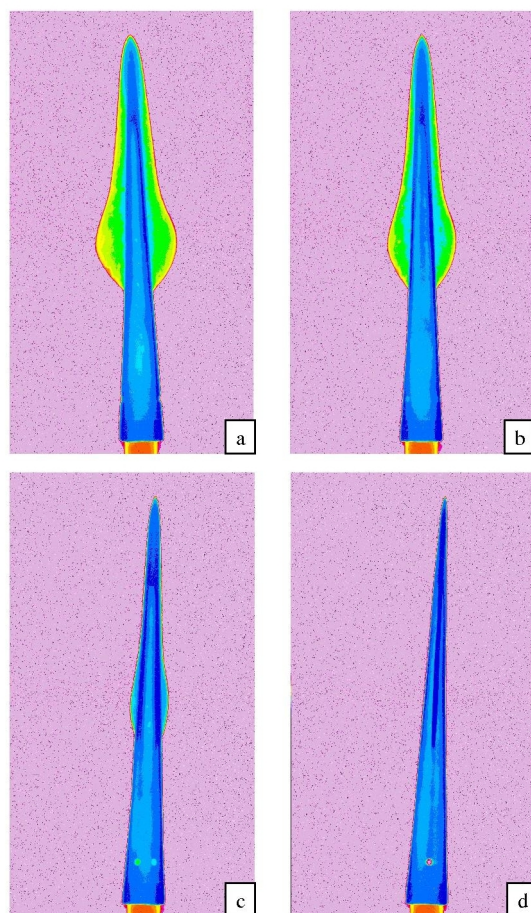
Figure 4.12: *Open beam X-ray radiographs (false colours) at 0^0, 30^0, 60^0 and 85^0 of rotation toward the incoming X-ray beam - length $= 30.5$ cm handle's diameter $= 3.0$ cm.*

4.1.3 Roman coins

Two ancient roman coins of the 2th century BC were studied by neutron diffraction. The archaeological interest about these samples was to discover the composition of the coins.

Figure 4.13: *Photograph of Coin 1.*

Figure 4.14: *Photograph of Coin 2.*

The period in which silver coins where introduced in Roman era is not exactly known but it is reasonably dated in the period of the Punic Wars (first: $264 - 241$ BC and second: $218 - 202$ BC), series of three wars fought between Rome and Carthage. In that period a big amount of money became necessary to cover war-expenditures. During this century a very large number of 'fakes' coins were used. It is not clear if they were made by the Roman

Republic or they are forger work. This phenomenon regards, in particular, silver coins. The 'authentic' and the 'fakes' coins can be tell apart by eye because the 'fakes' have a core by copper or lead and an external layer made in silver. Both samples are republican-roman money delivered by Roma's mint.

Neutron diffraction measurements on INES diffractometer at ISIS neutron spallation source (UK), were performed with the aim to authenticate the objects.
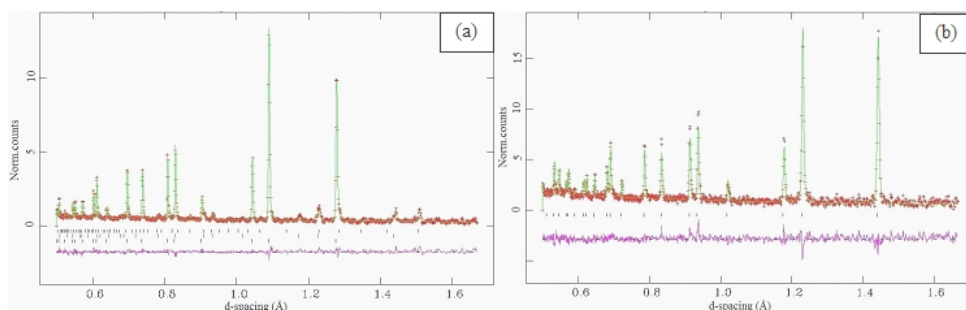
Figure 4.15: *Spectra are reported as a function of d-spacing. Analysis phase contents of coins: (a) Coin 1 composition: black-copper (Cu): 79.247%, red-Silver: 18.329%, blue-Cuprite: 2.424%. (b) Coin 2 composition: 100% Silver (Ag).*

The analysis of the diffraction measurements on the two ancient coins show the difference in composition: one of these is composed by only silver and it can be hold as 'authentic', instead the second one is composed by a nucleus of copper with a cuprite patina and a silver covering. The latter is clearly 'fake'.

Sample	Composition	Percentage
Coin 1	Ag	100%
Coin 2	Cu or (Cu alloy)	79.247%
	Ag	18.329%
	Cu_2O	2.424%

Table 4.1: *Diffraction results on the two samples at INES powder diffractometer (ISIS, UK).*

4.2   Ceramics

4.2.1   Southern Italy ceramics

Ceramic is known as one of most common material found in archaeological excavations. It is made from common materials and his production, although technology made refinements, is generally simple. This material is constituted of a vitreous phase that act as cement to link more crystalline phases. These phases are present in micro-grains that could be have different dimensions and their distribution depends from raw materials and from firing conditions. The row materials are clay, water and fillers. Clay is a sedimentary rock composed by minerals like silicate rock (silicium, aluminium e oxigen, calcium, magnesium, sodium, potassium, iron, manganese and titanium); the principal minerals are the illite, the montmorillonite and the kaolinite. The fillers are materials with various function such organic like dung, straw and hay or inorganic likes shells, sand calcite and sandstone. These are added to the ceramic dough to permit the evaporation of water contained in the amalgam, minimizing the contraction of the clay during firing and helping the vitrification process. Thermal processes of the ceramic dough produce a series of physical and chemical irreversible transformations that get new compounds in solid and fluid phase. Physical important parameters for the ceramic formation are the thermal gradient, the maximum value of baking temperature, the time of treatment and the atmosphere conditions of the furnace (for the redox-reactions).

The application of neutron-diffraction technique allowed us to carry out detailed analysis of the mineral phase composition and structural properties in a non-destructive way, so intact large fragments were investigated without damaging the objects. This information can be used to trace the provenance of the artifacts or provide indication about the manufacturing methods.

Recent findings in Southern Italy (1988, Brindisi, Italy) provided a large number of potteries coming from different regions of central Mediterranean area (Greece, in particular) and eastern regions (Syria, Palestine, Asia Minor) dated $2^{th} - 3^{th}$ century AD. Beside traditional techniques like neutron activation and X-ray fluorescence (XRF), non-destructive neutron diffraction technique can be used to obtain bulk information, without sectioning and damaging. Samples were investigated with neutron diffraction technique by INES spectrometer. More experiments, indeed, have shown the ability of neutron diffraction to provide reliable information from large ceramic fragments or even a whole ceramic object [40], [41].

Measurements provided data collection from bulk and surface of the samples and give the opportunity to determine, quantitatively, the crystalline compounds of the clays and their proportions in the sample. The investigated objects are three representative fragments (figures 4.16, 4.17, 4.18) of $1 - 3^{th}$ century AC coming from the same excavation site but seems to have different manufacture provenance. Diffraction patterns were analysed by Rietveld refinement method using the GSAS program [13]. Results are shown in table 4.2.

Figure 4.16: *Photograph of sample* 1. *Asia Minor cup ceramic.*

During the clay-baking, some physical transformations happening: the first is the expansion as consequence of the heating. Water present in the

Figure 4.17: *Photograph of sample 2. Corinthian matrix decorate ceramic.*

Figure 4.18: *Photograph of sample 3. Ceramic dish probably of greek or Patrasso production.*

dough, moreover, evaporates between $100 - 200$ ^oC. At right temperature $(400 - 650$ $^oC)$ the evaporation of the lattice water in the oxydril groups takes place and, increasing temperature, fusion processes happens.

When the system cooling-down, begins the formation of crystalline compounds or vitreous phase that depends from the compounds type and the cooling conditions. Moreover there are many chemical reactions that transform the dough in minerals of new-formation that take place at different temperatures. Also the atmosphere conditions of the furnace play an important rule in the reactions. The iron hydroxide as the goethite $(\alpha - FeOOH)$ at low temperature give the reaction $2FeOOH \rightarrow Fe_2O_3 + H_2O$ with consequent formation of the hematite that confer the classical red-brown coloring. The
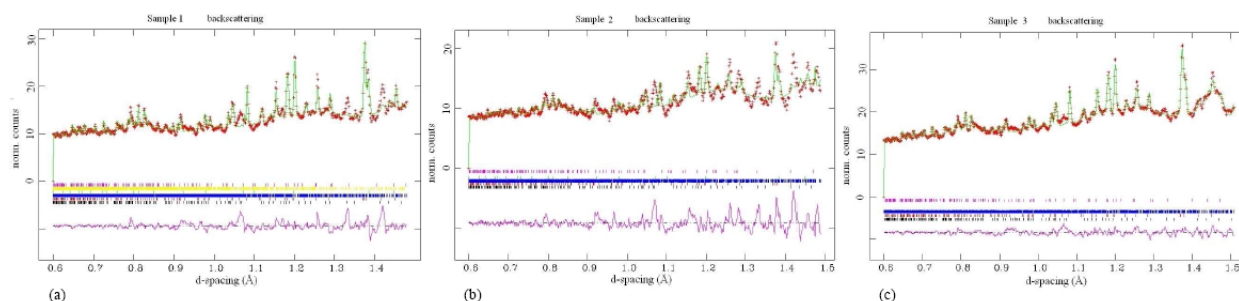
Figure 4.19: *Spectra are reported as a function of d-spacing. Analysis phase contents of potteries: (a) Sample 1 composition: calcite: 2.9%, quartz: 61.0%, plagioclase: 25.5%, lime: 7.4%, muscovite/illite: 2.0%, hematite: 1.2%. (b) Sample 2 composition: calcite: 5.2%, quartz: 50.8%, plagioclase: 31.4%, lime: 7.2%, hematite: 5.4%. (c) Sample 3 composition: calcite: 3.0%, quartz: 68.4%, plagioclase: 27.6%, hematite: 1.0%.*

Sample	Age	Site	CA	QU	PL	LI	MI	HE
1	1th - 2th cent. AC	Asia Minor	2.9	61.0	25.5	7.4	2.0	1.2
2	2° half 2th - 3th cent. AC	Corinth	5.2	50.8	31.4	7.2	−	5.4
3	1th - 2th cent. AC (?)	Greece or Patrasso(?)	3.0	68.4	27.6	−	−	1.0

Table 4.2: *Diffraction results on the three samples at INES powder diffractometer (ISIS, UK). Composition of the samples in weight percentage wt % where: CA=calcite, QU=quartz, PL=plagioclase, LI=lime, MI=muscovite/illite, HE=hematite*

hematite is formed also at higher temperature ($\approx 750\ ^oC$) after the expulsion of Fe(III) from the phyllosilicate lattice. The decomposition of carbonate

(calcite - $CaCO_3$) occurs in a large temperature range $(650-900\ ^oC)$ and this reaction gives the formation of Lime (CaO) through: $CaCO_3 \rightarrow CaO + CO_2$. The decomposition temperature depends from the grains-dimension, the crystallinity degree and the carbonate abundance. Calcareous clay can produce carbonate up to $950\ ^oC$ depending on the abundance and the low kinetics of that reaction [42], [43].

In the studied case, the comparison of the three different samples was performed. It is clearly visible, in all spectra, typical modulated background coming from the scattering of the amorphous material as silica glass. The sample 1 has difference from sample 3 due to the presence of additional components in sample 1 (lime and muscovite/illite). These samples exhibit, indeed, a very similar mineral ratio of plagioclase, hematite and calcite related to the content of quartz, while the sample 2 is completely different. The presence of some compounds such as quartz, calcite, plagioclase and illite could be related to the raw materials extraction site while the quantitative differences could be assumed in different geological levels. Looking at the table 4.3 that reported ratio of much more representative compounds (calcite, quartz, plagioclase, hematite) it could be formulated the hypothesis that all the samples have been baked at temperature in the range of $750-900^oC$.

Sample	PL/QU	HE/QU	CA/QU
1	0.418	0.019	0.048
2	0.618	0.106	0.102
3	0.403	0.015	0.044

Table 4.3: *Ratio of weight percentage (wt %) fractions where: CA=calcite, QU=quartz, PL=plagioclase, HE=hematite*

4.3 Stones

4.3.1 Roman Empire Marbles

A recent preliminary application of neutron techniques in the cultural heritage field is a neutron diffraction study of marbles from Villa Adriana in Tivoli (Rome) [44], [45]. Villa Adriana is an exceptional complex of classical buildings designed and erected in the 2nd century AD by the Roman emperor Hadrian, and is recorded by the UNESCO in the World Heritage List. Analytical investigations on monumental complexes of the Roman Empire age complement the studies carried out on architectural and building engineering in order to achieve unitary views on this historical period. In this context, neutron diffraction technique have been used for the characterization of ancient Roman marble fragments from the *Edificio con Tre Esedre* palace, located in Villa Adriana. The marble decorations were built with technique known as opus sectile, typical of Hadrian's time, with wall decorations belonging to the 2nd century AD. A reconstruction of the Palace's marble wall decoration positioning is shown in Figure 4.21.

Fragments of such decorations are used as samples. Marble is one of the most common stones used for monuments, statues and other objects of archaeological interest and is typically composed of either calcite or dolomite or a combination of the two. The ongoing study aims at distinguishing different marble types on the basis of the mineral phase compositions and the crystallographic textures. Information obtained can be used to distinguish different types. The Diffraction experiments on marbles were performed on the Time-Of-Flight (TOF) diffractometers GEM, INES and ROTAX located at ISIS Neutron Spallation sources (UK). Multi-phase and multi-bank analysis of the diffraction patterns were carried out with standard crystallographic public-domain software (GSAS for quantitative phase analysis and MAUD for texture analysis). The texture information is displayed in Pole-Figures.

Figure 4.20: *View of Villa Adriana site, Tivoli, Rome, Italy.*

Pole Figures are the maps of the crystal grains orientations, caused in marbles by geological processes, and can be used as a fingerprint to identify them.

ND results on marbles are shown in table 4.4 that present the weight-percentage of each compound in a certain sample. Most of the samples, appear to be essentially carbonatic monophasic studied objects. Other phases, when present, are usually in small amounts.

Experimental data for marble VA2 and VA19, together with the final GSAS Rietveld refinement, are shown in Figure 4.22 and 4.23.

Table 4.5 reported the composition-scan derived by means of ND is indicated for different positions of the beam. This sample have big dimensions $(60 \times 50 \times 5)$ cm^3 and present of veins of different colours.

Figure 4.21: *Reconstruction of the marble wall decoration of the Palace Edificio con Tre Esedre.*

Figure 4.22: *Spectra from V A2 sample is reported as normalized number of counts as a function of d-spacing. Best fit of data are also shown, with the peak position of the different components, and residue is reported in violet. Component: calcite (CaCO₃).*

Actually measurements were performed with beam dimensions (5×5)

Sample	CA	QU	MC	PL	OR	MI	HO	HE	DO
$VA2$	100.0	–	–	–	–	–	–	–	–
$VA4$	15.8	3.3	–	–	–	80.9	–	–	–
$VA5$	–	–	–	–	–	–	–	–	100.0
$VA8$	100.0	–	–	–	–	–	–	–	–
$VA9$	100.0	–	–	–	–	–	–	–	–
$VA10$	–	3.4	8.1	44.2	34.2	–	7.8	2.3	–
$VA12$	93.4	–	–	6.6	–	–	–	–	–
$VA14$	–	1.5	–	83.0	15.5	–	–	–	–
$VA15$	96.9	0.1	–	3.0	–	–	–	–	–
$VA17$	97.9	2.1	–	–	–	–	–	–	–
$VA19$	57.2	4.3	–	–	–	38.5	–	–	–

Table 4.4: *Sample compositions based on ND measurements. Components: CA=calcite , QU=quartz, MC=mica, PL=plagioclase, OR=orthoclase, MI=muscovite/illite, HO=hornblende, HE=hematite, DO=dolomite*

mm^2. The anomalous value of composition found with the sample moved 5 mm is due in part to the presence of a vein.

Texture measurements were performed on GEM. GEM is equipped with 6 detector banks that have a coverage of 4 sterads and can 'see' the sample from different point of view. In this way the sample does not need to be rotate and the time of measurements are considerably reduced. Texture is the preferred orientation of crystallites is intrinsic in rocks and influence their physical properties. Pole figures produced from (006), (110) of a pure calcite sample ($VA8$) and pure dolomite sample ($VA5$) are shown in figures 4.25.

Both compounds have a trigonal crystal structure. The (006) pole figure
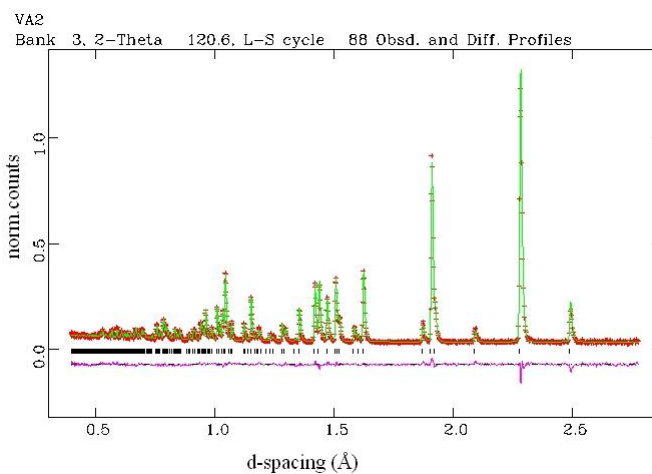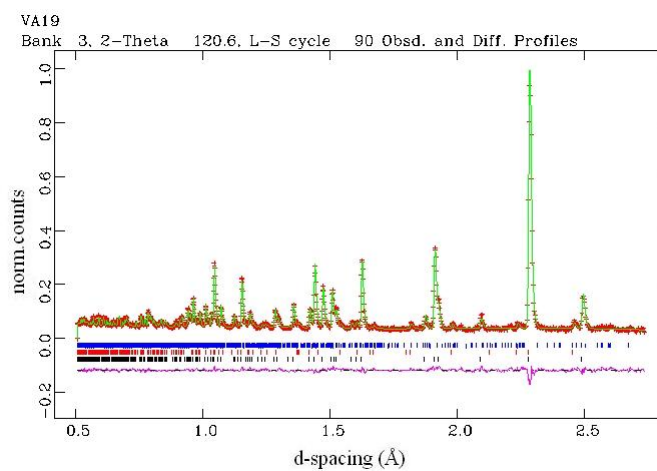
Figure 4.23: *Spectra from VA19 sample is reported as normalized number of counts as a function of d-spacing. Best fit of data are also shown, with the peak position of the different components, and residue is reported in violet. Components: calcite ($CaCO_3$), quartz (SiO_2) and muscovite ($KAl_2(AlSi_3)O_{10}(OH)_2$) /illite $K_yAl_{4()}(Si_{8-y}, Al_y)O_{20}(OH)_4$.*

Figure 4.24: *Photograph of VA9 sample.*
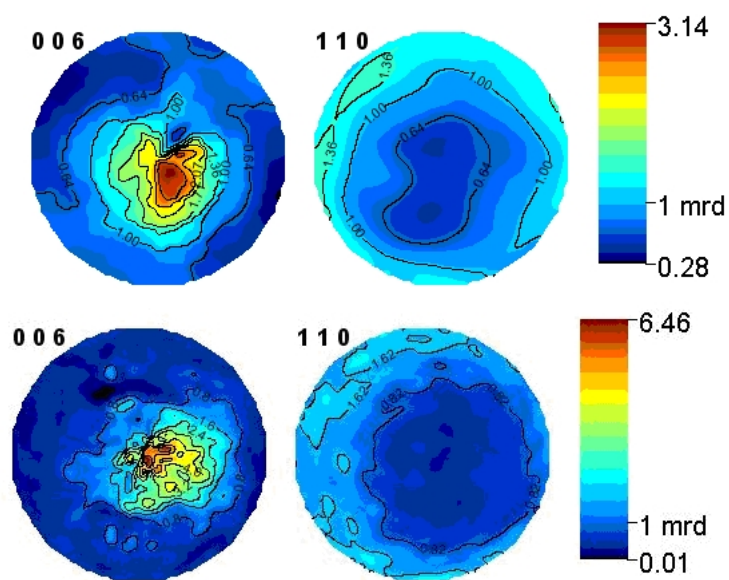
Figure 4.25: *Pole Figures. (top) Sample VA8 composed of only calcite, (below) Sample VA5 composed of only dolomite.*

Sample	CA	QU
0 mm	100.0	–
5 mm	97.2	2.8
15 mm	100.0	–
25 mm	100.0	–
35 mm	100.0	–
$45mm$	100.0	–

Table 4.5: *Local composition by a ND scan of VA as observed. Compounds: CA=calcite, QU=quartz*

represents the c-axis distribution while the (110) is representative of the a-axis distribution. Both samples exhibit a strong pole density maxima in the (006) pole figure, the texture type is typical of marbles. The texture of $VA8$ is quite typical for natural calcites that have suffered 'pure shear' or 'simple shear' deformations [16]. Pure shear occurs when the geological forces press the material in only one direction while 'simple shear' is a compression and a viscous translation.

Chapter 5

Preliminary results from newly developed techniques

This chapter presents preliminary results about measurements with integrated techniques: new Prompt Gamma Activation Imaging (PGAI) combined with Neutron Radiography (NR). Samples were two precious gilded bronze heads from the monumental doors of the *Battistero di Firenze* by *Lorenzo Ghiberti*.

5.1 The *Ghiberti* doors and preservation problems

The object of this study are two gilded bronze heads, part of the East and North monumental doors of *Battistero di Firenze*.

The gilded bronze doors of the Baptistery are one of most important masterpiece of the Italian metallurgical art of the XIV and XV centuries [46]. The critical aspect regarding its state of conservation is the chemical and physical stability of the gold layer on the bronze surface. The doors have

Figure 5.1: *(a) Head* 1*, from the 'Porta del Paradiso - Gate of Paradise' (b) Head* 2 *from the North door.*

suffered the consequences of events that have damaged the precarious status of the gilding such as the 1966 Florence flood, previous restoration treatments and urban pollution. The advanced deterioration state of the amalgam gilding sculptures lead to urgent preservation strategies beginning with cleaning treatments. The *Opificio delle Pietre Dure* (OPD) started a systematic investigation about the manufacturing techniques and state of conservation of the doors and in particular of the gilding to choose the best restoration practices at the beginning of the 1980s [47], [48], [49], [50]. Through these initial investigations the gilding technique (by mercury-amalgam) was found together with the stratigraphic structure of the objects: the bronze core is covered by copper corrosion compounds (such as copper oxides, chlorides and sulphates) and the gold is supported on this layer. The gilding is also covered by deposits and encrustations (gypsum, quarts, feldspars, carbon, etc.) which are caused by pollution. The copper corrosion phenomena grow below the gilding produced excrescences, pitting and in some cases micro-lifting and consequent loss of the gold layer. The oxide and salts layer constitutes the current bed of the gold which is in a precarious state. For this unstable

condition the cleaning operation was particularly difficult [48]. Moreover, it was necessary to remove selectively only the dangerous deteriorative and instable compounds and the encrustations while preserving the substrate of copper oxides that support the gold layer.

As of today, two types of cleaning methods were chosen and used to polish the East door known as 'Porta del Paradiso - Gate of Paradise': by chemical agent bath (Rochelle salt solution - sodium potassium tartrate) and by laser [51], [52], [53], [47].

In this context, it was decided to perform non-invasive neutron analysis on two elements coming from the *Ghiberti* doors.

The first sample, Head 1, is part of the gilded bronze decorations of the 'Gate of Paradise'. This door is under restoration, since twenty years, by the *Laboratorio di Restauro - Bronzi ed Armi Antiche*, and is in final state (due to be finished by May 2009). The second sample, Head 2, comes from the North Door which is not yet restored.

The aim of the present analysis was to:

- Head 1: Verify and compare the effects of the two cleaning methods adopted for the 'Porta del Paradiso - Gate of Paradise'. For this reason the head was treated in different ways: a portion of it was polished through chemical bath, the other through laser cleaning and the third remained uncleaned for comparison (figure 5.2).

- Head 1: Discover further details about the manufacturing technology of this piece in particular. The rear part presents an irregularity that seems a re-melting probably made as a correction of a first imperfect melting.

- Head 2: Verify the conservation state in view of a future restoration of the North Door.

Figure 5.2: *Head 1 cleaned with Rochelle salts and laser.*

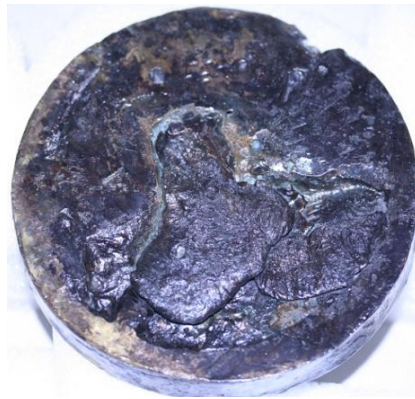**Figure 5.3:** *Back side of the Head 1 where is visible the presumable re-melting.*

These measurements will add to the previous extensive studies performed on the 'Gate of Paradise' with the intent to indicate the optimal micro-climatic conditions for future conservation and exhibition environments which will have to guarantee their preservation during time.

Prompt Gamma Activation Imaging (PGAI) combined with Neutron Ra-

diography (NR) measurements and high resolution radiographies at FRMII reactor (Garching, Munich) were performed and are described below; ND and NRCI/NRT measurements at ISIS neutron spallation source (Oxfordshire, UK) are planned for March/April 2009.

5.2 Transportation procedure

The performed neutron measurements, used instruments located in large scale facilities such as ISIS (UK), FRMII (D) and BNC (HU). This means that archaeological and cultural heritage samples needed to be transported and kept in safely during the process. The time of permanence, moreover, is a factor to consider and is related with the decay-time of the objects. After the identification of suitable, scientifically and archaeologically interesting objects, the activation after irradiation was estimated so as to have an idea about the cooling-down time for the investigated objects. This aspect is closely related to transport procedures because it is necessary to know the time of stocking at the facilities after irradiation. This aspect was kept in mind during the planning of the experiments.

Some 'best practices', regarding the transportation of Italian objects, were defined through the combination of practical and legal actions necessary when cultural heritage artifacts are brought abroad and subject to neutron experiments. They can be summarized in the following steps:

1. Permission from the owner entity

2. Assent of the own *Soprintendenza*

3. Permission from the MIBAC (Cultural Heritage Ministry)

4. Covering insurance permission

5. Temporary circulation certificate for transportation

6. Packaging of the samples by authorized and qualified personnel

7. Transportation of the samples via road or flight

8. Transportation of the samples back via road or flight and return to owner

The procedure was tested transporting the two precious gilded bronze heads property of the *Opera di S. Maria del Fiore* Museum, in Florence. The complete procedure took 4 months.

5.3 Sample holders

Two ad hoc Ergal sample holders were created for the two heads with the aim of preserving the object during measurements and functioning as interface between the objects and the instruments. The aluminum alloy (Ergal) contains only 0.01% manganese (Mn), which reduces the cooling-down time of the sample holder to a minimum. Aluminum is also a soft material and creates no damage to the objects. To make the sample holder softer, while still keeping the objects firmly in the sample holders, Teflon and plastic screws were used for the contact surface area between the sample holder and the object.
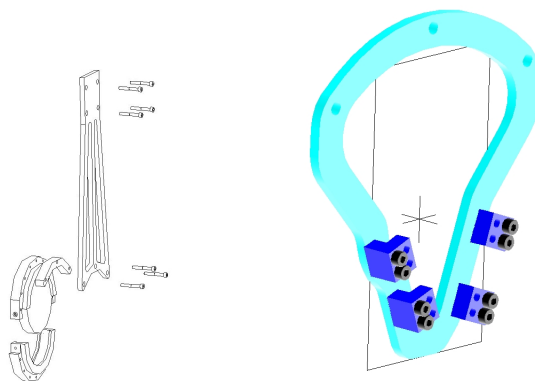

Figure 5.4: *Drawing of for gilded bronze Ghiberti Heads supports: Head 1 (left), Head 2 (right).*

5.4   Measurements and preliminary results

Two types of neutron investigations were performed at FRMII reactor source: punctual investigations (Prompt Gamma Investigation Imaging/Neutron Radiography - PGAI/NR) at PGAA station and Neutron Radiography at ANTARES station. Prompt Gamma Activation Imaging is a new technique that combines two standard techniques: Prompt Gamma Activation Analysis, which enables discovery of the elements present in the irradiated volume, and Neutron Radiographies, which determines the internal morphology of the sample. With the simultaneous use of these two techniques it is possible to know the elements of the sample and their spatial distribution thus allowing an elemental mapping.

The activation of the samples was permanently monitored. Before neutron measurements, Head 1 was scanned with the Scanny $3D$ laser that produces a $3D$ model of the surface. It was very useful to estimate the amount of gold before irradiating the samples, because it was possible to estimate their activation degree.

PGAI/NT measurements were performed in the three clean sectors of the Head 1 and on the Head 2 in a totally non-destructive manner. Neutron radiographies were used to define the real position of the beam and to identify the area illuminated by neutrons. Because we were interested in the elements presence around the gilding layer, the neutron beam was positioned so as to hit areas around few millimeters deep in the surface of the samples. The study of these layers allowed the reconstruction of their composition in a completely non invasive manner and down to a depth which is not reachable by other analytical techniques.

The PGAI/NT set up has been described in chapter 2 and is presented in figure 5.5.

Preliminary results of spots PGAI measurements are shown in table 5.1.

The presence of the Cl, detected by PGAI, in the un-cleaned zone is

Figure 5.5: *PGAI (Prompt gamma activation imaging) setup.*

Sample	Cleaning treatment	Elements
Head 1	Laser	Au, Cl, Cu, Hg,
Head 1	Rochelle salts	Au, Cu, Hg
Head 1	Uncleaned	Au, Cl, Cu, Hg
Head 2	Uncleaned	Au, Cl, Cu, Hg, K

Table 5.1: *PGAI/NT measurements results at PGAA station (FRMII, Garching, Munich).*

not surprising but its presence in the laser cleaning zone is an important information. In fact, Cl compounds are dangerous for the gilding in long run because of forms pitting and excrescences that damage the over-top gold layer.

Radiographies, made at the ANTARES station revealed new details about

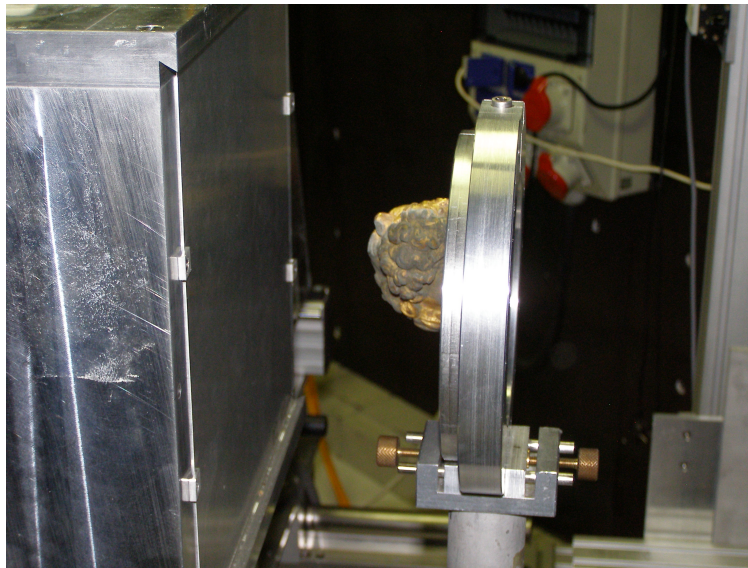the internal structure of the heads in particular about Head 1.

Figure 5.6: *ANTARES setup.*

Each radiography was performed using a beam with size $85 \times 85\ mm^2$ and an exposure time of 50 s.

Open beam false color neutron radiographies are presented in figure 5.9.

In the rear part of Head 1 un-homogeneities are visible which can be explained as a second melting made after the original ones. In all other heads, except two, an open cavity on the back is present. Through neutron radiographies the extension of the re-melting was determined: it seems to arrive in depth up to the face. A preliminary analysis of the radiographies showed that the re-melting is mainly in the front part corresponding to the area of the face and beard. An hypothesis is that the original melting was faulty and that the sculptor made another one. Draining the new metal inside the original cavity, the head orientation directed the casting in the front part of the head leaving part of the original cavity empty in correspondence of
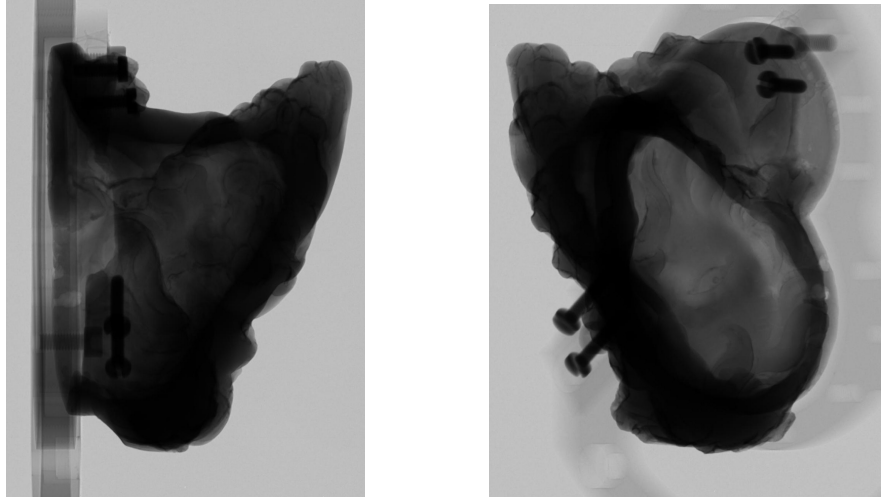
Figure 5.7: *Neutron radiographies of the Head 2.*

the neck.

After PGAI and NR measurements the decay spectra were measured after one day from the last measurements obtaining the results reported in table 5.2.

Sample	Instrument	Nuclide
Head 1	PGAA	^{56}Mn, ^{76}As, ^{122}Sb, ^{198}Au
Head 1	Antares	^{65}Zn, ^{76}As, ^{122}Sb, ^{198}Au
Head 2	Antares	^{65}Zn, ^{76}As, ^{122}Sb, ^{124}Sb, ^{198}Au

Table 5.2: *Nuclide identification by decay spectrum after irradiation at PGAA and Antares station.*

New neutron experiments are planned on the two Heads. The aim on the next measurements is to characterize, non-destructively, the bulk phase composition and the strain distribution in small gauge volume at critical

locations of the two heads characterising phase composition, chemical inhomogeneities, strains, providing an insight into master processes and help to set up restoration treatments. The results of this new investigation will help the conservators from *Opificio Pietre Dure* to set up the future restoration treatment.
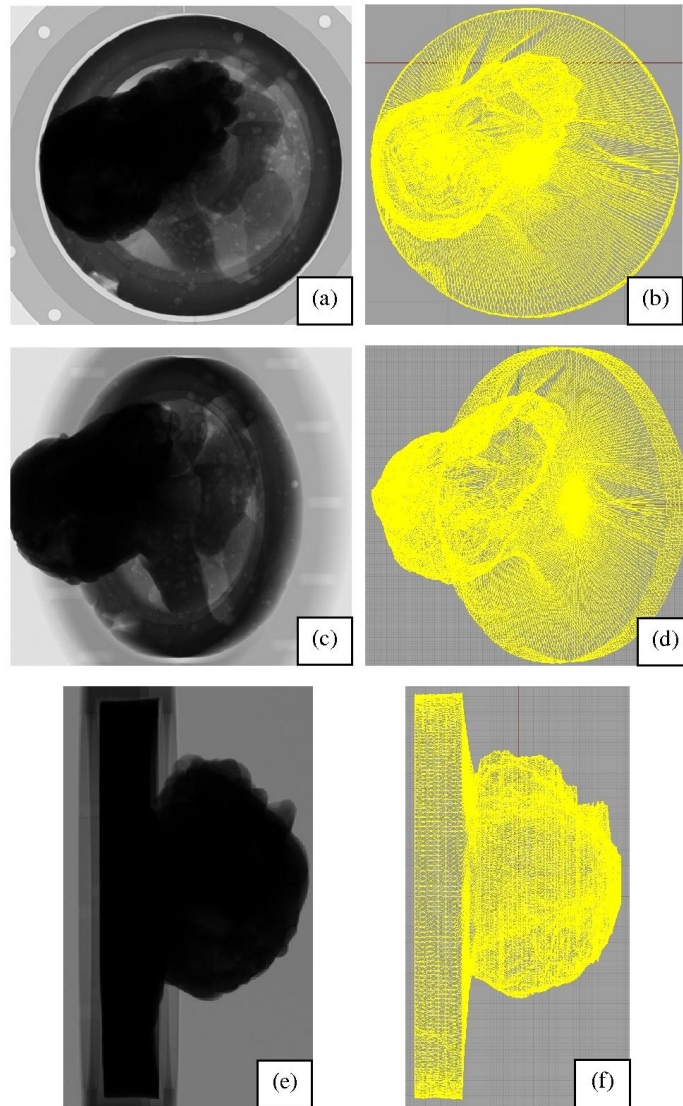
Figure 5.8: *Neutron Radiographies (a,c,e) and laser-scan surface reconstructions (b,d,f) of Head 1: (a-b) 90^0 compared to the neutron beam direction, (c-d) 45^0 compared to the neutron beam direction, (e-f) 0^0 compared to the neutron beam direction.*
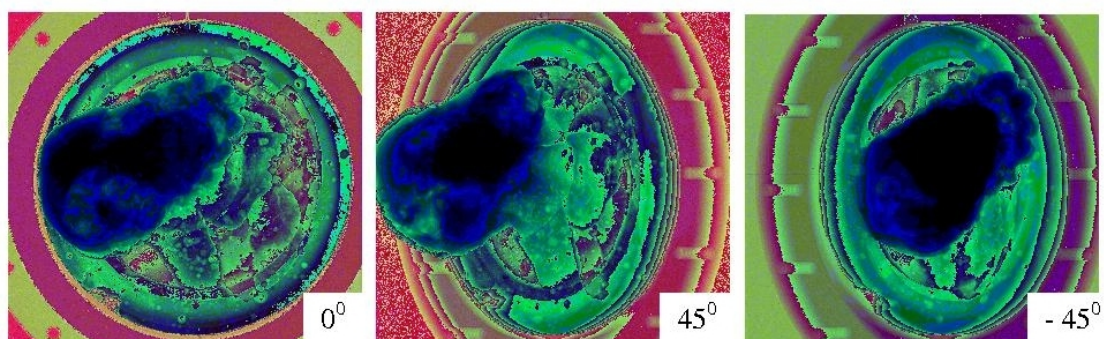
Figure 5.9: *Open beam false color neutron radiographies at 0^0, 45^0, -45^0 of rotation toward the incoming beam.*

Conclusions and future prospectives

Research results about the application of neutron technology in the field of cultural heritage discussed in this work show promising perspectives for the future of science and technology within cultural heritage studies.

It was presented assessment of neutron diffraction applications in the field of archaeological objects' study and the fruitful combination with other neutron analysis methods, the determination of conservation state, authentication and attribution of samples come from important archaeological sites and the fundamental role of the development activities on neutron instrumentation trough the application of new techniques to the precious *Ghiberti* heads, from the doors of the *Battistero di Firenze*.

Awareness of the potentials and limits is the first step towards a more extensive and aware application of these techniques. Like any physical application they are not a *panacea* but promising prospectives to improve the knowledge about our past and about methods of heritage preservation for the future generations.

The combination of Tomography, Prompt Gamma Activation Analysis and Neutron Diffraction results has provided useful information to reconstruct the spatial distribution and the nature of the interior parts of test samples.

The Prompt Gamma Activation Imaging/Neutron Tomography instruments were useful for studying two precious gilded bronze samples coming from the monumental doors of the *Battistero di Firenze* by *Lorenzo Ghiberti*. The study of silicon-photomultiplier (SiPM) as neutrons and gamma detector showed potential for applications in the field of neutron sources.

The study of bronze artifacts' composition and the presence of corrosion products provided essential information about the state of conservation and, indirectly, about the past environment and the physical and chemical events which transformed the objects into partially corroded matrices; such data is highly relevant for the work of archaeologists and conservators. The structural analysis of ancient silver coins have distinguished between 'authentic' and 'fake' ones, vital pieces of information when they are on display in a museum.

The further development of instrumentation and techniques will give us the opportunity to serve a growing multidisciplinary community. New imaging methods, in particular, will provide a novel, possibly comprehensive, neutron-based approach which will be applied for the 3D imaging of elemental and phase composition of archaeological objects as a result of a broad scope archaeological research.

List of publications related with PhD activities

International publications with referee

- G. Gorini and Ancient Charm collaboration (**Giulia Festa** et al.)
  Ancient Charm: a research project for neutron-based investigation of cultural heritage objects.
  Nuovo Cimento, **30**, N. 1, 47, DOI 10.1393/ncc/i2006-10035-9, (January-February 2007).

- **G. Festa**, C. Andreani, A. Filabozzi, D. Malfitana, J. Poblome
  Neutron techniques in cultural heritage.
  Acheometriai Muhely (Archaeometry workshop), III.2 $32 - 36$ (2006)

- **G. Festa**, P. A. Caroppi, A. Filabozzi, C. Andreani, M. L. Arancio, R. Triolo, F. Lo Celso, V. Benfante, S. Imberti
  Composition and corrosion phases of Etruscan Bronzes from Villanovan Age Measurements Science and Technology, **19**, 034004 (2008)

- **G. Festa** for the Ancient Charm Collaboration
  Study of archaeological samples via neutron techniques.
  Il Nuovo Cimento B, **122**, 06-07 (2008)

- **G. Festa**, W. Kockelmann, A. Kirfel and the Ancient Charm Collaboration
  Neutron Diffraction Analysis of Black Boxes.
  Archeometriai Muhely (Archaeometry workshop), Hungary, Nr. 2008/1

- Belgya, T., Z. Kis, L. Szentmiklsi, Z. Kasztovszky, **G. Festa**, L. Andreanelli, M.P. De Pascale, A. Pietropaolo, P. Kudejova, R. Schulze, and T. Materna
  A new PGAI-NT setup at the NIPS facility of the Budapest Research Reactor.
  Journal of Radioanalytical and Nuclear Chemistry, Vol. 278, No.3 (2008) 713718.

- S. Kasztovszky, Z. Kis, T. Belgya, W. Kockelmann, S. Imberti, **G. Festa**, A. Filabozzi, C. Andreani, A. Kirfel, K. T. Bir, K. Dzs, Zs. Hajnal, P. Kudejova, M. Tardocchi and the Ancient Charm Collaboration
  Prompt gamma activation analysis and time of flight neutron diffraction on 'black boxes' in the 'Ancient Charm' project.
  Journal of Radioanalytical and Nuclear Chemistry, Vol. 278, No.3 (2008) 661664.

- Belgya, T., Z. Kis, L. Szentmiklsi, Z. Kasztovszky, P. Kudejova, R. Schulze, T. Materna, **G. Festa**, and P.A. Caroppi
  First elemental imaging experiments on a combined PGAI and NT setup at the Budapest Research Reactor.
  Journal of Radioanalytical and Nuclear Chemistry, Vol. 278, No.3 (2008) 751754.

Communications at congresses

1. **G. Festa**
   Composition and corrosion phases of Etruscan Bronzes of Villanovan

Age.
4th European Conference on Neutron Scattering, $25 - 29$ June 2007, Lund (Sweden)

2. **G. Festa**

   Study of cultural-heritage artefacts by neutron techniques.
   Invited communication to XCIII Congresso Nazionale Societ Italiana di Fisica, Pisa (Italy), $24 - 29$ September 2007 (selected as **best comunication** - section Vb - Physics for cultural heritage).

3. **G. Festa**

   Investigation of Black-boxes by neutron techniques.
   Invited comunication to XCIII Congresso Nazionale Societ Italiana di Fisica, Pisa (Italy), $24 - 29$ September 2007 (selected as **best comunication** - section Vb - Physics for cultural heritage).

Conference proceedings

- Zsolt Kasztovszky and the Ancient Charm Collaboration (**Giulia Festa** et al.)
  ANCIENT CHARM: a new European project for neutron-based 3D imaging with applications to archaeological research.
  Symposium on archaeometry, Quebec City (Canada), 2/6 May 2006

- Pietropaolo and the Ancient Charm collaboration (**G. Festa** et al.)
  Ancient Charm: a project for the development of neutron-based elemental imaging.
  Congress proceedings (Siracusa, $26 - 29$ February 2008)

- Z. Kis, L. Szentmiklosi, T. Belgya, Zs. Kasztovszky, W. Kockelmann, **G. Festa**, A. Kirfel, P. Kudejova, R. Schulze, K. T. Bir, K. Duzs, Zs.

Hajnal, D. Visser and the Ancient Charm Collaboration
Radiography driven PGAA and neutron diffraction measurements on Black Boxes designed for the ANCIENT CHARM project.
37th International Symposium on Archaeometry, Siena, $12 - 16$ May 2008, published by Springer as an e-book

Posters

- Ancient Charm collaboration (**Giulia Festa** et al.)
  Imaging with Epithermal Neutrons for Cultural Heritage Research.
  IAN 2006 workshop, October $23 - 25/2006$ Oak Ridge National Laboratory, Oak Ridge (TN)

- **G. Festa** and the Ancient Charm Collaboration
  ANCIENT CHARM: a new project for neutron-based 3D imaging with applications to archaeological research.
  Looking Forward to the Past: Science and Heritage, Tate Modern, Bankside, London, 28 November 2006 (**first prize for best poster**)

- F. Lo Celso, V. Benfante, R. Triolo, N. Kardjilov, A. Hilger, **G. Festa**, A. Filabozzi, C. Andreani
  Application of Neutron Techniques on Marbles of Archeological Interest.
  4th European Conference on neutron scattering, $25 - 29$ June 2007, Lund, (Sweden)

- Z. Kasztovszky, T. Belgya, Z. Kis, W. Kockelmann, **G. Festa**, A. Kirfel, K. T. Bir, K. Ds, Z. Hajnal and the Ancient Charm Collaboration
  Promt Gamma Activation Analysis and time of flight neutron diffraction of Black Boxes in the Ancient Charm project.

12th International Conference on Modern Trends in Activation Analysis (Sep. $16 - 21$ 2007) Tokyo Metropolitan Univ., Hachioji-shi, Tokyo, JAPAN

- T. Belgya, Z. Kis, L. Szentmiklosi, Z. Kasztovszky, **G. Festa**, L. Andreanelli, M.P. De Pascale, A. Pietropaolo, P. Kudejov, R. Schulze, T. Materna, E.P. Cippo, and A.C. Collaboration
A new PGAI and NT setup at the NIPS facility of the Budapest research reactor.
12th International Conference on Modern Trends in Activation Analysis (Sep. $16 - 21$ 2007) Tokyo Metropolitan Univ., Hachioji-shi, Tokyo, JAPAN

- T. Belgya, Zs. Kasztovszky, Z. Kis, L. Szentmiklosi, W. Kockelmann, **G. Festa**, A. Kirfel, P. Kudejova, R. Schulze, K. T. Bir, K. Duzs, Zs. Hajnal, D. Visser
Radiography driven PGAA and neutron diffraction measurements on Black Boxes designed for the ANCIENT CHARM project.
37th International Symposium on Archaeometry, Siena, $12 - 16$ May 2008

Reports

- A. Pietropaolo, C. Andreani, M. P. De Pascale, **G. Festa** and L. Andreanelli, G. Mazzenga, E. Reali
Design and realization of a $xyz - \omega$ table for automated sample movements in PGAI/NT experiments
Internal Report- $ROM2F$/2006/19, Physics departement, $Università$ degli Studi di Roma Tor Vergata (2006).

- **G. Festa**, P. Caroppi, A. Filabozzi
Indagini di Fluorescenza X e micro-radiografia X su oggetti di interesse

archeologico
Tecnical report for Museo Nazionale Etrusco di Villa Giulia, Rome (2006).

- T. Belgya, Z. Kis, L. Szentmiklsi, Zs. Kasztovszky, **G. Festa**, L. Andreanelli, M.P. De Pascale, A. Pietropaolo, P. Kudejova, R. Schulze, T. Materna and the Ancient Charm Collaboration
  Working PGAI/NT system at the NIPS facility of the Budapest Research Reactor
  Internal report AC.

Bibliography

[1] Science and technology - ninth report. *House of Lords Publications*, http://www.publications.parliament.uk/pa/ld200506/ldselect/ldsctech/ 256/25602.htm, 2006.

[2] W. Kockelmann and A. Kirfel. Non-destructive phase analysis of *Archaeological Ceramics* using *TOF Neutron Diffraction*. *Journal of Archaeological Science*, 28:213–222, 2001.

[3] S. Siano, W. Kockelmann, U. Bafile, M. Celli, M. Iozzo, M. Miccio, O. Moze, R. Pini, R. Salimbeni, and M. Zoppi. Quantitative multiphase analysis of archaeological bronzes by neutron diffraction. *Applied Physics A*, 74:S1139–S1142, 2002.

[4] B. Dorner. Basic concepts. *Lecture Notes on Neutron Scattering. Introductory Course to ECNS'99*, KFKI-1999-04/E(REPORT), 1999.

[5] G.L. Squires. *Introduction to the theory of thermal neutron scattering.* Cambridge University Press, 1978.

[6] C. Ongaro and A. Zanini et al. *Analysis of photoneutron spectra produced in medical accelerators*, volume 45 of *L55-61*. Physics in Medicine and Biology, 2000.

[7] G.S. Bauer. Neutron sources. *Lecture Notes on Neutron Scattering. Introductory Course to ECNS'99*, KFKI-1999-04/E(REPORT), 1999.

[8] D. Chateigner. Combined analysis: structure-texture-microstructure-phase-stresses determination by X-ray and neutron diffraction. *http://www.ensicaen.ismra.fr/c̃hateign/texture/combined.pdf*.

[9] PDF. Power diffraction file, jcpds-icdd international centre for diffraction data.

[10] ICSD. *Inorganic Crystal Structure Database. Germany National Institute of Standard and Technology, USA*, 2004.

[11] CRYSTMET. Material toolkit 2.0.1. *Toth Information Systems Inc*, 2002.

[12] S.R. Hall, F.H. Allen, and I.D. Brown. The crystallographic information file (cif): a new standard archive file for crystallography. *Acta Crystallographica*, A47:655–685, 1991.

[13] A.C. Larson and R.B. Von Dreele. Gsas: Generalized structure and analysis software. *http://www.ccp14.ac.uk*.

[14] L. Lutterotti. Maud: Material analysis using diffraction. *http://www.ing.unitn.it/l̃uttero/maud/index.html*.

[15] J. Rodriguez-Carvajal. Fullprof: Refinement of powder diffraction data. *http://www-llb.cea.fr/fullweb*.

[16] H.R. Wenk and G. Molli. Texture and microstructure. *Journal of Structural Geology*, 25, 2003.

[17] H.R. Wenk and P. Van Houtte. Texture and anisotropy. *Reports on Progress in Physics*, 67:1367–1428, 2004.

[18] V. Randle and O. Engler. *Introduction to texture analysis.* CRC press, 2000.

[19] G.L. Molnar. *Handbook of Prompt Gamma Activation Analysis with Neutron Beams.* Kluwer Academic Publishers, 2004.

[20] N. Kardjilov. Overview of imaging with x-rays and neutrons. *Notiziario Neutroni e Luce di Sincrotrone*, 11(1):15–23, 2006.

[21] C.K. Avinash and M. Slaney. Principles of computerized tomographic imaging. *IEEE Press*, 1988.

[22] P. Buzhan, B. Dolgoshein, and A. Ilyin snd et al. An advanced study of silicon photomultiplier. *ICFA Instrumentation Bulletin*, www.slac.stanford.edu/pubs/icfa/fall01/paper3/paper3.pdf, 2001.

[23] D. Renker. New trends on photodetectors. *Nuclear Instruments and Methods in physics research A*, 571:1–6, 2007.

[24] P. Ciambrone for the KLOE collaboration. The *KLOE* calorimeter front end electronics. *Proceedings of IX International Conference on Calorimetry in High Energy Physics*, 2000.

[25] P. Buzhan, B. Dolgoshein, A. Ilyin, V. Kantserov, V. Kaplin, and et al. An advanced study of silicon photomultiplier. *Proceedings of the Seventh International Conference on Advance Technology and Particle Physics*, 23:717, 2001.

[26] D. Renker. New trends on photodetectors. *Nuclear Instruments and Methods in Physics Research*, 571:1–6, 2007.

[27] P. Buzhan, B. Dolgoshein, E. Garutti, M. Groll, A.Karakash, V. Kaplin, V. Kantserov, F. Kayumov, S. Klyomin, N. Kondratieva, A. Pleshko,

E. Popova, and F. Sefkow. Timing by silicon photomultiplier: A possible application for *TOF* measurements. *Nuclear Instruments and Methods in physics research A*, 567:353–355, 2006.

[28] A. Karar, Y. Musienko, and J. Ch. Vanel. Characterization of avalanche photodiodes for calorimetry applications. *Nuclear Instruments and Methods in physics research A*, 428:413–431, 1999.

[29] E. Aprile, P. Cushman, K. Ni, and P. Shagin. Detection of liquid xenon scintillation light with a silicon photomultiplier. *Nuclear Instruments and Methods in physics research A*, 556:215–218, 2006.

[30] S. Moehrs, D. J. Herbert A. Del Guerra, and M. A. Mandelkern. A detector head design for small-animal *PET* with silicon photomultipliers (*SiPM*). *Physics in medicine and biology*, 51:1113–1127, 2006.

[31] A. N. Otte, B. Dolgoshein, J. Hose, S. Klemin, E. Lorenz, R. Mirzoyan, E. Popova, and M. Teshima. The sipm - a new photon detection for *PET*. *Nuclear Physics B - Proceedings supplements*, 150:417–420, 2006.

[32] A. N. Otte, J. Barral, B. Dolgoshein, J. Hose, S. Klemin, E. Lorenz, R. Mirzoyan, E. Popova, and M. Teshima. A test of silicon photomultipliers as readout for *PET*. *Nuclear Instruments and Methods in physics research A*, 545:705–715, 2005.

[33] Z. Hajnal. Developing non-descructive *3D* material analysis of cultural heriatge objects: plans for 'black boxes' as test objects to be analysed in the *ANCIENT CHARM* project. *Archaeometry Workshop*, 1:3–6, 2008.

[34] K. Dzs. Realisation of the planned 'black boxes' in the *Hungarian National Museum*. *Archaeometry Workshop*, 1:7–20, 2008.

[35] A. Kirfel. Construction and description of the *UNIBONN* 'black boxes'. *Archaeometry Workshop*, 1:21–34, 2008.

[36] Z. Kis, T. Belgya, L. Szentmiklsi, Zs. Kasztovsky, P. Kudejova, and R. Schulze. *Prompt Gamma Activation Imaging* on 'black boxes' in the *ANCIENT CHARM* project. *Archaeometry Workshop*, 41-60, 2008.

[37] S. Siano, L. Bartoli, J. R. Santisteban, W. Kockelmann, M. R. Daymond, M. Miccio, and G. De Marinis. Non-destructive investigation of *Picenum* bronze artefacts using neutron diffration. *Archaeometry*, 48:77–96, 2006.

[38] D. A. Scott. *Copper and Bronze in Art. Corrosion, colorants, conservation.* The Getty Conservation Institute, Los Angeles, 2002.

[39] C.Y. Chen. *The Role of Particles on Initial Atmospheric Corrosion of Copper and Zinc*, volume ISBN 91-7178-155-2. Royal Institute of Technology, Stockholm, 2005.

[40] D. Barilaro, V. Crupi, D. Majolino, and V. Venuti. Characterization of pottery fragments by non-descructive neutron diffraction. *Journal of Applied Physics*, 98, 2005.

[41] A. Botti, M.A. Ricci, G. De Rossi, W. Kockelmann, and A. Sodo. Methodological aspects of *SANS* and *TOF* neutron diffraction measurements on pottery: the case of *Miseno* and *Cuma*. *Journal of Archaeological Science*, 33:307–319, 2006.

[42] L. Campanella et al. *Chimica per l'arte.* Zanichelli editore, 2007.

[43] M.J. Trindade, M.I. Dias, J. Coroado, and F. Rocha. Mineralogical transformations of calcareous rich clays with firing. *Applied Clay Science*, 2008.

[44] A. Filabozzi, A. Pietropaolo, C. Andreani, M.P. De Pascale, G. Gorini, W.Kockelmann, and L.C.Chapon. Non-invasive neutron diffraction analysis of marbles from the *Edificio con Tre Esedre* in *Villa Adriana*. *Nuovo Cimento C*, 29(02):237–252, 2006.

[45] A. Filabozzi, C. Andreani, M.P. De Pascale, G. Gorini, A. Pietropaolo, E. Perelli-Cippo, and R. Senesiand W. Kockelmann. Texture and structure studies on marbles from *Villa Adriana* via neutron diffraction technique. *Journal of Neutron Research*, 14(01):55–58, 2006.

[46] G.P. Bernardini, M.C. Squarcialupi, R. Trosti-Ferroni, M. Matteini, C.G. Lalli, G. Lanterna, M. Rizzi, and I. Tisini. The bronze doors of the baptistery in florence: a comparative study of the bronze alloys and alteration products. *Protection and Conservation of the Cultural Heritage of the Mediterranean Cities*, pages 43–47, 2002.

[47] E. Mello, P. Parrini, M. Matteini, A. Moles, G. Rocchi, A. Bartolozzi, L. Giorgi, and G. Giusgredi. *Lorenzo Ghiberti*: storie di *Giuseppe* e di *Beniamino*, storie di *Adamo* ed *Eva*. *Metodo e Scienza - operatività e ricerca nel restauro*, Sansoni Editore:168–202, 1982.

[48] P. Fiorentino, M. Marabelli, M. Matteini, and A. Moles. The condition of the 'Doors of Paradise' by *L. Ghiberti*. tests and proposal cleaning. *Studies in Conservation*, 27:145–153, 1982.

[49] E. Mello. The gilding of *Lorenzo Ghiberti*'s 'Doors of Paradise'. *Gold Bulletin*, 19 (4):123–126, 1986.

[50] S. Siano, M. Miccio, P. Bertelli, F. Marinelli, S. Mugnaini, and G. Garagnani. Studio sulla tecnica di fusione dei rilievi della *Porta del Paradiso*. *Schede di restauro*.

[51] S. Siano, R. Salimbeni, R. Pini, A. Giusti, and M Matteini. Laser cleaning methodology for the preservation of the *Porta del Paradiso* by *Lorenzo Ghiberti*. *Journal of Cultural Heritage*, 4:140s–146s, 2003.

[52] A. Giusti and M. Matteini. The *Gilded Bronze Paradise Doors* by *Ghiberti* in the *Florence Baptistery*. *ICOMOS*, 1997.

[53] M. Matteini, C. Lalli, I. Tosini, A. Giusti, and S. Siano. Laser and chemical cleaning tests for the conservation of the *Porta del Paradiso* by *Lorenzo Ghiberti*. *Journal of Cultural Heritage*, 4:147s–151s, 2003.